Contrôle et caractérisation d'un qubit singulet-triplet entraîné par l'interaction spin-orbite dans le silicium

Control and Characterization of a Spin-Orbit-Driven Singlet-Triplet Qubit in Silicon

par

Chloé Bureau-Oxton

Thèse présentée au département de physique

en vue de l'obtention du grade de docteur ès sciences (Ph.D.)

FACULTÉ des SCIENCES

UNIVERSITÉ de SHERBROOKE

Sherbrooke, Québec, Canada, 7 mai 2021

Le 7 mai 2021

le jury a accepté la thèse de Madame Chloé Bureau-Oxton dans sa version finale.

Membres du jury

Professeur Michel Pioro-Ladrière
Directeur de recherche
Département de physique

Docteur Dwight R. Luhman
Codirecteur de recherche
Sandia National Laboratories

Professeur Alexandre Blais
Évaluateur interne
Département de physique

Professeure Susan Coppersmith
Évaluatrice externe
Départements de matière condensée et de physique théorique
School of Physics, University of New South Wales

Professeur Bertrand Reulet
Président rapporteur
Département de physique

To my husband, Patrick

Sommaire

Les spins dans les semi-conducteurs sont d'excellents candidats pour l'implémentation d'un ordinateur quantique universel puisqu'ils sont compacts, peuvent être opérés à des températures relativement élevées, ont le potentiel d'atteindre des temps de cohérence très longs, et peuvent être combinés avec d'autres technologies quantiques pour former des systèmes hybrides. En particulier, les dispositifs fabriqués en silicium isotopiquement enrichi offrent des fidélités accrues et ont un processus de fabrication compatible avec les techniques utilisées dans les fonderies CMOS. Cette thèse étudie un qubit singulet-triplet confiné dans une boîte quantique double en silicium isotopiquement enrichi. Dans la première partie, cette thèse montre comment caractériser et ajuster la double boîte pour atteindre le régime de contrôle désiré. Une méthode numérique est développée pour trianguler la position des boîtes quantiques et des donneurs implantés dans le substrat. Un nouveau modèle permettant de prédire les taux tunnel en fonction des voltages de grille est également proposé, puis vérifié expérimentalement. Dans la deuxième partie, cette thèse montre comment implémenter le contrôle résolu en temps d'un qubit singulet-triplet entraîné par l'interaction spin-orbite. Deux méthodes différentes permettant d'implémenter des rotations arbitraire sur un qubit sont démontrées : la méthode pulsée (DC) et la méthode résonante (AC). Il est montré que le régime où le qubit est fortement entraîné peut être atteint à l'aide de ces portes résonantes. Finalement, la tomographie d'ensemble de portes (*gate set tomography*) est utilisée pour comparer ces deux types de portes logiques. Les résultats semblent indiquer que les portes résonantes sont de plus haute fidélité que les portes pulsées, et cela malgré le fait qu'elles soient plus lentes et qu'elles aient un facteur de qualité plus petit que ces dernières. Ces travaux sont les premiers à utiliser cette méthode tomographique pour caractériser des rotations autour de deux axes non-orthogonaux.

Mots-clés: Informatique quantique, Tomographie d'ensemble de portes, Donneurs, Boîtes quantiques, Silicium, Couplage spin-orbite, Qubits singulet-triplet

Abstract

Spins in semiconductors are attractive candidates for a universal quantum computer because they are compact, can be operated at relatively high temperature, have potentially long coherence times, and can be combined with other quantum technologies to form hybrid systems. Devices made using isotopically-enriched silicon offer the additional advantages of increased coherence time due to the relative absence of nuclear spins, and compatibility with existing CMOS foundry fabrication techniques. This work studies a singlet-triplet qubit formed in an enriched silicon metal-oxide-semiconductor double quantum dot device. The first part of this thesis presents techniques that are useful for characterizing the double-dot device and tuning it to the few electron regime. A capacitance-based numerical method is developed to triangulate the position of quantum dots and implanted donor atoms. Additionally, a new model that predicts dot-lead tunnel rates for varying gate voltages is proposed and its validity is demonstrated over a wide range of values. The second part of this thesis shows how to perform time domain control on a spin-orbit-driven singlet-triplet qubit. Two different methods for performing arbitrary single-qubit rotations are demonstrated: fast DC-controlled pulses, and slower resonantly-driven AC pulses. Evidence of the resonantly-driven pulses being pushed to the strongly-driven regime is shown. The final part of this thesis uses gate set tomography to compare the fidelity of these two types of single-qubit operations. Preliminary results seem to indicate that the resonantly-driven rotations have a higher fidelity than the DC-controlled operations despite the fact that the former are slower and have a smaller quality factor than the latter. This work constitutes the first time that gate set tomography is used to characterize a non-orthogonal set of gates.

Keywords: Quantum Computing, Gate Set Tomography, Donors, Quantum Dots, Silicon, Spin-Orbit Coupling, Singlet-Triplet Qubits

Acknowledgements

The research presented in this thesis is the product of many years of hard work and collaborations between the Université de Sherbrooke and Sandia National Labs. I would like to take the opportunity of thanking everyone who played a role in my academic accomplishments and made this thesis possible.

I would like to start by thanking my advisor, Michel Pioro-Ladrière, who has been overseeing my research since I first began my master's degree in 2011. His knowledge and insight regarding spin qubits was an asset throughout my PhD, while his constant encouragement and enthusiasm, particularly during the writing of my thesis, played a major role in bringing this work to fruition. I would also like to thank Dwight Luhman, my advisor at Sandia National Laboratories, for overseeing my research during the five years I spent in New Mexico. He was always available to lend a hand in the lab and his experimental know-how was invaluable in solving the many problems encountered with the dilution refrigerator, as well as in hunting down the source of electrical noise and ground loops in the experiment. Additional thanks to Malcolm Carroll and Michael Lilly for affording me the benefit of their guidance and expertise during my time at Sandia National Laboratories.

Among my colleagues at Sandia, I would especially like to thank my fellow experimentalists in the spin qubit group – Ryan Jock, Andrew Mounce, Patrick Harvey-Collard, Matthew Curry, and Martin Rudolph – for sharing their tips and tricks regarding the tuning and measurement of the devices as well as for exchanging good-humoured banter during the occasional CINT happy hour. I am very grateful to the superb team of theorists, including Toby Jacobson, Kenny Rudinger, Vanita Srinivasa, John Gamble, and Andrew Baczewski, for their help in answering the many technical questions encountered. Additional thanks to Meenakshi Singh for teaching me the ropes when I first arrived at the Labs, as well as to Victor Chavez

for his machining skills and for riveting discussions about the latest episode of *Game of Thrones*. I would also like to acknowledge Tzu-Ming Lu, Lisa Tracy, Amir Shirkhorshidian, Erik Nielsen, Steven Rinaldi, and numerous others that I had the privilege of meeting and working with during my PhD.

Thanks to all the friends I made upon moving to New Mexico: Yadeeh, Justin, Matt, Jaimie, Vanessa, Sarah, Joe, Crystal, Jay, Gio, Kendrick, and many others. The experiences I shared with these wonderful people (hiking, camping, rock climbing, skiing, paragliding, playing board games, etc.) showed me how fun, beautiful, and exciting the "Land of Enchantment" could truly be. Special thanks to Shelley, Maynard James, and Henry for inviting me into their home and their family during my last four months in NM. I am also grateful to all my Québécois friends and former colleagues at the Université de Sherbrooke for warmly welcoming me back into the fold every time I went home to Canada.

I would like to thank my parents, Josée Bureau and Richard Oxton, as well as my parents-in-law, Anne Harvey and André Collard, for their constant support and encouragement during the many years I have spent studying physics. They have always shown an interest in my research, despite not being physicists themselves, and will always be welcome to come visit with Patrick and me, wherever our careers may take us.

Last but not least, I am exceedingly grateful to my husband, Patrick Harvey-Collard, who has been a most significant person in my life ever since I started my Bachelor's degree in 2007. Over the years, he has played many different roles in my life: boyfriend, classmate, climbing partner, research colleague, ski instructor, husband, etc. He has been a constant source of support and encouragement, with regards to both my academic and recreational pursuits, and I am extremely lucky to get to share this important milestone with him.

Contents

List of Tables

List of Figures

Chapter 1

Introduction

1.1 Quantum computing

A quantum computer is a machine that makes use of the laws of quantum mechanics to solve computational problems. The idea of such a computer was first introduced in 1982 by Richard Feynman when he suggested that, in order to efficiently simulate quantum systems, one should use a machine that operates on quantum mechanical principles [1]. The fundamental component of a quantum computer is a two-level system referred to as a quantum bit, or qubit. Unlike classical bits that are either in the 0 or the 1 state at any given time, a quantum bit can be in a superposition of both states, i.e. in the 0 and the 1 state simultaneously. Additionally, two or more qubits can be entangled together to form correlated states in which the state of each qubit cannot be described without reference to the state of the others.

Although a large-scale universal quantum computer has not yet been developed, there exist quantum algorithms that would allow up to exponential speedup over the best known classical algorithms [2]. The most famous of these are perhaps Shor's algorithm [3, 4], which performs prime factorization of composite numbers, and Grover's algorithm [5, 6], which conducts searches through unstructured data bases. Thanks to algorithms such as these, quantum computation has potential applications in many fields, including cryptography [7], pharmaceuticals [8, 9], search and optimization, solving large systems of linear equations, and, of course, simulating quantum systems.

As stated above, a qubit is simply a quantum two-level system, such as the vertical and horizontal polarization of a single photon or the spin state of a spin-1/2

particle. There are, however, more requirements that must be met in order to properly implement a universal quantum computer [10]. First of all, the user must be able to initialize the system to a known state, often chosen to be the ground state of the system. The user must also have access to a universal set of quantum gates. In practice, this means achieving the minimum requirement of being able to perform arbitrary single-qubit rotations as wells as one entangling two-qubit gate between adjacent qubits [11, 12]. Another requirement is that the user must be able to read out the individual qubits of the system in order to extract the result of a computation. Because interactions between the qubits and the surrounding environment will cause the quantum state to decay, the system must be sufficiently isolated so that the coherence time (i.e. the time during which the quantum information is preserved) is long compared to the time required to execute an individual quantum gate. Finally, the chosen architecture must be scalable in order to eventually allow many qubits to be operated together and large quantum calculations to be performed. As no experimental implementation of a qubit will ever be perfect (i.e. have initialization, control and measurement fidelities of 100%), quantum error correcting codes have been developed in order to allow reliable computations to be performed on qubits with reasonably achievable control fidelities of $\gtrsim 99\%$ [13, 14]. However, the implementation of these error correcting codes requires a single logical qubit to be encoded in multiple physical qubits, placing an even greater importance on the scalability requirement imposed on the chosen system.

In an attempt to meet the requirements listed above, many different qubit architectures have been investigated over the past few decades: polarized photons [15], trapped ions [16], charge [17] and flux [18] in superconductors, charge [19] and spin [20] in semiconductor quantum dots, donor spins in semiconductors [21], nitrogen-vacancy centres in diamond [22], etc. Each of these architectures has its merits and challenges regarding various metrics such as scalability, qubit size, operating temperatures, coherence times, manipulation times, gate fidelity, readout fidelity, ease of fabrication, etc. For an overview of the advantages and challenges of these various architectures, the reader can refer to existing articles and reviews [23, 24, 25, 26, 27]. The work presented in the following thesis focuses on spin qubits in semiconductor quantum dots, though some of the techniques presented can be applied to a wide variety of systems.

1.2 Spin-1/2 qubits in semiconductors

Spin qubits, as the name implies, use the intrinsic angular momentums of particles, such as electrons or atomic nuclei, as qubits. In particular, spin-1/2 particles are attractive candidates for qubits because, when placed in a magnetic field, they form genuine two-level systems. Two distinct approaches have been proposed in order to implement spin qubits in semiconductors. In the first architecture, introduced by Bruce Kane, the nuclear spin of a donor atom such as phosphorus is used as a qubit, while the spin of the electron trapped in the donor atom's potential well is used to address the nuclear spin [28]. The second architecture, proposed by Daniel Loss and David DiVincenzo, uses nanoelectronic devices called quantum dots to trap single electrons and use their spin as a qubit [29]. In both architectures, electrostatic gates are used to control the electric environments of the qubits and perform quantum operations.

Spins in semiconductors offer many advantages that make them attractive candidates for a large-scale quantum computer. Because the devices used to trap the spins are generally small (atomic- and nano-scaled), they offer a high potential for scalability. They have long coherence times, ranging from several milliseconds for electron spins in quantum dots [30] to several seconds for donor spins [21, 31]. Furthermore, some architectures can be operated at relatively high temperatures [32], even up to room temperature [33]. Finally, because spins can be coupled to light, to magnetic fields, and (indirectly) to electric fields, spin qubits can be combined with other quantum technologies, such as photons or superconducting resonators, in order to create hybrid quantum systems [34, 35, 36].

Thanks to early work with epitaxially grown III-V materials, many of the milestones for spin qubits in semiconductors were first demonstrated using lithographically-defined quantum dots in GaAs/AlGaAs heterostructures [37]. These results include single-shot readout of an electron spin through spin-to-charge conversion [38], as well as coherent control of one- [39] and two-electron [20] spin states. However, both the gallium and the arsenic atoms in the host material have nuclear spins which result in a randomly oriented and fluctuating nuclear field of $\sim 1-3$ mT felt by the electron spin [40]. This fluctuating field leads to relatively short coherence times, which in turn makes it challenging to achieve high-fidelity qubit operations with these devices.

Silicon is an attractive material for the implementation of spin qubits because, unlike Ga and As, it has isotopes that have zero nuclear spin. Indeed, natural silicon is composed of 95% non-magnetic nuclei and can be isotopically enriched so that extremely few nuclear spins are present. Spin qubits fabricated using enriched silicon substrates have shown significantly longer coherence times, exceeding by more than two orders of magnitude the coherence times achieved in GaAs/AlGaAs and natural silicon devices, as well as higher gate fidelity [30, 41]. Interest in Si-based quantum devices is also driven by the fact that advanced techniques have already been developed for the fabrication of classical processors. Making use of these techniques could lead to higher uniformity in the devices – an important factor in scalability – and could allow the integration of classical and quantum processors [42]. Fabrication of Si-MOS qubits using these CMOS foundry-compatible techniques has already been demonstrated [43, 44].

Despite the many advantages of spin-1/2 particles in semiconductors, these qubits present their own unique challenges. Because single spins are magnetic moments, they can be manipulated using resonant oscillating magnetic fields. These oscillating fields can be produced using on-chip microwave waveguides [39]. However, oscillating fields produced in this manner do not offer high spacial selectivity and their strength – and therefore qubit operation time – is limited by photon assisted tunnelling and heating of the device. Another challenge arises from the fact that a common readout method for an electron spin is through energy-selective tunnelling of the electron to a nearby reservoir [38]. For this to be possible, strong external magnetic fields, on the order of 1 Tesla, must be applied in order to achieve a sufficiently large energy splitting between the spin-up and spin-down states. This large field results in an electron spin resonance frequency of several tens of gigahertz, leading to the need for high-speed electronics and extremely precise pulsing in order to achieve high-fidelity qubit operations. Finally, entangling gates between two spins often rely on controlling the strength of the exchange interaction between them, which arises when their wave functions overlap and decreases rapidly with distance. Because of the strong confinement potential of both donor atoms and quantum dots, it is challenging to create arrays where every qubit can be coupled to each of its nearest neighbours in order to perform entangling gates. Using multiple electron spins together – rather than a single spin – to encode a qubit allows all these challenges to be overcome, as will be discussed in the following section.

1.3 Single-triplet qubits

As stated previously, spin-1/2 particles such as electrons are convenient candidates for qubits because they are genuine quantum two-level systems. They are not, however, the only way to implement qubits using spins. In practice, systems with more than two levels can be used as qubits by limiting operations to two of the available levels. This means that the collective spin state of a group of electrons can be used as a qubit. Various types of spin qubits such as these have been proposed and demonstrated: the singlet-triplet qubit [20, 45], which is formed by two electrons in a double quantum dot [46]; the hybrid qubit [47, 48], composed of three electrons in a double quantum dot; the exchange-only qubit [49] and the resonant exchange qubit [50], both consisting of three electrons in a triple quantum dot [51]; and the quadrupolar exchange-only qubit [52], composed of four electrons in a triple quantum dot. Among these many schemes, the singlet-triplet qubit is the one most commonly encountered, and is the one that will be studied in this thesis.

Singlet-triplet (ST) qubits, as mentioned above, are usually composed of two electrons in a double quantum dot. They have also been demonstrated in other systems, such as four electrons in a single dot coupled to a phosphorus donor atom [53, 54]. They are normally encoded in the singlet (S) and non-polarized triplet (T_0) states while the polarized triplets (T_+ and T_-) are disregarded [45]. In some cases, the ST qubit is encoded using the singlet and a polarized triplet state [55], though this is less common. Regardless of the chosen encoding, care must be taken, when performing quantum operations and readout, to keep the qubit within the chosen energy level subspace in order to avoid leakage errors.

The ST qubit is driven using two distinct energies: the exchange energy, which arises when wave functions of the two electrons overlap; and the difference in Zeeman energy felt by the two electrons when they are confined to two separate dots [56]. These two distinct driving energies can be turned on and off by controlling the energy detuning between the two dots. This means that the ST qubit naturally lends itself to all-electrical control schemes. In other words, the oscillating magnetic fields used to manipulate single spins – and the microwave waveguides needed to produce these fields – are no longer necessary. The difference in Zeeman field between the two dots can be provided by different sources, including nuclear spins in the substrate [20, 57], a micro-magnet [58], a single donor spin [54], and spin-orbit

interaction [59, 60]. Though this latter effect is generally weak in bulk silicon [61], strong quantum confinement and interface effects can lead to a spin-orbit effect that is sufficiently large to serve as the second axis of control for the qubit. Therefore, spin-orbit-driven ST qubits in silicon are attractive candidates for a quantum computer because, in addition to all the advantages listed previously for silicon, universal single-qubit operations can be achieved without the need for any external components, such as microwave waveguides or micromagnets, which would inevitably complicate the fabrication and scalability of the devices [62].

The fact that ST qubits can be controlled entirely electrically allows for entangling gates between neighbouring qubits to be achieved through capacitive coupling [63]. Though exchange coupling is still necessary between the two electrons forming each ST qubit, the fact that entangling gates can be performed using capacitive coupling, which decreases less rapidly with distance than exchange coupling, greatly relaxes fabrication constraints.

Readout of ST qubits is typically performed using Pauli spin blockade [64]. This phenomenon doesn't depend on the strength of the applied magnetic field, as is the case with spin-1/2 particles, but rather on the size of the energy splitting between the S and T_0 states which is dictated by the orbital splitting of the quantum dot. In silicon, the presence of degenerate valley states can lift Pauli spin blockade and complicate the qubit readout process. However, it has been demonstrated that the valley splitting increases in the presence of large electric fields [65] and that this challenge can therefore be overcome by careful device tuning.

Despite it not being necessary to readout, a large magnetic field is nonetheless needed to generate the difference in Zeeman energy between the dots, which is used to drive qubit rotations. However, because it is the difference in the Zeeman field – rather than the total Zeeman energy – that is relevant, the resulting resonance frequency is several orders of magnitude smaller than it would be for a spin-1/2 particle in a similar field. This may be viewed by some as a drawback, since it will lead to longer operation times for resonantly driven gates. On the other hand, it means that many of the challenges associated with high resonance frequencies (such as the need for high-speed electronics and precise pulsing) can be avoided. Furthermore, resonantly driven gates are not the only way to perform operations on a ST qubit. Other, faster, qubit operations can be implemented with ST qubits due to the presence of two distinct driving energies.

1.4 Thesis outline

This thesis focuses on the control and characterization of spin-orbit-driven singlet-triplet qubits in isotopically-enriched Si-MOS double quantum dots. As discussed previously, these qubits are attractive candidates for implementing a quantum computer.

The first three chapters of this thesis are meant to serve as a guide to new users who may wish to take a many-electron quantum dot device and tune it to a regime where coherent ST qubit experiments can be achieved. Chapter 2 focuses on standard measurements that are routinely performed in order to characterize both the quantum dot device as well as the experimental setup. The experiments presented can also be used to confirm that the few-electron regime has been reached and that the electrons on the dot have been properly counted. Chapter 3 introduces devices implanted with phosphorus and antimony donor atoms. A new method for triangulating the position of the donor atoms with respect to the quantum dot is presented, and single-shot readout of the donor electron's spin using spin-to-charge conversion is demonstrated. Though these experiments are performed on a donor-dot system, they are just as relevant in the case of single- or multi-dot systems. Chapter 4 presents a tunnel rate model that was developed in order to facilitate tuning of the tunnel rate barriers to the appropriate values needed in order to couple the two electrons in the double quantum dot and to perform readout of the singlet-triplet qubit. This model can be integrated to existing computer-automated tuning methods [66] which are expected to play an essential role in the tuning of a quantum computer composed of a large number of qubits.

Once a device has been tuned to the few electron regime and the relevant parameters – such as tunnel rate and valley splitting – have been adjusted to reasonable values using the methods described in Chapters 2, 3, and 4, the system is ready for coherent qubit control to be attempted. Chapter 5 starts by presenting technical considerations regarding the experimental setup that must be addressed in order to achieve reliable qubit control and reasonable data acquisition times. Initialization of the qubit to the singlet ground state and readout of the qubit using a novel latching readout technique [67] is detailed in Sec. 5.4. Standard measurements used to characterize the qubit's inter-dot tunnel coupling and ramp rate regimes are also presented. Finally, two different methods for performing arbitrary single-qubit rota-

tions (a requirement for universal quantum computing) are demonstrated. The first of these methods, achieved by applying rapid "DC-controlled" pulses, is detailed in Sec. 5.7. The second method, performed by applying slower "AC-controlled" resonant pulses, is discussed in Sec. 5.8. Evidence of the qubit being pushed to the strongly-driven resonant regime, a feat difficult to achieve in qubits with transmission lines or micromagnets, is presented in Sec. 5.8.3.

After investigating, in Chapter 5, two different approches to controlling the qubit, the logical question to ask is: Which method should be used in order to achieve high-fidelity gates? In Chapter 6, gate set tomography is detailed and used to measure the fidelity of both the DC- and AC-controlled gates in order to compare their performances. To the best of the author's knowledge, the results presented in this chapter constitute the first time gate set tomography has been used to assess the performance of qubit rotations around non-orthogonal rotation axes.

Chapter 2

Quantum dot tuning and measurement methods

Spin qubits in semiconductors have garnered interest as potential candidates for a universal quantum computer because they are compact, can achieve long coherence times [21, 31], and in some cases can be operated at relatively high temperatures [32, 33]. Devices fabricated using isotopically enriched ^{28}Si are of particular interest because the absence of nuclear spins in the substrate leads to longer spin coherence times and, therefore, higher quantum gate fidelities [30, 41]. Silicon devices have the added advantage of profiting from existing techniques and infrastructures developed for the fabrication of classical processors [43, 44].

In recent years, important milestones towards building a quantum computer have been reached using quantum dots in silicon: Single-qubit gate fidelities exceeding 99.9% [68] and two-qubit gate fidelities up to 98% [69] have been achieved; Large linear arrays of individually-tuneable, series-coulpled quantum dots have been demonstrated [70]. Such impressive results may lead people unfamiliar with these devices to believe that they are generally easy to tune and to measure. The truth, however, is that a significant part of a graduate student's time measuring a device is dedicated not to performing novel research but rather to tuning the numerous device parameters in order to reach a regime where the experiments of interest have a chance of succeeding.

In this chapter, the two different geometries of silicon metal-oxide-semicontor (Si-MOS) quantum dot devices used throughout the thesis are presented. The experimental setup used to measure these devices is also described. The greater part of the

chapter, however, is dedicated to detailing standard measurements and techniques that are essential to characterizing such devices and tuning them into few-electron quantum dots. It is meant as a sort of guide that people new to the field can refer to when attempting to measure similar devices for the first time. The measurements presented range from room temperature characterization, which is performed before the device is even placed in a dilution refrigerator, all the way to pulsed-gate experiments, which provide information about the tunnel rates and excited states of the electrons on the dot. The measurements presented are not specific to the devices used in this theses and can be applied to a wide variety of quantum dot architectures and layouts.

Contributions: The devices were fabricated at Sandia National Laboratories by D.R. Ward, J.M. Anderson, R.P. Manginell, J.R. Wendt, and T. Pluym. Room temperature characterization was routinely performed by B. Silva, and occasionally by C.B.-O. The measurements and techniques presented are inspired by experiments described in the various references cited. All the device tuning, data acquisition, and analysis of results presented in this chapter was performed by C.B.-O.

2.1 Device layouts

The devices used in the experiments presented in this thesis are fabricated at Sandia National Laboratories using a fully foundry-compatible process. They are made using a single-gate-layer, MOS poly-silicon gate stack. This stack consists of a 1 μm thick epitaxially-grown layer of isotopically enriched ^{28}Si with 500 ppm residual ^{29}Si, followed by a 35 nm layer of silicon-oxide and, finally, 200 nm of highly doped n+ poly-silicon. The device gates are formed using electron-beam lithography and selective dry etching of the poly-silicon layer. Isotopically enriched ^{28}Si is used as the substrate because the absence of nuclear spins leads to longer coherence times both in quantum dots [30] and donor devices [71]. Additional details concerning device fabrication can be found in the supplementary material of Jock *et al.* [59] and Rochette *et al.* [72].

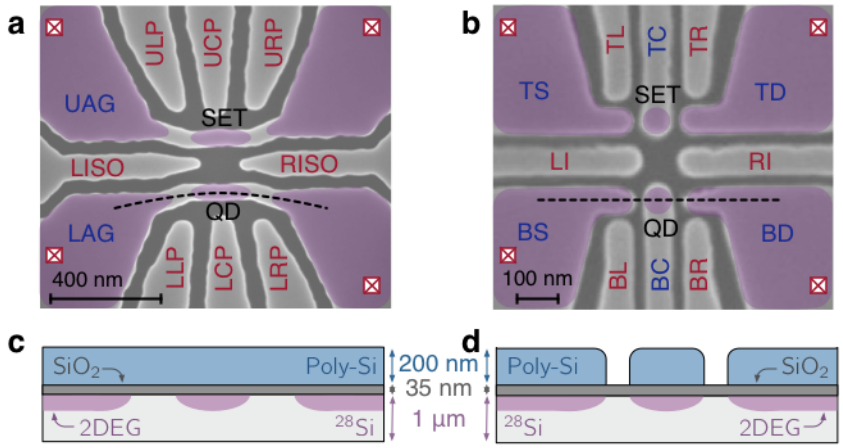

Figure 2.1: (a-b) SEM images of **(a)** a gated-wire device and **(b)** a SWAG device similar to the ones used in the experiments. Light grey areas are the poly-silicon gates, while dark grey areas are regions where the poly-silicon has been etched away to reveal the silicon oxide layer. Gates labelled in blue are positively-biassed accumulation gates, while gates labelled in red are negatively-biassed depletion gates. The red squares indicate the areas under which ohmic contacts are situated (outside of the imaged area). Purple shading indicates the approximate position of the 2DEG. **(c-d)** Schematic representations of the cross sections of **(c)** the gated-wire device and **(d)** the SWAG device along the dashed lines in **(a)** and **(b)**, respectively.

Two different types of devices with distinct gate layouts are used in this work. Scanning electron microscopy (SEM) images of the gated-wire device and the split-wire accumulation gate (SWAG) device are shown in Fig. 2.1(a) and Fig. 2.1(b), respectively. For both device geometries, a two-dimensional electron gas (2DEG) is formed at the interface between the ^{28}Si substrate and the silicon oxide layer by applying positive voltages to the poly-silicon accumulation gates (labelled in blue in Fig. 2.1). Negative voltages are then applied to the depletion gates (labelled in red) in order to shape the quantum dots (QDs), to tune the tunnel barriers between the dots and the surrounding 2DEG, and to control the number of electrons on the dots. Ohmic contacts (represented by red squares in Fig. 2.1) are used to control the electrochemical potentials of the 2DEGs, which are used as source and drain electron reservoirs for the QDs. Both device geometries are symmetrical and are designed for two QDs to be formed: one in the upper wire, and one in the lower wire. In the following work, the experiments are performed on the QD situated in the lower wire, while the dot in the upper wire is used as a single-electron transistor (SET) remote charge sensor (see Sec. 2.3.4).

As will be discussed later in this chapter, the large dimensions of the gated-wire device make it difficult to reach the few electron regime while maintaining reasonably large tunnel coupling between the QD and both leads. In order to reach the few electron regime, the device must be tuned asymmetrically in order to push the dot to one side and maintain coupling with a single electron reservoir (as in Harvey-Collard *et al.* [54]). The SWAG device was designed in order to avoid these tuning challenges. In this new device geometry, the tunnel barrier is naturally formed beneath the gap between the dot and reservoir accumulation gates. Because of this, the leads extend further out towards the dot and the few electron regime can be reached while maintaining coupling to both leads [53]. However, a consequence of the new design is that secondary dots tend to form beneath the tips of the reservoir gates that extend towards the QD. As these secondary dots can be formed and tuned in a reproducible manner, the SWAG device has successfully been used for double quantum dot (DQD) experiments [60, 62].

The experiments presented in the following chapter are routinely performed on both gated-wire and SWAG devices in order to characterize them and tune them to the desired regime. The donor-dot experiments presented in Chapter 3 are done on a gated-wire device. As for the tunnel rate, singlet-triplet, and gate set tomography experiments, presented in Chapters 4, 5, and 6 respectively, they are performed on SWAG devices.

2.2 Experimental setup

The measurements presented in this thesis are performed at the Center for Integrated Nanotechnologies (CINT). Initial vetting of the devices is performed at room temperature using a probing station (see Sec. 2.3.1), while all subsequent measurements are performed in ^{3}He/^{4}He dilution refrigerators. Either an Oxford Kelvinox MX400 or an Oxford Triton cryofree system is used. Both systems are similarly wired, have a base temperature of $\sim$ 35 mK and are equipped with superconducting magnets able to produce static magnetic fields larger than 8 T. They are equipped with both DC and RF lines used to connect the device, which is at base temperature, to the measurement instruments, which are at room temperature. All the DC lines are filtered using low-pass RC filters situated at the mixing chamber, while there is 20 dB attenuation on some, but not all, of the RF coax lines. The main differences

between the two systems are the electron temperature – which is 93 mK in the Kelvinox compared to $\sim$ 300 mK in the Triton – and the presence of 820 Hz noise in the Triton which is caused by the fridge's pulse tube.[1]

The samples are wire-bonded to a printed circuit board (PCB) which is placed in a copper enclosure and attached to the fridge's cold finger. Most of the device gates are connected directly to filtered DC fridge lines. The DC voltage to each of these gates is supplied either by a Stanford Research Systems SIM 928 Isolated Voltage Source, a Yokogawa GS200 DC voltage/current source, or a Keysight 33500B arbitrary waveform generator (AWG). Two of the device gates (usually LLP and LCP for gated-wire devices, or BL and BC for SWAG devices) are wired to RC bias tees located on the PCB. The DC paths of the bias tees are connected to DC fridge lines in the same manner as the other device gates. The RF paths, on the other hand, are connected to attenuated coax lines in order for high frequency pulses to be applied to these gates when needed. These pulses are supplied by Keysight 33500B AWGs. Finally, the ohmic contacts of both the QD and the SET are connected to unattenuated coax lines. An excitation signal of 50 μV rms is applied to the source ohmic using a Keysight 33500B AWG. The signal from the drain is amplified using a DL1211 current preamplifier and measured using an Stanford Research Systems SR830 lock-in amplifier.

The experimental setup used for the singlet-triplet qubit experiments presented in Chapters 5 and 6 differs slightly from the one presented here, and is discussed in Sec. 5.1.

2.3 Device tuning and standard measurements

2.3.1 Room temperature characterization

Because the process of cooling down a sample in a dilution refrigerator can be time-consuming and labour-intensive, it is best to have an idea of the quality of a device before undertaking this task. Therefore, when they are through with fabrication, all samples undergo room temperature characterization in order to cull the potentially good samples from those with obvious defects. This characterization process is performed at a probing station equipped with several Keithley 2400 source measure

[1] The Kelvinox is a "wet" dilution refrigerator and therefore does not have a pulse tube.

units (SMUs). Metallic probes that can be connected to these instruments are put into contact with the gold bonding pads of the device in order to test the integrity of the ohmic contacts and poly-silicon gates. The routine tests performed at room temperature are the following:

Ohmic contact tests: The resistance between a chosen reference ohmic contact and all other ohmic contacts is measured. The resistance between all the tested pairs should be a few tens of kiloohms when light is shone on the sample, and higher when the sample is in the dark.

Ohmic to poly leakage tests: The leakage current is measured between a working ohmic contact (identified during the ohmic contact test) and each of the poly-silicon gates of the device. The ohmic contact pad is grounded, while the voltage applied to the gate's contact pad is swept between +1 V and -1 V. The leakage current measured should always be less than 500 pA. Light is shone on the sample during this measurement.

Poly to poly leakage tests: The leakage current is measured between all neighbouring pairs of poly-silicon gates in order to check that the etching process was successful and that there are no accidental shorts. One of the gates in the pair is grounded, while the voltage to the other gate is swept between +1 V and -1 V. The leakage current should be too small to be detected by the SMU. Light is shone on the sample during this measurement.

Accumulation gate tests: The resistance between two ohmic contacts is measured while the voltage applied to the poly-silicon gate(s) above these contacts is swept from +2 V to -2 V. For the gated-wire device, the resistance between the ohmic contacts at the top (bottom) of the device is measured while the voltage on the UAG (LAG) poly-silicon gate is swept. For the SWAG device, the resistance is monitored between the ohmic contacts on the left (right) side of the device while the voltage applied to the TS and BS (TD and BD) gates is varied. The resistance should decrease as the voltage applied to the poly-silicon gate(s) is made less positive. This measurement is performed in the dark. For the device layouts and gate names, see Fig. 2.1.

After the room temperature tests have been performed and a sample has been chosen, it is wire-bonded to a printed circuit board and mounted into the dilution refrigerator. Before cooling the system, it is advisable to repeat some (or all) of these test in order to ensure that the sample has not been damaged by electrostatic

discharge during the bonding process. Repeating these measurements will also indicate if there are any shorts between the wire bonds, or if any of the bonds have been damaged or broken while the sample was being mounted into the fridge.

2.3.2 Stability diagrams

As discussed in Sec. 2.1, quantum dots can be formed in the devices used by applying positive voltage to the accumulation gates and negative voltages to the depletion gates. Because of its small size, the energy levels on the dot are quantized. The energy required to add an electron to the quantum dot is referred to as the addition energy. If both tunnel barriers are sufficiently transparent, electrons can tunnel from the source to the dot and from the dot to the drain when the thermal energy of the electrons[2] is larger than the addition energy. This leads to a measurable current between the source and the drain. However, at very cold temperatures, when the thermal energy is smaller than the addition energy, current through the QD can only be measured when the electrochemical potential level of an allowable QD transition is in the transport window (i.e. between the source and the drain energy levels). When there is no such electrochemical potential level in the transport window, electron tunnelling cannot occur and and no current can be measured. This phenomenon is known as Coulomb blockade.

Fig. 2.2(b) shows how the current through the QD varies as the voltage on one of the poly-silicon gates is swept. Sweeping the gate voltage causes the electrochemical potential ladder to shift up or down. This leads to periodic peaks in the current measured through the dot as different electrochemical potential levels move into and out of the transport window. These are often referred to as Coulomb peaks or Coulomb oscillations. Between the peaks, Coulomb blockade is observed and the number of electrons on the QD is constant. Crossing a peak indicates that an electron has been added or removed from the dot. Fig. 2.2(c) shows how the position of the Coulomb peaks changes when the voltage applied to two gates is swept. This type of plot is called a stability diagram. The Coulomb peaks have now become a series of parallel lines, the slope of which corresponds to the ratio between the energy lever arms of the two gates to the QD.

[2] The thermal energy of the electrons is given by $k_B T_e$, where k_B is the Boltzmann constant and T_e is the electron temperature (see Sec. 2.3.5).

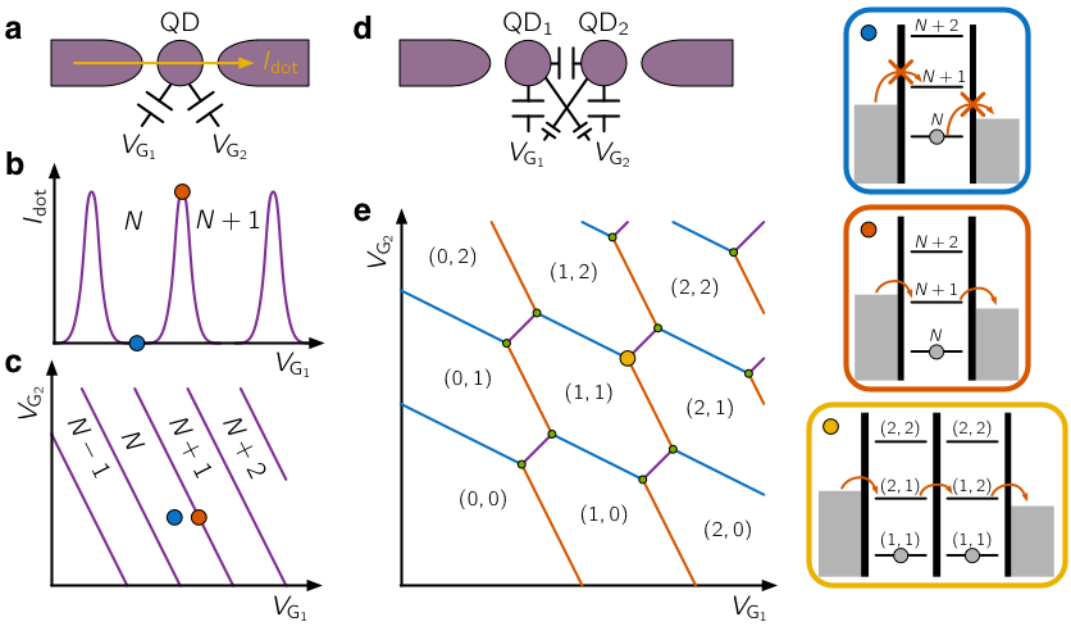

Figure 2.2: (a) Schematic of a single QD connected to source and drain reservoirs. Two gates, G_1 and G_2, are used to control the occupation of the dot. **(b)** Current through the QD as the voltage on one of the gates is varied. The red dot indicates a region where there is an electrochemical potential level of the dot in the transport window and current through the dot is observed. The blue dot indicates a region where there is Coulomb blockade and the number of electrons on the dot, N, is constant. **(c)** Stability diagram showing the position of the current peaks of the QD as the voltage on both gates is varied. **(d)** Schematic of a DQD. Each dot is capacitively coupled to both gates as well as to the other QD. **(e)** Stability diagram of the DQD. The red (blue) lines correspond to changes in the occupancy of the left (right) dot. The purple lines correspond to transitions where electrons are shuttled between the dots, but the total occupation of the DQD is conserved. The green dots indicate triple points where current through the DQD can be measured.

Fig. 2.2(e) shows a stability diagram of a DQD. In this scenario, both QDs are capacitively coupled to both gates, though not to the same degree. This leads to distinct slopes in the charge transition lines of the two dots. Because the two QDs are also capacitively coupled to each other, adding or removing an electron to one dot will cause a shift in the electrochemical potential ladder of the other. As a result of this, there is an offset to both transition lines at the points where the lines would normally have crossed, leading to two triple points (green dots in Fig. 2.2(e)) rather than a single intersection. These triple points get their name from the fact that they are situated at voltage points where three different charge states are degenerate.

Unlike in the single QD charge stability diagram, where current could be observed along the charge transition lines, in the case of the DQD, current between the source and drain can only be measured at the triple points. However, the charge transition lines can be observed using charge sensing (see Sec. 2.3.4).

2.3.3 Coulomb diamonds

The Coulomb diamond measurement is often performed in order to extract device parameters such as the lever arms of the device gates to the dot, the electron addition energy, and the energy splitting between the ground and excited states of the QD [73]. It consists in measuring the current through the QD as a function of the source-drain bias, V_{SD}, while the gate voltage is swept in order to empty the QD. Because the measurement relies on transport through the QD, it is most often performed on single dot devices, though it can be performed on double-dot devices if the gate voltage is swept in such a way as to pass through the triple points of the DQD [74, 75].

Fig. 2.3(a) shows a Coulomb diamond measurement performed on a gated-wire device tuned to form a single QD. Negative voltage is applied to gate LRP to empty the dot, and the source-drain bias is varied by changing the voltage on the source ohmic while keeping the drain ohmic at 0V. Current can only be observed if there is one or more electrochemical potential levels of the QD situated in the transport window. If the transport window is smaller than the energy level splitting of the dot, alternating regions of transport and Coulomb blockade will be observed as the gate voltage is swept and the QD is emptied. This is what can be seen in Fig. 2.3(a,b), near $V_{SD} = 0$ mV. As V_{SD} is increased, the Coulomb Blockade regions become narrower while the transport regions become wider. When the size of the transport window becomes larger than the energy level spacing of the QD, there is always at least one electrochemical potential level of the dot in the transport window and current is observed for all gate voltages.

The diamond shape of the Coulomb blockade region is where this measurement gets its name. Inside each diamond, the number of electrons on the QD, N, is constant and can be counted. The shape of the diamonds is skewed because V_{SD} is not changed symmetrically (i.e. the voltage of the source is swept, while the drain is kept at 0V). Furthermore, because of the capacitive coupling between the

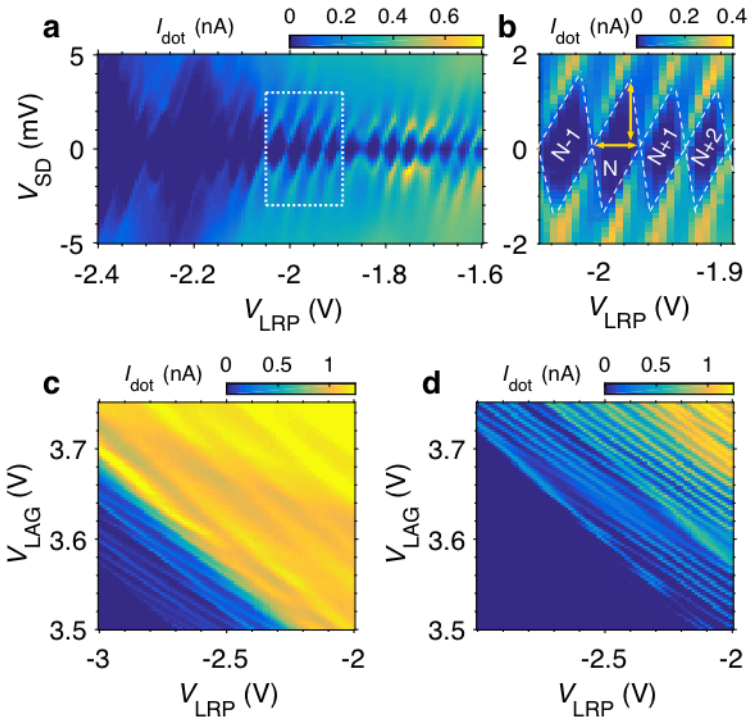

Figure 2.3: (a) Measured transport through a QD as a function of gate voltage and source-drain bias. **(b)** Zoom in the Coulomb diamond scan shown in **(a)**, in the region indicated by the white dotted lines. The blockaded regions where the number of electrons in the QD is constant are highlighted by white dashed lines. **(c,d)** Stability diagrams measured **(c)** before and **(d)** after compensating for the 6 mV offset introduced to the source-drain bias by the fridge lines.

source and the QD, the electrochemical potential of the dot will be affected by a change in V_{SD}, which will cause additional adjustments to the slopes of the diamonds [25]. The height of a diamond (vertical arrow in Fig. 2.3(b)) corresponds to the voltage at which the size of the transport window is equal to the addition energy ($E_{add}(N) = \mu(N+1) - \mu(N)$) of the QD. The width of the diamond (horizontal arrow in Fig. 2.3(b)), on the other hand, corresponds to the voltage change that must be applied to gate LRP in order to lower the electrochemical potential levels of the dot by this same addition energy. Since converting the vertical axis of the Coulomb diamond plots to units of energy is straightforward, the quotient between the height and width of a diamond yields the lever arm of the gate LRP to the QD.

A common use of the Coulomb diamond measurement is to confirm if the zero electron regime has been reached. If the dot is successfully emptied, the last visible

diamond doesn't close even when the gate voltage is made very negative [76]. This is not what is observed in Fig. 2.3(a), where making V_{LRP} more negative causes the diamonds to no longer extend to $V_{SD} = 0$, but where features are still visible for larger values of V_{SD}. This occurs because, as V_{LRP} is decreased and the dot is emptied, the tunnel coupling between the dot and the leads is decreased. This results in a reduction of the current flowing through the dot, to the point where it becomes difficult to measure. As V_{SD} is increased, QD transitions involving excited states enter the transport window, increasing the tunnel rate and therefore the measured current. This data indicates that, given the large dimensions of the gated-wire device, it is not possible to reach the few electron regime while simultaneously maintaining reasonable tunnel couplings with both leads. Further evidence of this can be obtained using charge sensing measurements, as discussed in Sec. 2.3.4.

For both device geometries presented in this thesis, it is not possible to reach the tuning regimes of interest for qubit experiments while maintaining transport through the QD.[3] In this work, the Coulomb diamond measurement was not used to determine the lever arm to the device gates because tuning from the transport regime to the regime of interest may cause significant changes in the confinement potential of the dot, and therefore to the lever arms. This type of measurement was still useful, however, for diagnostic purposes. Using a Coulomb diamond measurement, it was found that there was a 6 mV DC bias applied across the device when one ohmic was wired to a DC line and the other to a coax line. This was due to an element in the wiring of the wet dilution refrigerator acting as a thermocouple. Following this realization, a waveform generator was used as the input source for the QD in order to compensate for this DC bias. In the presence of the wiring-induced voltage bias, the Coulomb blockade lines of the device were washed together and indistinct, as shown in the upper right corner of the stability diagram plotted in Fig. 2.3(c). Correcting for this bias causes well defined Coulomb blockade lines to emerge in the corresponding area of the stability diagram shown in Fig. 2.3(d). These results highlight the importance of having a small source-drain bias when performing measurements on a QD.

[3] It is possible to tune the SWAG device to zero electrons while maintaining transport through the QD [53], but this tuning regime is very different from the one used during the singlet-triplet qubit experiments presented in Chapter 5.

2.3.4 Charge sensing

In some situations, measuring transport through a QD is not possible. For example, as a QD formed in a gated-wire device is emptied, the tunnel barriers become increasingly more opaque until the current through the dot becomes too small to be measured. Other examples include situations where one must measure QDs that are connected to a single reservoir (as in Fig. 4.2 and Fig. 5.1) or when single-electron tunnelling events must be measured. In these cases, charge sensing can be used to overcome the challenges and limitations of transport measurements.

In this work, a single electron transistor (SET) is used as a charge sensor. The SET is in essence a large QD connected to two leads and tuned to a regime where Coulomb blockade and transport through the SET can easily be measured [77]. As both the gated-wire and SWAG device geometries are designed to allow two QDs to be formed (one in the upper wire and one in the lower wire), one of these dots can be used as a charge sensor while the other is tuned to perform qubit experiments. As illustrated in Fig. 2.4(a), the SET is capacitively coupled to the QD as well as to the device gates. When the gate voltage is swept, smooth oscillations in current through the SET are observed. These oscillations are Coulomb blockade peaks. When an electron is added to the QD, the mutual capacitance between the QD and the SET causes the SET's Coulomb blockade peaks to shift to more positive gate voltages, resulting in an abrupt change in the current through the SET, as shown by the blue curve in Fig. 2.4(b). Plotting the derivative of the current through the charge sensor emphasizes these abrupt changes in current, as shown by the red curve in Fig. 2.4(b).

When tuning the SET, certain details must be taken into consideration. First, in order to avoid blind spots where changes in the dot occupation cannot be detected, it is preferable that the SET have wide Coulomb blockade peaks that do not drop to zero current. The peaks can be widened by increasing the tunnel coupling to the leads, by applying a larger source-drain bias to the SET, or by tuning the SET so that the energy spacing between its energy levels is on the order of the electron temperature. Next, because the shift in the charge sensor signal is proportional to the mutual capacitance between the SET and the QD, increasing this capacitance will result in a larger signal when the dot occupation in changed. This can be done when designing the device, by placing the SET and QD physically near each other and by avoiding putting gates between them that might screen electric fields. Finally, changes in

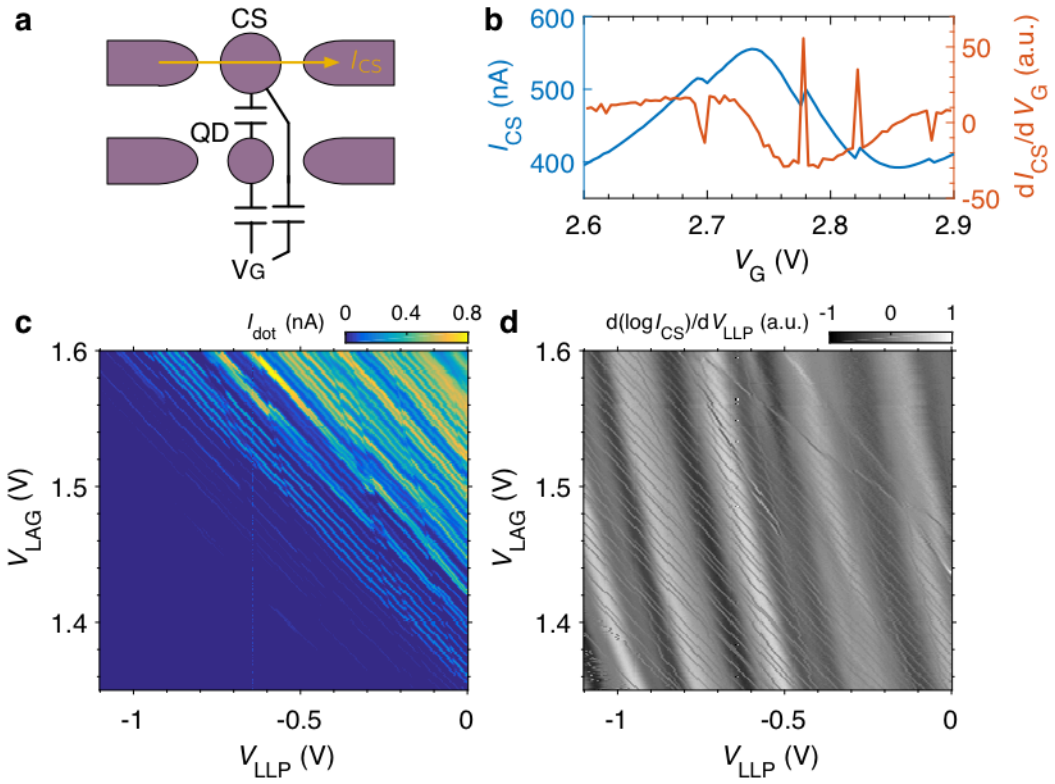

Figure 2.4: (a) Schematic representation of a single quantum dot device. The device gate, V_G, is capacitively coupled to both the QD and the charge sensor (CS). The CS is capacitively coupled to the QD. **(b)** Current through the charge sensor (blue) and its derivative (red) as a function of gate voltage. The slow varying background is due to the capacitive coupling between the device gate and the CS. The abrupt jumps in the CS signal indicate changes in the QD occupation. **(c-d)** Stability diagrams of an implanted gated-wire device acquired simultaneously by measuring **(c)** the current through the QD and **(d)** the current through the CS.

the QD occupation will result in the largest jumps in the SET current when the latter's derivative is maximized. Therefore, when performing measurements such as magnetospectroscopy (Sec. 2.3.6), pulsed gate spectroscopy (Sec. 2.3.7), or latched readout (Sec. 5.4), it is best to tune the SET to the edge of a Coulomb blockade peak in order to maximize the charge-sensed signal.

Fig. 2.4(c) and Fig. 2.4(d) compare stability diagrams acquired simultaneously on a gated-wire device through transport and charge sensing measurements, respectively. In the upper right corner of the charge-sensed measurement, the charge transition lines are not visible due to lifetime broadening; In this region, current always flows through the dot, even between the Coulomb peaks, and the number

of electrons on the dot is, therefore, never well defined. As the gate voltages are lowered and regions of Coulomb blockade begin to appear, so do the charge-sensed charge transition lines. In the lower left corner of the transport measurement, as the QD is emptied, the Coulomb blockade peaks become fainter until they disappear entirely. However, in the corresponding region of the charge-sensed measurement, features indicating the presence of QD charge transitions are still clearly visible. This is consistent with the results presented in Sec. 2.3.3 and indicates that the QD is not empty despite the fact that transport through the dot can no longer be detected. These measurements highlight the important role that charge sensing plays in confirming that the few electron regime has been reached.

2.3.5 Electron temperature

While performing measurements on QDs, low temperatures are necessary not only to ensure that the electrons remain well confined, but also to prevent thermal excitation of their spin state which will be used as a qubit (see Chapter 5). Though dilution refrigerators can easily reach sufficiently low temperatures for these experiments, there is no guarantee that the electrons in the QD are thermalized at the same temperature as the mixing chamber. Thermal contact between the sample and the cold finger might be poor, and high frequency electrical noise may be making its way from the control and measurement instruments down to the sample through the fridge's wiring. Being able to measure the temperature of the electrons is necessary in order to determine how large the other energies in the system (e.g. Zeeman splitting, valley splitting, etc.) must be in order for the experiments to be successful.

As the wet dilution refrigerator used in these experiments is equipped with a well-calibrated thermometer as well as a heater on the mixing chamber, the electron temperature is extracted by measuring the width, w, of an electron transition line of the QD as a function of the mixing chamber's temperature, T_{MC}, in a manner similar to the one described in Bradley *et al.* [78]. If charge sensing measurements are performed, the width of the transition is extracted by fitting a Fermi-Dirac step function to the signal of the charge sensor as the QD is swept across a charge transition line [79]:

$$I_{\mathrm{CS}}(V_{\mathrm{G}}) = m \cdot V_{\mathrm{G}} + b + \frac{a}{\exp((V_{\mathrm{G}} - V_0)/w) + 1} \quad , \tag{2.1}$$

where V_0 is the position of the charge transition, a, is the amplitude of the step function, and m and b describe the slope and offset of the background CS signal. If transport measurements are performed, the width of the transition is extracted by fitting the derivative of the Fermi-Dirac step function to the transport current through the QD:

$$I_{\mathrm{QD}}(V_{\mathrm{G}}) = c - \frac{a}{4w}\cosh^{-2}\left((V_{\mathrm{G}} - V_0)/w\right), \tag{2.2}$$

where a, w, and V_0 are defined as in Eq. (2.1), and c is an offset that may be present in the current through the QD. When measuring the width of the electron transition in transport, it is important to tune the tunnel barriers so that they are symmetrical and very opaque to avoid broadening of the transition due to a large tunnel coupling with the leads. The source-drain bias used must also be as small as possible. Increasing the temperature of the mixing chamber will provoke an increase in the width of the charge transition in the following manner:

$$w(T_{\mathrm{MC}}) = \frac{k_{\mathrm{B}}}{\alpha}\left(T_{\mathrm{MC}}^n + T_{\mathrm{e},0}^n\right)^{1/n}, \tag{2.3}$$

where k_{B} is Boltzmann's constant, α is the lever arm to the gate V_{G} used to sweep across the charge transition, and $T_{e,0}$ is the saturated electron temperature. The exponent, n, depends on the electron thermalization mechanisms involved [80].

The measurements performed in order to extract the electron temperature of the MX400 wet dilution refrigerator are presented in Fig. 2.5. Fig. 2.5(a) shows the current through a QD formed in a gated-wire device as the gate voltage is swept across an electron charge transition. Repeating this measurement at varying mixing chamber temperatures and using Eq. (2.2) to extract the width of the transition yields the temperature dependence shown in the blue curve of Fig. 2.5(c). By performing a fit to this data using Eq. (2.3), a saturation temperature of $T_{\mathrm{e},0} = 379 \pm 40$ mK is extracted. When this measurement was performed, there was 20 dB attenuation on the two coax lines that were connected to the bias tees on the pulsing gates, and 80 MHz low-pass filters on all the DC lines. In an attempt to improve the electron temperature, 3.55 kHz RC filters were added to all the DC lines of the fridge. The electron temperature measurement was then repeated by performing a charge-sensed measurement on a SWAG device, as shown in Fig. 2.5(b). Using Eq. (2.1) to

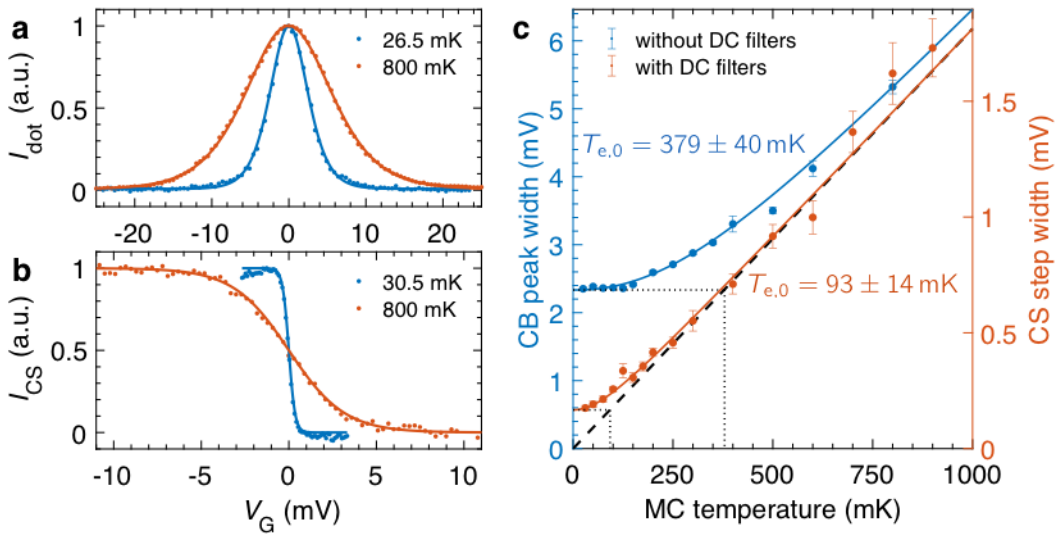

Figure 2.5: Measuring the electron temperature. **(a)** Width of a QD charge transition measured in the transport regime at fridge temperatures of 26.5 mK (blue) and 800 mK (red). **(b)** Width of a QD charge transition measured through charge sensing at fridge temperature of 30.5 mK (blue) and 800 mK (red). The amplitude of the data in **(a-b)** has been normalized for clarity. The solid lines are fits to the data. **(c)** Width of an electron charge transition measured through transport in a gated-wire device (blue) and through charge sensing in a SWAG device (red) as a function of the mixing chamber (MC) temperature. The blue (red) data was taken before (after) RC filters were added to the DC lines of the dilution refrigerator. The solid lines are fits to the data used to extract the electron saturation temperature. The black dashed line indicates the transition width if the electrons were thermalized with the mixing chamber.

extract the width of the transition at various mixing chamber temperatures results in the red curve shown in Fig. 2.5(c). This time, fitting Eq. (2.3) to the data yields a saturation temperature of $T_{e,0} = 93 \pm 14$ mK. This significant improvement in the electron temperature highlights the effect of high frequency electrical noise on the QD and emphasizes the importance of electrical filtering when high temperatures can hinder the experiments being performed.

The experiments presented in Chapter 5 and Chapter 6 are performed in an Oxford Triton cryofree refrigerator. In this system, the electron temperature is measured to be approximately 300 mK. This value is obtained by extracting a gate lever arm from a magnetospectroscopy measurement (see Sec. 2.3.6) and measuring the width of an electron transition line. The electron temperature is then calculated using Eq. (2.3).

The measurements presented in this section can serve not only to extract the electron temperature, but to get a precise measurement of the lever arm to the gate used to sweep across the charge transition. Indeed, from Eq. (2.3) we see that at high mixing chamber temperature ($T_{MC} \gg T_{e,0}$), when the electrons of the quantum dot are well thermalized with the fridge, the width of the electron transition varies linearly with T_{MC} and the slope is given by k_B/α. Extracting the lever arm from the fit to Fig. 2.5(c) is therefore straightforward. Though the lever arm can also be extracted from Coulomb diamond (Sec. 2.3.3) or magnetospectroscopy (Sec. 2.3.6) measurements, this method involving the temperature dependence of charge transition widths is found to be the most reliable.

2.3.6 Magnetospectroscopy

Magnetospectroscopy is a measurement technique that can be very useful when characterizing a QD. It can be used to extract various parameters such as spin filling, valley splitting, and gate lever arms, to name a few. The measurement consists in measuring how the strength of the external magnetic field affects the electrochemical potential levels of the QD [81, 82]. As the external magnetic field is increased, the electrochemical potential of the dot is expected to change in the following manner [83]:

$$\Delta\mu_N = g\mu_B B_{ext} \Delta S_{z,N} \ , \tag{2.4}$$

where $g = 2$ is the electron g-factor in silicon, μ_B is the Bohr magneton, B_{ext} is the strength of the external magnetic field, and $\Delta S_{z,N} = S_z(N) - S_z(N-1)$ is the change in the projection of the spin of the system along the quantization axis when the N^{th} electron is added. Generally, adding an electron to the dot results in $\Delta S_{z,N} = \pm 1/2$, though other values have been observed [81, 84].

Fig. 2.6(d) shows a magnetospectroscopy measurement performed on a SWAG device tuned to the few electron regime. The position of the $N = 1$ to $N = 2$ transition line is measured through charge sensing while the strength of the external in-plane magnetic field is varied. Between $B_{ext} = 0$ T and $B_{ext} = 2.85$ T, the slope of the charge transition is positive, indicating that a spin up electron is added to the dot. For $B_{ext} > 2.85$ T, the slope is negative, indicating that a spin down electron is added. In order to understand this behaviour, the electrochemical potential

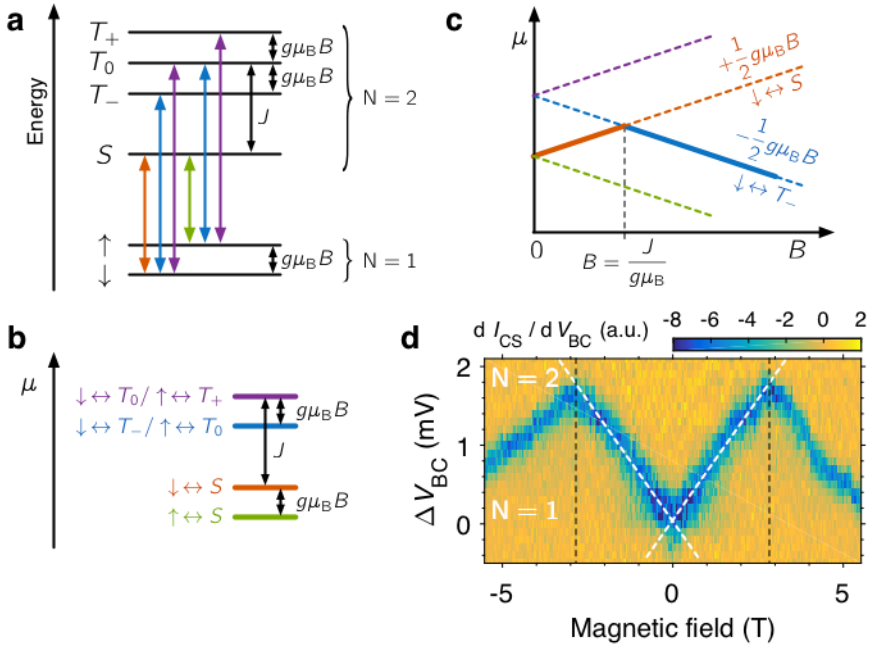

Figure 2.6: (a) Energy level diagram of the $N = 1$ and $N = 2$ electron states of a single QD in the presence of a magnetic field B. The transitions allowed while adding or removing an electron are indicated by coloured arrows. **(b)** Electrochemical potential of the electron transitions shown in **(a)**. **(c)** Electrochemical potential of the allowable transitions of the dot as a function of magnetic field. The solid line indicates the transitions observed if the QD is in its ground state. **(d)** Magnetospectroscopy scan showing the position of the $N = 1$ to $N = 2$ transition line of a gated-wire device as a function of magnetic field.

ladder of the system must be studied. Fig. 2.6(a) shows an energy level diagram for the $N = 1$ and $N = 2$ electron states in the QD. The transitions allowed when adding or removing an electron from the QD are indicated by coloured arrows. The electrochemical potential ladder resulting from these transitions is shown in Fig. 2.6(b), where the colours relate the levels to their corresponding transitions drawn in Fig. 2.6(a). Because the magnetic field affects the energy levels of the dot, it will also affect this electrochemical potential ladder, as shown in Fig. 2.6(c). During the magnetospectroscopy measurement, the gate voltage is swept slowly with respect to tunnelling and relaxation times. As a result of this, only the transitions involving the ground states of the QD can be observed. These transitions are drawn as bold lines in Fig. 2.6(c). At low magnetic field, the ground state of the $N = 2$ charge region is the singlet and the energy required for the $\downarrow\leftrightarrow S$ transition increases with magnetic field. If the magnetic field is increased beyond $B = J/g\mu_B$, the T_- triplet

becomes the ground state of the $N = 2$ charge region and the energy required for the $\downarrow \leftrightarrow T_-$ transition decreases with magnetic field. This is what is observed in the experimental results shown in Fig. 2.6(d). The fact that the electrochemical potential shifts as expected lends further support to the claim that the few electron regime has been reached and that the electrons have been properly counted.

As mentioned above, the valley splitting can be extracted from the magnetospectroscopy measurement. Indeed, the change in the slope of $\Delta\mu_N$ occurs when the Zeeman splitting ($g\mu_B B$) is equal to the valley splitting (J). The fact that this change in slope occurs at $B = 2.85$ T indicates that the valley splitting is $J = 330$ μeV in this device. From Eq. (2.4), the slope is expected to be $m = g\mu_B \Delta S_{z,N}$. By performing a fit to the slope at low magnetic field (and using $g = 2$ and $\Delta S_{z,N} = \frac{1}{2}$), a lever arm of $\alpha = 95.8 \pm 2.3$ μeV/mV is extracted for the BC gate to this dot. However, it is worth noting that the slope can be affected by impurities near the dot [85] and can change as a function of magnetic field due to contraction of the orbitals [86, 87, 88]. For this reason, the electron temperature measurement is the preferred method for extracting the gate lever arms.

2.3.7 Pulsed gate spectroscopy

Pulsed gate spectroscopy is a measurement that consists in applying a square pulse to one or more gates of the device while measuring the average occupation of the dot through charge sensing [89].[4] If the voltage pulse is across a charge transition line, the QD system is brought out of equilibrium and an electron will be loaded and unloaded from the dot at the frequency of the pulse that is being applied. Either the frequency or the amplitude of the square pulse are varied as the centre of the pulse is swept across a charge transition line, allowing information about the excited states and tunnel rates to be extracted.

Fig. 2.7 shows a pulsed gate spectroscopy measurement performed on a SWAG device tuned to the few electron regime and subjected to a 1.2 T in-plane magnetic field. The device is tuned in such a way that there is only one reservoir coupled to the dot (see Fig. 4.2). In Fig. 2.7(a), a square pulse with a fixed peak-to-peak amplitude of 10 mV is applied to the bottom centre (BC) plunger gate while the average voltage on the gate, V_{BC} is swept across the $N = 1$ to $N = 2$ charge transition

[4] Transport measurements can also be performed, as described in Fujisawa *et al.* [90].

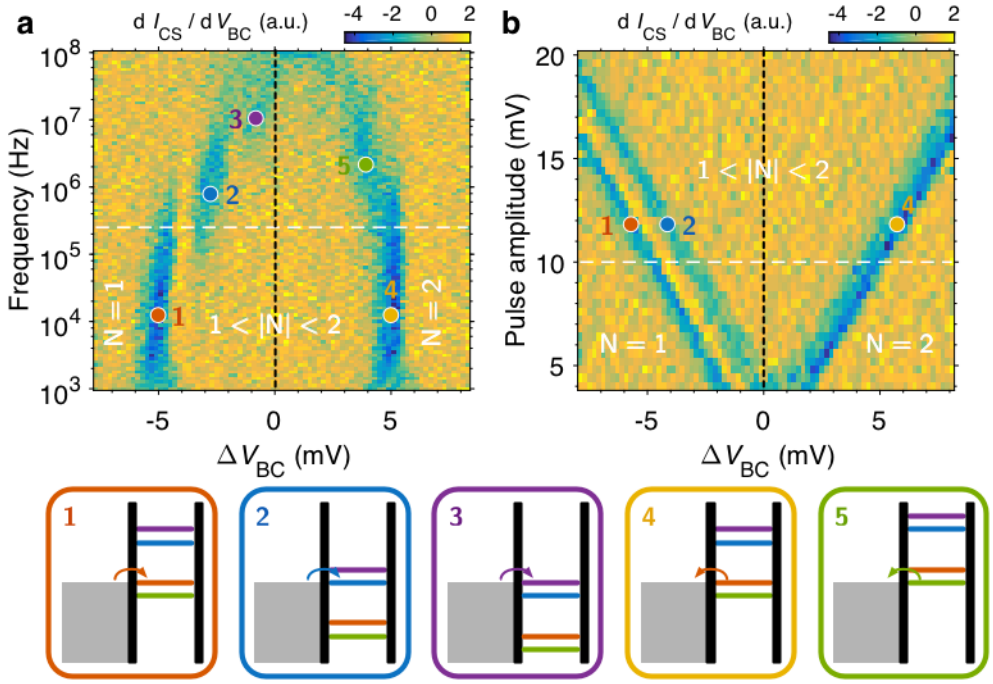

Figure 2.7: Pulsed-gate spectroscopy on the $N = 1$ to $N = 2$ charge transition line of a single QD. **(a)** Data acquired by applying a 10 mV square pulse on the BC gate (dashed white line in **(b)**) and varying its frequency. **(b)** Data acquired by applying a 251 kHz square pulse on the BC gate (dashed white line in **(a)**) and varying its amplitude. The black dotted lines indicate the position where the centre of the square pulse coincides with the charge transition line. The applied external magnetic field is 1.2 T. The colours of the electrochemical potential levels in the ladder relate to their corresponding transitions illustrated in Fig. 2.6(a).

line. At low frequency ($<$ 40 kHz), the half-period of the pulse is much longer than the tunnelling time to and from the dot. Therefore, when the pulse is applied across the transition line, the average dot occupation is $|N| = 1.5$ regardless of the number of electrochemical potential levels that are energetically available for the loading and unloading processes. As the frequency is increased and the period of the pulse becomes comparable to the tunnelling times, electrons are no longer shuttled to/from the dot during every iteration of the pulse and the average occupation of the dot becomes highly dependent on the tunnel rates to the lead. In this regime, increasing V_{BC} so that $N = 2$ excited states can be loaded results in an increase in the loading rate, and therefore an increase in the average occupation of the QD. This produces the feature indicated by the blue dot in Fig. 2.7(a). A similar argument can

be made to explain the feature arising from an $N = 1$ excited state contributing to an increase in the unloading rate (green dot in Fig. 2.7(a)).

Fig. 2.7(b) shows the result of a pulsed gate measurement where the amplitude of the pulse is varied while its frequency is kept constant. The features that are visible in this scan are highly dependent on the chosen frequency. This scan is used to determine whether the features in Fig. 2.7(a) relate to transitions that increase the loading or the unloading rates. In other words, it is used to determine if the electrochemical potential of each transition is situated higher or lower in the ladder relative to the transition involving both ground states (red transition in Fig. 2.6 and Fig. 2.7). In Fig. 2.7(b), the feature indicated by the blue dot moves left as the amplitude of the pulse is increased, keeping a constant spacing with the feature marked by the red dot. This means that the corresponding level in the electrochemical potential ladder is situated above the transition involving both ground states. Had it been below this transition, it would have been parallel to the feature indicated by the yellow dot.

If the lever arm to the BC plunger gate is know, the pulsed gate measurements presented in this section can be used to map the electrochemical potential ladder and extract the relevant energy spacings of the system. In addition to this, the frequency scan can be used to estimate the tunnel rate between the dot and the lead. Indeed, additional features start appearing in this scan when the tunnel rates are on the order of the pulse frequency. From Fig. 2.7(a), the loading rate between the ground states is estimated to be on the order of 40 kHz. For the pulsing experiments presented in this thesis, the tunnel rates should ideally be between a few tens of kHz to 1 GHz in order to achieve reasonable initialization times while maintaining good readout fidelities. The pulsed gate experiments constitute a fast and easy way to get an estimate of these rates. For a more precise value of the tunnel rates, the frequency scan can be fit using a model described in Harvey-Collard [91] (Sec. 2.9.1) or they can be measured directly using the method presented in Sec. 4.2.

Chapter 3

Investigating and measuring donor-dot systems

The spin of an electron bound to a dopant atom in silicon is an interesting candidate for a quantum bit because of its potentially long coherence time [27, 41, 71]. In recent years, donor electrons have successfully been used as spin-1/2 qubits [92] and coherent coupling between a donor electron and a QD in silicon has been demonstrated [53, 54]. Direct coupling between two donor electrons has also been achieved [93], but remains extremely difficult because it requires near-atomic precision on the position of both donors [94, 95].

There are two techniques commonly used for fabricating silicon devices with donors. The first, which is the one used in this work, is ion beam implantation (see Sec. 3.1) and consists in accelerating a beam of ions and directing it towards the surface of the substrate. This technique has the advantage of being compatible with most device fabrication processes, but offers less control on the number and position of the ions implanted. Use of a focussed ion beam in conjunction with diode detectors [96] can reduce the uncertainty on these parameters, but not sufficiently to attain reasonable yield for double-donor experiments. The second technique used to fabricate devices with donors is hydrogen lithography using scanning tunnelling microscopy (STM) [97]. Though this technique offers far better control on donor placement, it is not compatible with commonly used fabrication techniques and significantly increases the complexity and duration of the fabrication process.

Originally, this thesis work was supposed to focus on coupling two donor electrons via a nearby quantum dot. As is often the case, this goal was found to be

rather more ambitious than realistic. Numerous devices were measured, but none was found to simultaneously have all characteristics needed to perform donor-dot experiments (dot tunability, charge sensing capability, reasonable donor-dot tunnel coupling, etc.). Consequently, the focus of the work was redirected from donor-dot to double-dot experiments. The results pertaining to donor-dot devices that were obtained before this shift in goals are presented in this chapter. In Sec. 3.1, the different device geometries and donor implant parameters are discussed. Sec. 3.2 presents an intuitive as well as a numerical method for determining the position of an implanted donor. Finally, Sec. 3.3 presents results regarding single-shot readout of a donor electron.

Though the experiments presented in this chapter are performed on electrons bound to donor atoms, the triangulation and readout techniques used can be easily transferred to single- or multi-dot devices. This is because the donor potential well used to confine the electron is not dissimilar to the confinement potential created by the electrostatic gates of a small quantum dot device. In the discussions that follow, the donor-dot system is likened to a double quantum dot, and the two terms are used somewhat interchangeably.

Contributions: Simulations regarding the expected number, depth, and straggle of the donors implanted into the devices was performed by M. Singh. The numerical method used in Sec. 3.2.2 to calculate the position of a donor, as well as the accompanying results presented in Fig. 3.3 were produced by E. Nielsen with input from C.B.-O. Device tuning and triangulation measurements were performed by C.B.-O. Pulsed spin readout experiments were also performed by C.B.-O. using pulsing code provided by D. Luhman.

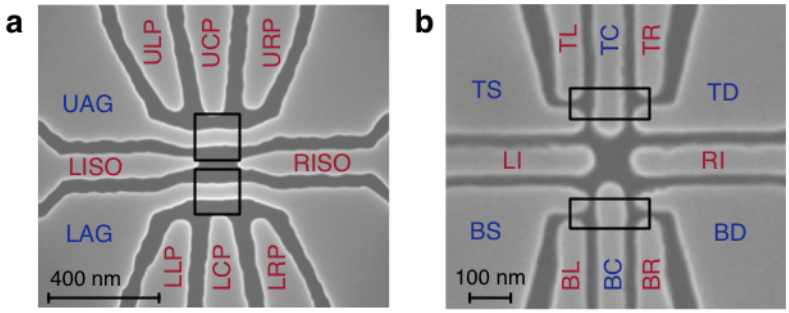

Figure 3.1: SEM images of **(a)** a gated-wire device and **(b)** a SWAG device. The black rectangles show the position of the donor implantation windows.

3.1 Implanted devices

Both gated-wire and split-wire accumulation gate (SWAG) devices (see Sec. 2.1) are implanted for use in donor-dot experiments. Either phosphorus (P) or antimony (Sb) atoms are used as donors. All implants (regardless of device geometry and donor species) are done using ion beam implantation with a self-aligned technique. During device fabrication, after the poly-silicon gates have been formed using electron-beam lithography followed by selective dry etching, a poly methyl-methacrylate (PMMA) mask is deposited on top of the device gates in order to limit the implantation to certain areas of the device. These implant windows are illustrated by black boxes in Fig. 3.1. When the device is exposed to an ion beam, the PMMA mask as well as the poly-silicon gates block the donor ions from reaching the Si/SiO_2 interface. Therefore, donors are only implanted in the etched regions situated within the implant window (dark grey areas situated within the black rectangles in Fig. 3.1).

The experiments shown in the rest of this chapter are performed on a gated-wire device implanted with Sb donors. An implantation energy of 120 keV and a fluence of 4×10^{11} cm^{-2} were used to implant the donors into the PMMA windows, on either side of both wires (see Fig. 3.1(a)). The donors were then activated with a 5 min long N_2 anneal at 900°C. From SRIM calculations [98], these implant parameters are expected to lead to roughly 42 donors in each implant window, situated at a mean depth of 37 nm below the Si/SiO_2 interface, with a vertical straggle of 17.7 nm.

The experiments discussed in subsequent chapters are performed on SWAG devices implanted with P donors. The devices were implanted in order for them to be used in donor-dot experiments, such as in Harvey-Collard *et al.* [54] and in

Rudolph *et al.* [53], though that is not how they were used in this work. These P implants were performed at 45 keV with a fluence of 4×10^{11} cm^{-2} into the implant windows shown in Fig. 3.1(b). The implants were then activated through a sequence of annealing processes: a 10 min O_2 anneal at 900°C, a 5 min N_2 at 900°C, and a 5 min N_2 anneal at 1000°C.

3.2 Triangulating the position of donors

Being able to determine the position of a donor atom is important in many different scenarios. As discussed previously, the success of experiments involving donors can be greatly affected by the relative position of the donors and the QDs involved. In other cases, the exact position of the donor is not of much importance, but knowing its general situation relative to the device gates can be used to determine how to most efficiently tune the system to the desired regime. Finally, proving that a donor is situated within the expected implant window can serve as an argument in favour of an observed feature being indeed due to the ionization of an implanted donor atom rather than to a nearby charge trap or impurity. In the following section, two different methods for determining the position of a donor are described: an intuitive method, and a numerical one. Both rely on the observation of the effect the ionization of the donor electron has on a nearby QD.

Fig. 3.2 shows the effect the ionization of a donor has on the stability diagram of a nearby QD. The data shown is for a gated-wire device implanted with Sb donors (see Sec. 3.1). The lower wire dot's charge transition lines are measured through transport and are typical of a single QD (see Sec. 2.3.2). However, as the voltages applied to the device gates are made more negative, a donor implanted near the QD becomes ionized. This causes a sudden change in the electrical environment of the QD and results in a visible break of the Coulomb blockade lines (highlighted by the red lines in Fig. 3.2). Another way of interpreting this system is as a double quantum dot (DQD), depicted schematically in Fig. 3.2(e), where the donor plays the role of one of the dots (D_1) and the lithographic dot is the other (D_2). The layout of this DQD differs from the one presented in Fig. 2.2(d) because only D_2 is situated on the path between the source and drain reservoirs. As a result of this, current between the source and drain is no longer limited to the triple points, and the charge transition lines of D_2 (blue lines in Fig. 2.2(e)) are visible. However, the charge transition lines of

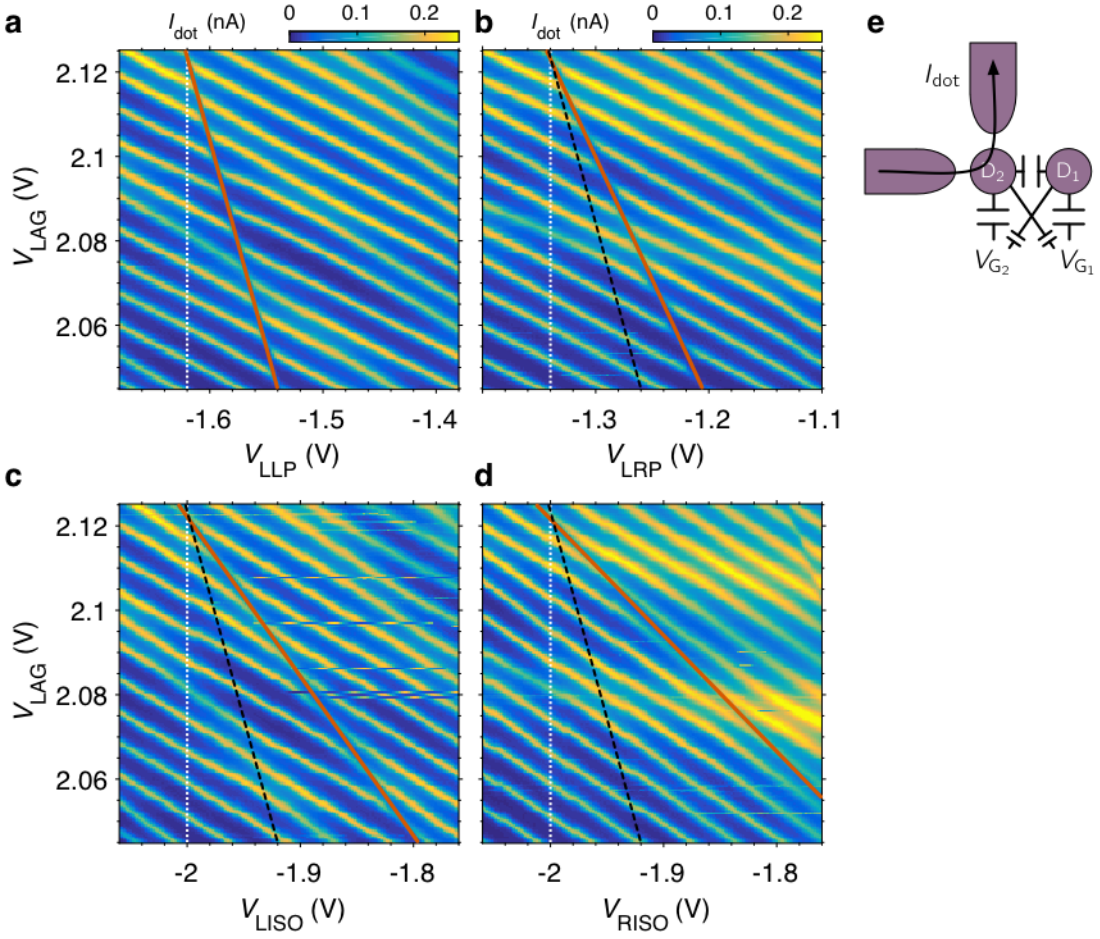

Figure 3.2: (a-d) Stability diagrams of the same QD-donor system, acquired using different pairs of gates. The white dotted lines correspond to identical line traces in each plot. The solid orange lines highlight the break in the dot's Coulomb blockade lines caused by a donor transition. The black dotted lines indicate the slope of the break from **(a)** and are used as visual guides to compare the slopes of the breaks between the plots. **(e)** Schematic of the "double quantum dot" system composed of a donor atom (D_1) and a lithographically defined QD (D_2). The two "QDs" are capacitively coupled to both gates (G_1 and G_2) as well as to each other. Transport between the source and drain reservoirs is possible through D_2.

D_1 and the interdot transition lines (red and purple lines in Fig. 2.2(e), respectively) will remain invisible unless a charge sensor is used. Because the charging energy of D_1 (the donor) is very large, only one charge transition is visible in the voltage range of interest.

The rest of this section concentrates on using the stability diagrams shown in Fig. 3.2 to extract the position of the donor causing the break in the Coulomb

blockade lines. Though a donor-dot system is used in this example, the methods presented are not limited to donors and can be adapted to triangulate the position of dots, donors, and defects in a wide variety of device layouts.

3.2.1 The intuitive method

The first method for determining the position of a donor is an intuitive one and works best for symmetrical device geometries (such as the gated-wire or SWAG devices). For all the stability diagrams shown in Fig. 3.2, the voltage on LAG is swept along the vertical axis, while the gate swept along the horizontal axis differs for each scan. Because the slope of the break in the CB lines (highlighted in red) is related to the capacitive coupling between the donor and the pair of gates swept [99], some information can be gleaned from the fact that the slope changes between the scans. In the example studied here, the slope of the break is significantly steeper for LLP and LRP than for LISO and RISO (see Fig. 3.1(a) for gate labelling). This indicates that the donor is more strongly coupled to the gates situated below the lower wire (LLP and LRP) than to those situated above it (LISO and RISO). It is, therefore, quite safe to assume that the donor studied is implanted below the lower wire. By observing that the slope of the break is steeper for LLP and LISO (which are situated on the left side of the device) than for LRP and RISO (which are situated on the right), respectively, similar reasoning can be used to conclude that the donor is implanted to the left of the centre plunger (LCP). The extent of the intuitive method, in this case, is to conclude that the donor is in the lower left quadrant of the bottom implant window shown in Fig. 3.1(a). Because all the gates are situated on the same plane at the surface of the sample, this method cannot provide any information about the depth at which the donor is implanted.

It is important to note that the slope of the lithographic dot lines is fairly similar between the plots shown in Fig. 3.2, indicating that the QD has a similar coupling to LLP, LRP, LISO, and RISO. Care must be taken in cases where this is not the case (i.e. in cases where there is a significant change in the slope of the QD transition lines between the scans) because, in these cases, the change in the slope of the break may not be entirely attributed to the change in the coupling between the donor to the gates being swept.

3.2.2 The numerical method

If a more precise knowledge of the donor position is required, the intuitive method described above can be expanded upon. Various methods of triangulating the position of a donor have already been reported, several of which rely, at least in part, on using capacitance models to reproduce experimental data [100, 101, 102]. The method used in this work was developed by Erik Nielsen and is similar to the one described in Foote *et al.* [102]. FastCap, a three-dimensional capacitance extraction program [103], is used to create a capacitance model of the device and calculate the expected stability diagrams. In the model, the device gates are represented by 200 nm thick metallic shapes, as shown in Fig. 3.3(a). The regions where a two-dimensional electron gas (2DEG) is present (i.e. the areas occupied by the source, drain, and dot) are represented by 5 nm thick metallic shapes, as shown in Fig. 3.3(b). The tops of these shapes are situated 35 nm below the bottom of the metallic gate shapes. The size of the rectangular dot is adjusted so that the spacing between the dot's Coulomb blockade lines calculated from the model is consistent with the spacing observed experimentally in Fig. 3.2. All the metallic shapes are considered as perfectly conducting, while all other areas are regarded as perfectly insulating. The model's computational domain is limited to a 4×2 μm area centred between the two wires. Any gate or 2DEG situated outside this domain is considered as too far away from the dot and the donor to have a significant impact on the relevant capacitances.

The donor is represented as a metallic sphere of variable size and position. For any chosen donor position, the capacitive model can be used to generate the expected stability diagrams. Several targets are used to determine how well these modelled stability diagrams reproduce the experimental ones shown in Fig. 3.2. These targets are: 1) the slope of the break in the Coulomb blockade lines, 2) a point along this break, and 3) the voltage by which the Coulomb blockade lines are shifted across the break. The *target error*, defined as the sum of the squared differences between the calculated and experimental target values, is then calculated and used to objectively compare potential donor positions. In order to determine the most likely position of a donor, a depth is chosen and the lateral position of the metallic sphere is rastered inside the implant window. For every point in the raster, stability diagrams are generated and the target error is calculated, as shown in Fig. 3.3(c). The

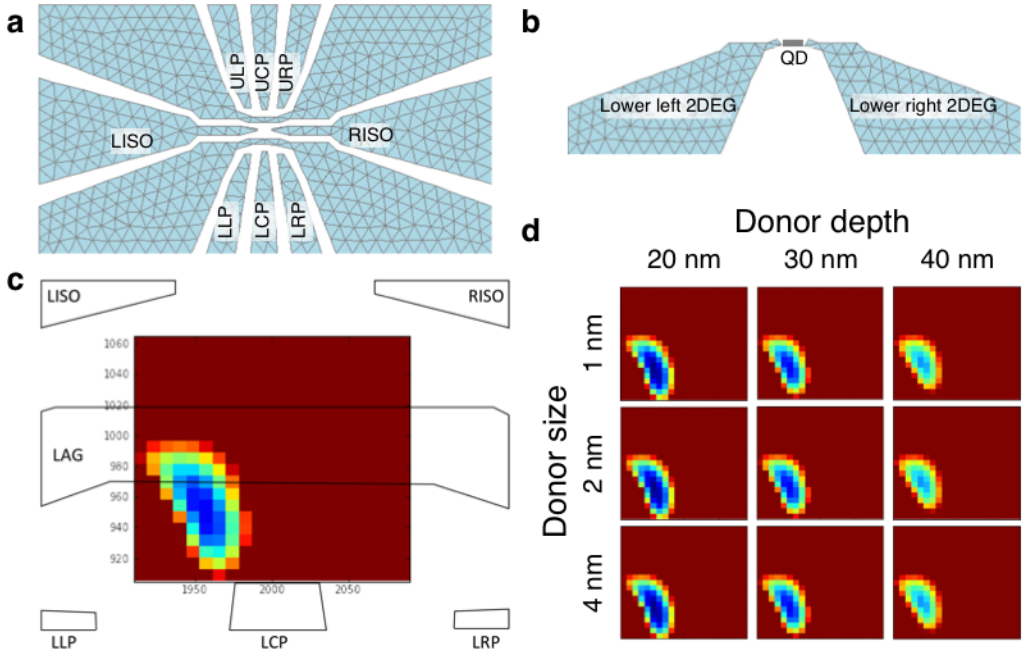

Figure 3.3: Results produced by Erik Nielsen. **(a)** Shape of the metallic gates used in the FastCap model. All gates have a thickness of 200 nm. **(b)** Shape of the metallic regions used to represent the QD, source and drain in the FastCap model. These regions are 5 nm thick and their top is situated 35 nm below the bottom of the gates shown in **(a)**. The donor is represented by a metallic sphere (not pictured) whose radius, position, and depth are changed during the calculation. **(c)** Target error (see text) calculated for different donor positions inside the implant window. Blue (red) areas have low (high) target errors and correspond to the most (least) likely positions for the donor studied. The results are for a donor with a 1 nm radius situated 30 nm below the SiO_2 layer. The black lines indicate the position of the device gates relative to the implant window. **(d)** Effect of the radius and depth of the donor on the target errors.

position with the smallest target error (darkest blue pixel) is then accepted as the most likely position of the donor studied. From Fig. 3.3(c), the calculations indicate that the donor is situated just below the wire and to the left of the LCP gate. This is consistent with conclusions reached using the intuitive method of triangulation discussed in Sec. 3.2.1.

It is worth noting that the radius of the metallic sphere used to represent the donor has little to no effect on the calculated donor position. This is clearly highlighted in Fig. 3.3(d), where each row corresponds to the target error calculated for a sphere with a different radius. As the radius is changed from 1 nm to 4 nm, there

is no visible change in the target error. It should also be noted that, because all the metallic gates and 2DEGs are on a plane at the surface of the device, this method does not offer much precision on the vertical position of the donor. In Fig. 3.3(d), the target error does decrease as the depth of the donor is changed over a large range from 20 nm to 40 nm below the Si/SiO_2 interface, but small changes in depth do not affect the target value enough to have much confidence in the results. However, it is reassuring that the choice of donor depth for the target error calculation does not seem to impact the lateral position extracted.

Finally, the numerical method presented here to extract the donor position may be improved by a more sophisticated method of choosing the shapes for the metallic structures representing the 2DEGs. Rather than replicating the shape of the gated wire for the source and drain 2DEGs and using a brick-shaped dot, as was done in the example presented here, more realistic geometries may be extracted by using tools such as COMSOL [104] or QCAD [105] to estimate the real extent of the 2DEGs.

3.3 Single-shot readout of a donor spin

As mentioned previously, single donor electrons in silicon have potentially long coherence times and are, therefore, promising candidates for qubits. An important requirement for any qubit is to be able to measure its state [10]. Because the devices used in this work are not equipped with microwave transmission lines or micro-magnets, the donor electrons cannot be coherently manipulated. However, such components are not required for demonstrating spin readout. The following section details a relatively simple pulsing technique that can be used to achieve single-shot readout of an individual donor electron spin.

In order to measure the spin of a donor electron, a spin selective tunnelling method can be used to achieve spin to charge conversion [38, 106, 107]. The donor transition line chosen for this experiment is shown in Fig. 3.4(a).[1] As discussed previously, ionizing the donor (in this case moving to more negative V_{LCP}) causes

[1] This particular donor is not the one studied in Sec. 3.2, but rather one situated farther away from the lithographic dot. This donor was chosen because, at the time this experiment was performed, the device gates were all wired to DC lines equipped with 80 MHz low-pass filters, making it impossible to perform experiments requiring fast pulsing. Because the tunnel rate between the donor and the lithographic dot is strongly dependent on the distance separating them, choosing a donor located farther away from the dot meant that the donor-dot tunnel rate was slow and that the following experiment could be performed despite the fact that the device wasn't wired to fast pulsing lines.

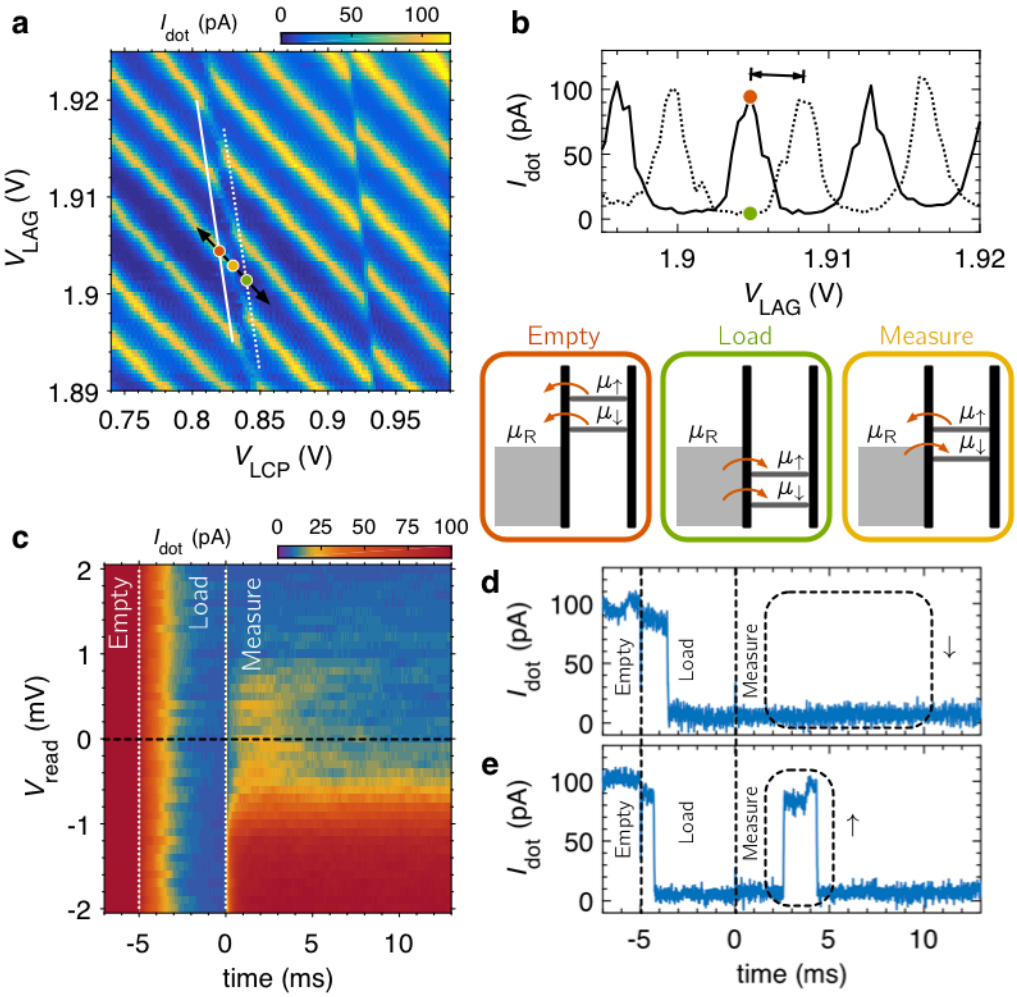

Figure 3.4: (a) Stability diagram showing charge transitions of a QD formed in the lower wire of a gated-wire device. The transition lines are offset by the ionization of Sb donors implanted nearby. The black arrow indicates the direction along which V_{LCP} and V_{LAG} are pulsed during the donor readout measurement. The coloured dots indicate the position of the *Empty* (red), *Load* (green), and *Measure* (yellow) points of the pulse. **(b)** Line traces taken along the solid (ionized donor) and dashed (neutral donor) white lines in **(a)**. **(c)** Time dependent current through the QD (averaged over 1000 single-shot traces) measured during the donor readout pulse. The *Empty* and *Load* points are kept constant, while the *Measure* voltage is scanned along the black arrow in **(a)**. $V_{\mathrm{read}} > 0$ is near the *Load* point, while $V_{\mathrm{meas}} < 0$ is near the *Empty* point. **(d-e)** Single-shot traces taken at $V_{\mathrm{meas}} = 0$ (black dashed line in **(c)**) when the spin of the donor electron is **(d)** anti-aligned and **(e)** aligned with the applied external magnetic field ($B_{\mathrm{ext}} = 2$ T).

the electrochemical potential ladder of the dot to suddenly shift down in energy. If there is a large capacitive coupling between the donor and the dot, this shift can correspond to a significant fraction of the dot's interline spacing. The black arrow in Fig. 3.4(a) is parallel to the QD transition line and therefore indicates the direction of constant electrochemical potential for the dot. Along this direction in voltage space, any change in the current of the QD is caused by a change in the occupation of the nearby donor. Fig. 3.4(b) shows line traces of the QD taken when the donor is neutral (dotted line) and when the donor is ionized (solid line). It is clear from these traces that the ionization of the donor shifts the electrochemical potential of the dot enough to switch the current from 0 pA when the donor is neutral (green dot) to its maximum value of 100 pA when the donor is ionized (red dot). In essence, the QD can be used as a charge sensor for the donor. In this experiment, the QD also serves as the reservoir for the donor electron, as illustrated in Fig. 3.2(e). However, in order to simplify the discussion, the reservoir for the donor electron is drawn as a fixed continuum of states in Fig. 3.4. For a more rigorous description of the QD electrochemical potentials involved, the reader can refer to Morello *et al.* [106].

In order to determine the spin of the electron on the donor, a large magnetic field of $B_{\text{ext}} = 2$ T is applied. In the presence of this magnetic field, the energy between the $|\uparrow\rangle$ and $|\downarrow\rangle$ states of the donor electron are split by the Zeeman energy $E_{\text{Z}} = g\mu_{\text{B}}B_{\text{ext}}$, where $g = 2$ is the electron g-factor in silicon and μ_{B} is the Bohr magneton. The donor spin readout experiment is performed by applying a three-level pulse to the system, as described in Morello *et al.* [107]. The voltage points of these levels are indicated by coloured dots in Fig. 3.4(a). First, during the *Empty* level of the pulse (red dot), the electrochemical potential ladder of the donor is raised enough for the donor to be ionized, regardless of the spin of its electron. The *Empty* level must be long enough compared to the donor-reservoir tunnel time for an electron to be emptied during every iteration of the pulse. A sharp increase in the current through the QD indicates that the donor was successfully emptied. Next, during the *Load* level (green dot), the energy levels of the donor are plunged so that both $\mu_{\uparrow}$ and $\mu_{\downarrow}$ are below μ_{R}, the electrochemical potential of the reservoir. This leads to an electron with a random spin being loaded onto the donor. The *Load* level must be long enough compared to the reservoir-donor tunnel time for it to be highly likely that an electron is loaded to the donor at every iteration of the pulse, but short enough compared to the spin relaxation time, T_1, to avoid all the $|\uparrow\rangle$ states

decaying to $|\downarrow\rangle$. The current through the QD suddenly dropping from 100 pA to 0 pA serves as confirmation that an electron was loaded to the donor. Finally, during the *Measure* level (yellow dot), the system is tuned so that $\mu_\downarrow < \mu_R < \mu_\uparrow$. This means that an electron in the $|\downarrow\rangle$ ground state will be blockaded and remain on the donor, leading to no change in the current through the QD. Meanwhile, an electron in the $|\uparrow\rangle$ excited state will tunnel to the reservoir and eventually be replaced by an electron in the $|\downarrow\rangle$ state. This will result in a single current blip of variable length during the *Measure* level. Typical single-shot traces measured for donor electrons in the ground and excited states are shown in Fig. 3.4(d) and Fig. 3.4(e), respectively.

Fig. 3.4(c) shows the scan performed to adjust the position of the *Measure* level of the spin readout pulse. Each line of the scan is an average of 1000 single-shot time traces. The *Load* and *Empty* levels are kept constant throughout the scan, while the voltage point of the *Measure* level is swept along the black arrow in Fig. 3.4(a). The vertical axis of the scan indicates the position of the read level, expressed in units of V_{LCP} relative to the mid-way point between the *Empty* and *Load* points. At the bottom of the scan, the *Measure* level is too high and the donor electron is emptied during every iteration of the pulse, regardless of its spin. This is evidenced by the high current through the dot during the *Measure* level. At the top of the scan, the *Measure* level is too low and the donor electron remains blockaded even if it is in the excited state. This leads to the low current signal observed. For *Measure* levels near $V_{read} = 0$, conditions for spin-selective tunnelling are met. The averaging of many single-shot traces such as the ones shown in Fig. 3.4(d-e) leads to the moderate-current feature visible at the beginning of the *Measure* level. This feature is sometimes referred to as a "spin bump" and it indicates the range of voltage points at which spin readout can be performed.

Once spin readout has been established, pulsing schemes similar to the one described can be used to glean a variety of information about the donor and the system in general. For example, the spin relaxation time, T_1, can be studied by varying the duration of the *Load* level of the pulse [107]. The pulse described above can also be used to initialize the donor electron in the ground state for single qubit experiments [92].

Chapter 4

Modelling tunnel rates for automated tuning of quantum dots

In recent years, significant effort has been put into increasing the number of semiconductor QDs fabricated on a single device [70, 108, 109, 110, 111, 112, 113]. Slight variations in the potential landscape seen by these QDs (caused, for example, by the presence of charge impurities or by slight differences in gate fabrication) means that they must each be tuned individually. This greatly increases the time and effort required to tune up these systems.

Unsurprisingly, the increased difficulty in tuning has lead to great interest in computer-automated tuning. Thus far, computer-automation has been successfully used to tune QDs to the single electron regime [66], as well as to fine tune QD parameters such as the inter-dot tunnel coupling [114, 115] and the dot-lead tunnel rates [116]. These methods used to tune the tunnel rates assumed that there was a dedicated "barrier gate" and used iterative approaches to reach the desired tunnel rate value (i.e. change barrier gate voltage, adjust other gates to preserve dot occupation, measure new tunnel rate, repeat). These iterative approaches can become quite time consuming if the tunnel rate must be adjusted over a large range of values and the number of iterations required to reach the target becomes large. Being able to predict how the tunnel rate changes with gate voltage would reduce the number of iterations needed to reach the goal and, therefore, reduce the time needed to tune up QD devices. Having access to a tunnel rate model would also be extremely useful in cases where the device design does not include a dedicated barrier gate.

The following chapter presents a simple model that can be used to predict how the dot-lead tunnel rate is affected by changes in the voltage applied to the surrounding gates. The theoretical basis for the model is explained in Sec. 4.1. In Sec. 4.2, the measurements needed to extract model parameters are detailed and the model is tested on a split-wire accumulation gate (SWAG) device from Sandia. It is demonstrated that the model succeeds in predicting the tunnel rate over a range of more than two orders of magnitude. Because the model makes no assumptions regarding device geometry and gate layout, it can be applied to a wide variety of experiments.

Contributions: The theoretical model for predicting tunnel rates was developed by N.T. Jacobson, with input from A.M. Mounce and C.B.-O. All the device tuning, data acquisition, and analysis of the results presented in this chapter were performed by C.B.-O.

4.1 Theoretical model

The theoretical model presented in this section aims to predict how the tunnel rate between a reservoir and a dot will be affected when the voltages on surrounding electrostatic gates are changed. The value of interest is Γ, the tunnel rate between the QD and its single reservoir. For simplicity, the system considered has only three gates (G_0, G_1, and G_2), as shown in Fig. 4.1(a), though the model can easily be generalized to include an arbitrary number of gates, n. Adjusting the voltages V_i on the gates G_i affects the QD occupation as well as the tunnel rate between the dot and the lead. Because the tunnel rate can only be considered when the number of electrons on the QD is changing, the area of interest is the electron transition between the N and $N+1$ charge stability regions which occurs when the electrochemical potential level of this transition is aligned with the Fermi level of the reservoir. Assuming a linear capacitance model, this electron transition corresponds to a straight line in a typical charge stability diagram where two gate voltages are swept and all other gate voltages are kept constant (Fig. 4.1(b)). In the three-dimensional voltage space considered in this example, the charge transition occurs along a two-dimensional

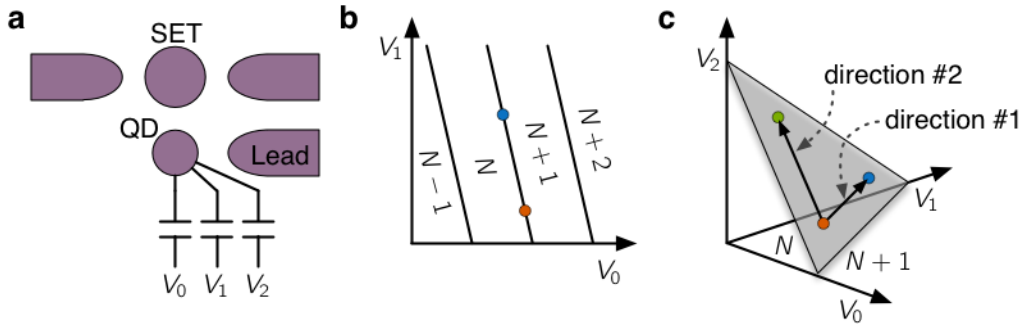

Figure 4.1: (a) Schematic representation of the device considered in the tunnel rate experiment. The QD is connected to a single reservoir (lead) and is capacitively coupled to various gates. A SET is used to charge-sense the QD. **(b)** 2D stability diagram for the device presented in **(a)**. The number of electrons in each charge stability region is indicated. **(c)** 3D representation of the Coulomb blockade plane between the N-electron (below the plane) and N+1-electron (above the plane) charge stability regions. The red and blue dots are along the the direction of constant V_2 (and correspond to the dots in **(b)**), while the red and green dots are along the direction of constant V_1.

plane, as shown in Fig. 4.1(c). This plane is parametrized by

$$\boldsymbol{\beta} \cdot \Delta \mathbf{V} = \sum_i \beta_i \Delta V_i = 0\,, \tag{4.1}$$

where $\Delta\mathbf{V}$ is a vector lying on the charge transition plane and β_i is the energy lever arm of the gate G_i. Since the energy of the QD is constant everywhere on the charge transition plane, $\boldsymbol{\beta}$ can be seen as a vector that is normal to this plane, indicating the direction of swiftest change in the QD's electrochemical potential.

Assuming that the dot-lead tunnel rate depends exponentially on gate voltage [117], the tunnel rate can be expressed as

$$\Gamma(\mathbf{V}) = \Gamma_0\, e^{\mathbf{T}\cdot\mathbf{V}} = \Gamma_0 \exp\left[\sum_i T_i V_i\right],$$

where Γ_0 is a reference tunnel rate measured at the voltage origin, and T_i is the "tunnel rate lever arm" for the gate G_i. It is important to note that the voltage at which Γ_0 is measured can be changed without affecting the model or the values of

T_i:

$$\begin{aligned}\Gamma(\mathbf{V}') &= \Gamma_0 \exp\left[\sum_i T_i(V_i + \Delta V_i)\right] \\ &= \Gamma_0 \exp\left[\sum_i T_i V_i\right] \exp\left[\sum_i T_i \Delta V_i\right] \\ &= \Gamma_0' \exp\left[\sum_i T_i \Delta V_i\right]. \end{aligned} \tag{4.2}$$

In the expression above, the new reference tunnel rate, $\Gamma_0' = \Gamma(\mathbf{V})$, is measured at $\mathbf{V}$, and the tunnel rate at point $\mathbf{V}'$ is calculated from the voltage offset $\Delta\mathbf{V} = \mathbf{V}' - \mathbf{V}$. As both $\mathbf{V}$ and $\mathbf{V}'$ are points on the charge transition plane, $\Delta\mathbf{V}$ is a vector that lies on the plane.

Because the concept of a tunnel rate only exists at a charge transition, as mentioned above, the constraint that $\mathbf{T}$ must lie on the charge transition plane is added:

$$\boldsymbol{\beta} \cdot \mathbf{T} = 0. \tag{4.3}$$

Adding this constraint means that, in the model, the charge transition can be thought of as a slightly broadened plane, and that any slight deviation in a direction perpendicular to this plane will not result in a change in tunnel rate. This assumption is reasonable so long as the slight deviation away from the plane does not add or remove discrete energy levels from the energy window probed by the chosen tunnel rate measurement.

The fact that the tunnel rate measurements are restricted to the charge transition plane reduces the problem from three dimensions down to two and allows Eq. (4.2) to be simplified. Indeed, from Eq. (4.1) it can be equated that

$$\begin{aligned}\Delta V_2 &= -\frac{\beta_0}{\beta_2}\Delta V_0 - \frac{\beta_1}{\beta_2}\Delta V_1 \\ &= -\alpha_{02}\Delta V_0 - \frac{\alpha_{02}}{\alpha_{01}}\Delta V_1\,, \end{aligned} \tag{4.4}$$

where $\alpha_{ij} = \beta_i/\beta_j$ is the lever arm ratio between gates G_i and G_j. Similarly, from Eq. (4.3) it is possible to write

$$\begin{aligned} T_2 &= -\frac{\beta_0}{\beta_2}T_0 - \frac{\beta_1}{\beta_2}T_1 \\ &= -\alpha_{02}T_0 - \frac{\alpha_{02}}{\alpha_{01}}T_1 \,. \end{aligned} \tag{4.5}$$

Using Eq. (4.4) and Eq. (4.5), Eq. (4.2) can be rewritten in the following way:

$$\begin{aligned} \ln\left(\Gamma(\mathbf{V})/\Gamma_0\right) &= T_0\Delta V_0 + T_1\Delta V_1 + T_2\Delta V_2 \\ &= T_0\Delta V_0 + T_1\Delta V_1 + \left(\alpha_{02}T_0 + \frac{\alpha_{02}}{\alpha_{01}}T_1\right)\left(\alpha_{02}\Delta V_0 + \frac{\alpha_{02}}{\alpha_{01}}\Delta V_1\right) \\ &= \begin{pmatrix} T_0 & T_1 \end{pmatrix} \begin{pmatrix} 1+\alpha_{02}^2 & \alpha_{02}^2/\alpha_{01} \\ \alpha_{02}^2/\alpha_{01} & 1+(\alpha_{02}/\alpha_{01})^2 \end{pmatrix} \begin{pmatrix} \Delta V_0 \\ \Delta V_1 \end{pmatrix} . \end{aligned} \tag{4.6}$$

From the equation above it is clear that, in order to use this tunnel rate model in a three-dimensional voltage space, the tunnel rate lever arms T_i for two gates as well as the lever arm ratios α_{ij} for two pairs of gates must first be extracted. More generally, in a n-gate voltage space, one would have to have access to the following parameters in order to use the model:

1. The tunnel rate lever arm for $n-1$ gates;
2. The lever arm ratio between $n-1$ pairs of gates, in which each gate is represented at least once;
3. The value of the tunnel rate measured at a known reference voltage on the electron transition plane.

The rest of this section details how to extract α_{ij} and T_i from experimental data.

4.1.1 Extracting lever arm ratios

The lever arm ratio α_{ij} between gates G_i and G_j can easily be extracted from a 2D stability diagram taken while sweeping the voltage applied to these two gates and keeping all other gate voltages constant. Fig. 4.1(b), for example, shows a stability diagram taken by sweeping V_0 and V_1 while keeping V_2 constant. Using Eq. (4.4), it can be written that $\Delta V_1 = -\alpha_{01}\Delta V_0$ when $\Delta V_2 = 0$. Therefore, the slope of the charge

transition line in the V_0-V_1 plane is equal to $-\alpha_{01}$. The lever arm ratios between all other pairs of gates can be extracted in a similar manner.

4.1.2 Extracting tunnel rate lever arms

Extracting the tunnel rate lever arms requires significantly more work than was needed for the lever arm ratios. If $n-1$ T_i parameters are to be extracted, it will be necessary to measure how the tunnel rate changes when the voltage is swept along $n-1$ linearly independent directions along the electron transition. In the case of the 3D voltage space considered, the tunnel rate will need to be measured along two different directions on the 2D charge transition plane. For simplicity, the first direction chosen is $\Delta V_1 = -\alpha_{01}\Delta V_0$ with $\Delta V_2 = 0$ (direction #1 in Fig. 4.1(c)) and the second direction is $\Delta V_2 = -\alpha_{02}\Delta V_0$ with $\Delta V_1 = 0$ (direction #2 in Fig. 4.1(c)). Along the first direction, Eq. (4.6) becomes:

$$\begin{aligned}\ln\left(\Gamma(\mathbf{V})/\Gamma_0\right) &= \begin{pmatrix} T_0 & T_1 \end{pmatrix} \begin{pmatrix} 1+\alpha_{02}^2 & \alpha_{02}^2/\alpha_{01} \\ \alpha_{02}^2/\alpha_{01} & 1+(\alpha_{02}/\alpha_{01})^2 \end{pmatrix} \begin{pmatrix} \Delta V_0 \\ -\alpha_{01}\Delta V_0 \end{pmatrix} \\ &= \left(T_0 - \alpha_{01}T_1\right)\Delta V_0 \\ &= \lambda_{01}\Delta V_0 \,.\end{aligned}$$

In the equation above, λ_{01} is simply the slope of the tunnel rate vs ΔV_0 along direction #1 (on a log-linear plot). Along the second chosen direction, Eq. (4.6) becomes:

$$\begin{aligned}\ln\left(\Gamma(\mathbf{V})/\Gamma_0\right) &= \begin{pmatrix} T_0 & T_1 \end{pmatrix} \begin{pmatrix} 1+\alpha_{02}^2 & \alpha_{02}^2/\alpha_{01} \\ \alpha_{02}^2/\alpha_{01} & 1+(\alpha_{02}/\alpha_{01})^2 \end{pmatrix} \begin{pmatrix} \Delta V_0 \\ 0 \end{pmatrix} \\ &= \left[\left(1+\alpha_{02}^2\right)T_0 + \left(\alpha_{02}^2/\alpha_{01}\right)T_1\right]\Delta V_0 \\ &= \lambda_{02}\Delta V_0 \,.\end{aligned}$$

Similarly to λ_{01}, λ_{02} is merely the slope of the tunnel rate vs ΔV_0 along direction #2 (on a log-linear plot). From the definitions of λ_{01} and λ_{02} given above, we have:

$$\begin{pmatrix} \lambda_{01} \\ \lambda_{02} \end{pmatrix} = \begin{pmatrix} 1 & -\alpha_{01} \\ 1+\alpha_{02}^2 & \alpha_{02}^2/\alpha_{01} \end{pmatrix} \begin{pmatrix} T_0 \\ T_1 \end{pmatrix} \,. \tag{4.7}$$

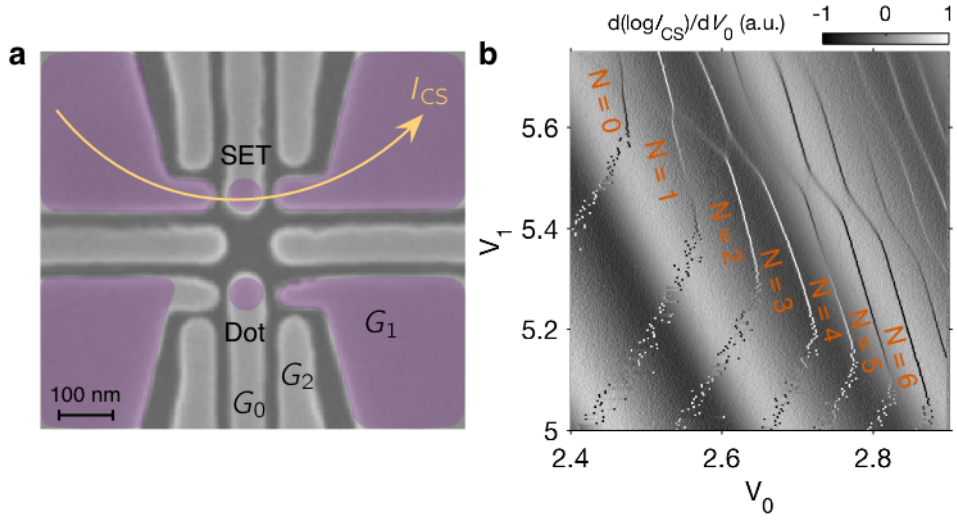

Figure 4.2: (a) SEM image of a device similar to the one used for the tunnel rate experiment. The purple shading indicates the approximate position of the two-dimensional electron gas accumulated at the interface of the SiO_2 layer and the enriched ^{28}Si substrate. A SET is formed in the upper wire and is used as a charge sensor (CS) for the single QD formed in the lower wire. The left lead is receded so that the QD is only tunnel-coupled to the right lead. **(b)** Charge stability diagram of the device shown in **(a)** as a function of the voltages V_0 and V_1 applied to the gates G_0 and G_1, respectively. The voltage applied to G_2 is kept constant at $V_2 = -2.75$ V. The number of electrons in each charge stability region is indicated in red.

From the equation above it is clear that, once λ_{ij} and α_{ij} have been measured, it becomes a simple matter of inverting a 2x2 matrix to extract all the needed T_i parameters.

4.2 Experimental results

In order to test the tunnel rate model described in Sec. 4.1, a SWAG device from Sandia (see Sec. 2.1) similar to the one shown in Fig. 4.2(a) is used. A single QD is formed in the lower wire underneath the centre accumulation gate, G_0, and is connected to a single reservoir underneath the right accumulation gate, G_1. The only other gate considered in the following experiment is the right depletion gate, G_2. A SET is formed in the upper wire and is used to charge sense the QD formed in the lower wire (see Sec. 2.3.4). Fig. 4.2(b) shows a charge stability diagram of the device tuned to the few electron regime. The speckling of the charge transition lines occurs

when the tunnel rate of the transition is similar to or smaller than the scanning rate of the measurement. The speckling appears to the left of where its corresponding transition line should be because the scan was taken by sweeping V_0 from right to left. The following experiments concentrate on the transitions between the $N = 2$ and $N = 3$ as well as between the $N = 3$ and $N = 4$ charge stability regions, which will hereby be referred to as the $N = 3$ and $N = 4$ transitions, respectively.

As described in Sec. 4.1.2, before the model can be used to predict tunnel rates, the tunnel rate lever arms must first be extracted by measuring how the tunnel rate changes when the measurement point is moved in different directions along the charge transition plane. Though pulsed gate spectroscopy (described in Sec. 2.3.7) does give a quick estimate of the tunnel rate, extracting a precise value from these scans is more challenging. Because of this, the dot-lead tunnel rate is instead measured using a method similar to the one described in Botzem *et al.* [118]. This method consists in forcing the system to switch repeatedly between charge states while measuring the time-dependent state of the QD. To do this, a square-wave voltage pulse is applied to V_0 (see Fig. 4.3(b)) and an oscilloscope is used to obtain the SET response, averaged over 50 000 periods. When the square pulse is centred on the charge transition, as illustrated by the blue dots in Fig. 4.3(a), a decaying time trace is observed (see Fig. 4.3(c)). Performing the same measurement in a region of constant QD occupation (between the red dots in Fig. 4.3(a)) allows the background SET signal (shown in Fig. 4.3(d)) to be subtracted from this raw tunnelling data, yielding the portion of the signal attributed solely to the QD's response to the square pulse, as shown in Fig. 4.3(e). A simple exponential decay can now be fit to the QD response signal in order to extract the load and unload tunnel times:

$$V(t) = \begin{cases} B_1 - A \exp\left[-t/t_\mathrm{u}\right] & \text{for } t < T_\mathrm{pulse}/2 \\ B_2 + A \exp\left[-(t - T_\mathrm{pulse}/2)/t_\mathrm{l}\right] & \text{for } t \geq T_\mathrm{pulse}/2 \end{cases} \tag{4.8}$$

In the equation above, T_pulse is the period of the square-wave pulse, t_u is the unload time and t_l is the load time. The offset B and amplitude A of the signal depend on the instrumental setup and the sensitivity of the SET and are irrelevant to the rest of the analysis.

Keeping V_2 constant while varying V_0 and V_1 in such a way as to remain at the electron transition allows the lever arm ratio α_{01} to be measured, as shown in

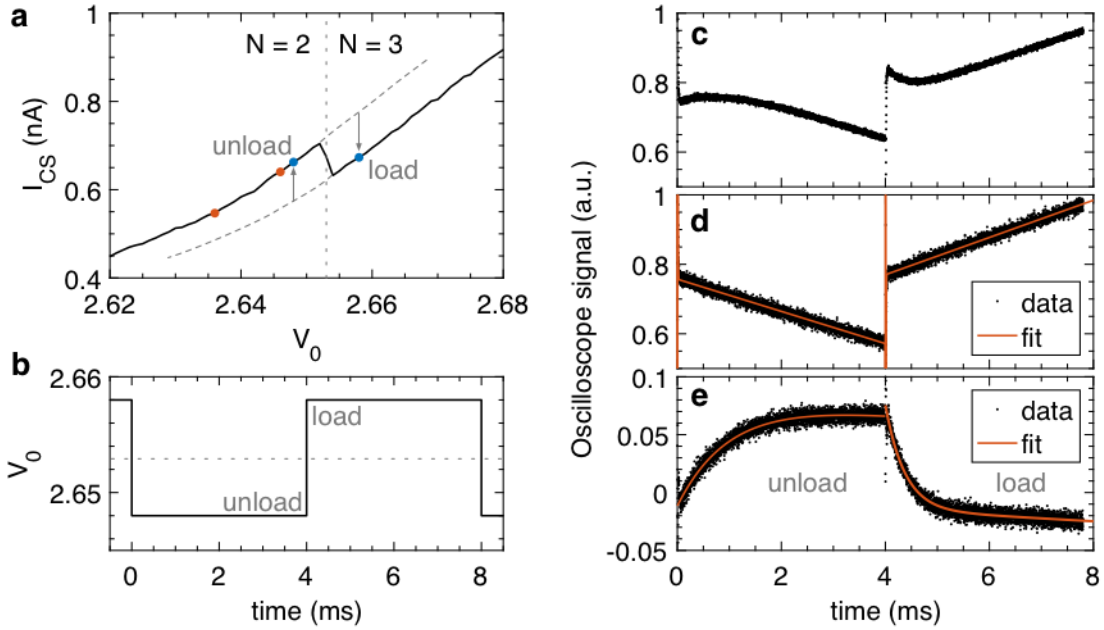

Figure 4.3: (a) SET response as V_0 is swept across the $N = 3$ electron transition line ($V_1 = 5.3$ V in Fig. 4.2.**b**). **(b)** Voltage pulse applied to G_0 in order to measure the tunnel rate. **(c)** SET response observed when V_0 is pulsed across the transition line, between the blue dots in **(a)**. **(d)** SET response observed when V_0 is pulsed far from the transition line, between the red dots in **(a)**. **(e)** Tunnelling data obtained after subtracting the fit to the background SET signal (red line in **(d)**) from the raw tunnelling data shown in **(c)**. The red line is a fit to the data.

Fig. 4.4(a). Meanwhile, measuring the tunnel rate at various points along this line, using the pulsing method described above, informs the user on how the tunnel rate changes along this direction of voltage space, as shown in Fig. 4.4(b). Performing a fit to these tunnel rates yields λ_{01}, as described in Sec. 4.1.2. Repeating the same procedure, this time keeping V_1 constant while varying V_0 and V_2 to move along the electron transition, allows α_{02} and λ_{02} to be extracted. The values of α_{ij} and λ_{ij} measured for the $N = 3$ and $N = 4$ transitions are presented in Tab. 4.1(a). Because no assumptions are made regarding whether or not the load and unload tunnel rates are equal, or even whether they vary in a similar manner with voltage, distinct $\lambda_{ij,\mathrm{u}}$ and $\lambda_{ij,\mathrm{l}}$ are extracted for the unload and load cases, respectively.

Once $\alpha_{01}, \alpha_{02}, \lambda_{01}$, and λ_{02} have been obtained, calculating T_0 and T_1 from Eq. (4.7) is straightforward. T_2 is then calculated using Eq. (4.5). The tunnel rate lever arms calculated for the $N = 3$ and $N = 4$ transitions are listed in Tab. 4.1(b). Once again,

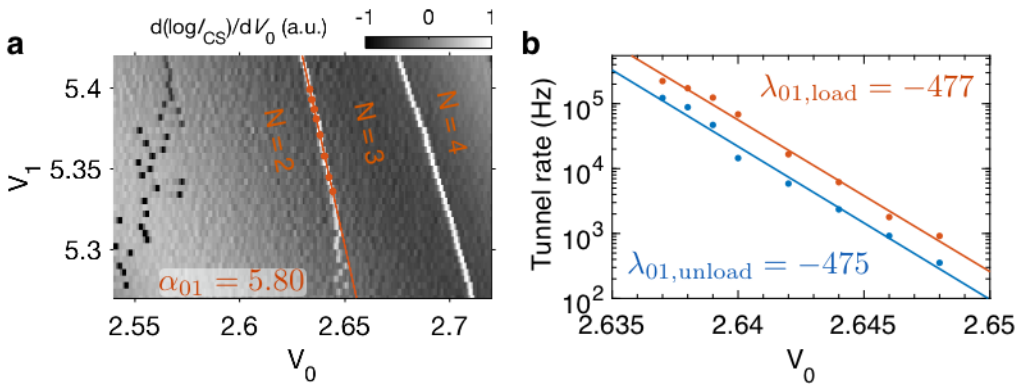

Figure 4.4: (a) Zoom in the stability diagram from Fig. 4.2(b) to show the area of interest on the $N = 3$ transition line. The red data points show voltages at which the tunnel rate was measured. The solid line is a fit to these voltages, yielding a lever arm ratio of $\alpha_{01} = 5.80$. **(b)** Unload (blue points) and load (red points) tunnel rates measured at the voltages indicated in **(a)**. The solid lines are fits to the data, allowing λ_{01} to be extracted.

(a)

	$N = 3$	$N = 4$
α_{01}	5.80 ± 0.22	4.88 ± 0.22
α_{02}	4.27 ± 0.03	4.11 ± 0.03
$\lambda_{01,\mathrm{u}}$	-475 ± 9	-373 ± 41
$\lambda_{01,\mathrm{l}}$	-477 ± 55	-378 ± 31
$\lambda_{02,\mathrm{u}}$	-144 ± 8	-141 ± 5
$\lambda_{02,\mathrm{l}}$	-162 ± 9	-118 ± 6

(b)

	$N = 3$	$N = 4$
$T_{0,\mathrm{u}}$	-20.3 ± 1.1	-21.8 ± 2.0
$T_{0,\mathrm{l}}$	-21.2 ± 1.8	-20.8 ± 1.7
$T_{1,\mathrm{u}}$	78.4 ± 3.2	72.0 ± 8.6
$T_{1,\mathrm{l}}$	78.5 ± 9.6	73.3 ± 6.8
$T_{2,\mathrm{u}}$	29.0 ± 1.7	28.9 ± 1.2
$T_{2,\mathrm{l}}$	32.9 ± 2.1	23.6 ± 1.4

Table 4.1: Tunnel rate parameters and lever arms calculated for the $N = 3$ and $N = 4$ transitions. The u and l suffixes indicate that the parameters relate to unload and load rates, respectively. **(a)** α_{ij} and λ_{ij} parameters extracted from experimental data. The errors correspond to 95% confidence bounds on the fit to the data. **(b)** Tunnel rate lever arms calculated from the parameters listed in **(a)**.

different values are calculated for the unload and load cases. It is worth noting, however, that for most gates $T_{i,\mathrm{u}}$ and $T_{i,\mathrm{l}}$ are quite similar, indicating that the unload and load rates do, in fact, vary in a similar manner when the voltage is changed. Also, the tunnel rate lever arms are somewhat comparable between the two electron transitions measured. This seems to indicate that the position and the size of the QD were not significantly impacted by the addition of a single electron.

Before moving on to using the tunnel rate model, it is interesting to take a closer look at the values calculated for the tunnel rate lever arms to see what they reveal about the system. The first observation is that T_1 is by far the largest in absolute value. This indicates that G_1 should be adjusted first if the goal is to effect a large change in tunnel rate. G_0, on the other hand, is the gate that will have the smallest effect on the tunnel rate. Both T_1 and T_2 are positive, which means that the tunnel rate will increase when G_1 and G_2 are made more positive. This can be understood by imagining that applying a large positive voltage to these gates, which are both to the right of the dot, would likely tend pull it out from under G_0 towards the lead (which is also to the right of the dot). In the case of G_1, a larger positive voltage could also mean a larger area occupied by the two-dimensional electron gas, i.e. the lead would extend out further towards the dot. A final observation is that T_0 is negative, indicating that the tunnel rate will decrease when G_0, the gate directly above the QD, is made more positive. This is to be expected since a larger positive voltage on G_0 would lead to a larger confinement potential for the electrons in the dot. These conclusions may seem obvious since they were reached using simple "hand-wavy" arguments regarding the geometry of the device. Nevertheless, it is reassuring to have this simple model confirm what intuition has taught us to expect.

Now that the tunnel rate lever arms have been calculated, the model is ready to be used. Fig. 4.5 compares measured tunnel rates (dots) to ones predicted by the model (solid lines) along different directions in voltage space for the $N = 3$ (Fig. 4.5(a,c,e)) and $N = 4$ (Fig. 4.5(b,d,f)) transitions. As an initial test, Eq. (4.2) is used to calculate the tunnel rate along direction #1 (where V_2 is kept constant) and direction #2 (where V_1 is kept constant). These are shown as red and blue results, respectively. Because these data points are the ones used to extract the parameters for the model, it is unsurprising that the model predictions fit the experimental results well. Therefore, to truly put the model to the test, the tunnel rates are measured along three new directions on the voltage plane (yellow, purple and green data in Fig. 4.5). We see that, for all the directions probed, the model predicts well how the tunnel rate changes. Even when the tunnel rate is measured far from where the model is calibrated (green data in Fig. 4.5(b)) or at voltages where the rate has changed by more than two orders of magnitude, the model continues to perform well and the measured tunnel rates often fall within the error on the predicted value (shaded areas around the solid lines in Fig. 4.5). Because Eq. (4.2) is derived by assuming a

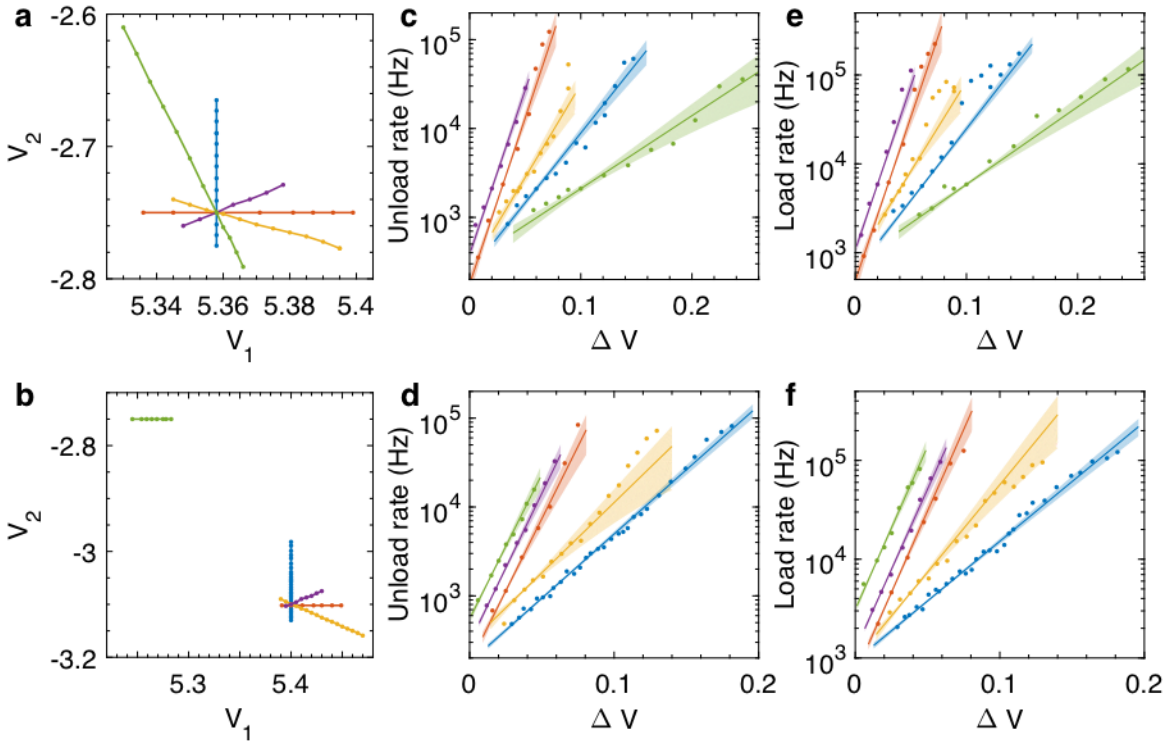

Figure 4.5: (a-b) Points on the $N = 3$ **(a)** $N = 4$ **(b)** charge transition planes where the tunnel rate is measured, projected onto the V_1-V_2 plane. V_0 is also adjusted in order to remain at the electron transition. The red data sets are used to extract α_{01} and λ_{01}, while the blue data sets are used to extract α_{02} and λ_{02}. **(c-f)** Unload **(c-d)** and load **(e-f)** tunnel rates measured at different points on the $N = 3$ **(c,e)** and $N = 4$ **(d,f)** transitions. The data is offset horizontally for clarity. The colours correspond to the different directions probed along the Coulomb blockade planes shown in **(a)** and **(b)**. The points are experimentally measured tunnel rates, while the lines are the corresponding rates predicted by the model. The shaded areas correspond to the error bars on the model predictions.

linear capacitance model, the predicted tunnel rates are expected to remain reliable so long as the voltages are kept within a range where the lever arm ratios, α_{ij}, are constant, i.e. the electron transition lines are straight. If the voltages are changed in such a way as to significantly displace or deform the QD, the model parameters will need to be recalibrated.

Chapter 5

Calibration and coherent quantum control of singlet-triplet qubits

Singlet-triplet (ST) qubits are generally composed of two electrons in a double quantum dot [20, 45]. They are encoded in the singlet and non-polarized triplet states and are driven using the exchange energy, which arises when the electrons are in the same dot and their wave functions overlap, and the difference in Zeeman energy, which dominates when the two electrons are confined to separate dots [56]. Though spin-orbit effects are generally weak in bulk silicon [61], recent work has shown that strong interface confinement can lead to spin-orbit effects large enough to provide this difference in Zeeman energy and allow the qubit to be driven without the need for external components such as micromagnets [59, 60]. Encoding the qubit in the combined spin state of two electrons allows some of the challenges associated with spin-1/2 qubits to be overcome. The presence of two distinct driving energies means that the ST qubit naturally lends itself to all-electrical control schemes, forgoing the need for oscillating magnetic fields and the microwave waveguides that produce them. In turn, this all-electrical control allows two ST qubits to be entangled via capacitive coupling, rather than requiring exchange coupling as is the case for spin-1/2 qubits [63].

In the previous chapters of this thesis, the usual methods used for tuning and characterizing quantum dot devices were presented. If a user is fortunate enough to have a device that can be tuned to the few electron regime while simultaneously exhibiting tunnel rates and valley splittings within the desired ranges, the system is finally ready for advanced pulsing experiments to be attempted. The following

chapter demonstrates how the spin state of two electrons in a Si-MOS double quantum dot can be used as a singlet-triplet qubit, and is organized as follows. Sec. 5.1 presents the experimental setup used and lists technical details that must be carefully considered in order to achieve reliable pulsing and reasonably fast acquisition times. Sec. 5.2 introduces theoretical concepts, such as the ST encoding and the qubit Hamiltonian, and discusses how the spin-orbit coupling can be used to drive qubit rotations. Sec. 5.3 discusses the typical construction of the qubit control pulses that will be used throughout the rest of the thesis. The three subsequent sections are dedicated to pulsing experiments that allow the user to calibrate the qubit initialization and readout (Sec. 5.4), identify the slow and rapid adiabatic transfer regimes (Sec. 5.5), and measure the tunnel coupling between the two quantum dots (Sec. 5.6). In the last two sections of this chapter, two different methods for performing arbitrary single-qubit rotations are demonstrated. The first method, discussed in Sec. 5.7, performs rotations around two non-orthogonal axes by rapidly pulsing between two regimes: one where the electron wave functions overlap, and the other where they are separate. The second method, detailed in Sec. 5.8, resembles electron spin resonance [39] and is achieved by varying the strength of the exchange coupling on resonance with the spin-orbit-driven rotation frequency of the qubit. Evidence of the qubit being pushed to the strongly-driven resonant regime is also presented.

Contributions: M.J. Curry and T.D. England designed the current-biased heterojunction bipolar transistor amplification circuit and provided guidance during its optimization and use. The data acquisition code used to acquire all the data presented in this chapter was written by C.B.-O. using some sections of code written by P. Harvey-Collard. N.T. Jacobson provided invaluable assistance regarding theoretical aspects of this work. All the device tuning, data acquisition, and analysis of results presented in this chapter was performed by C.B.-O.

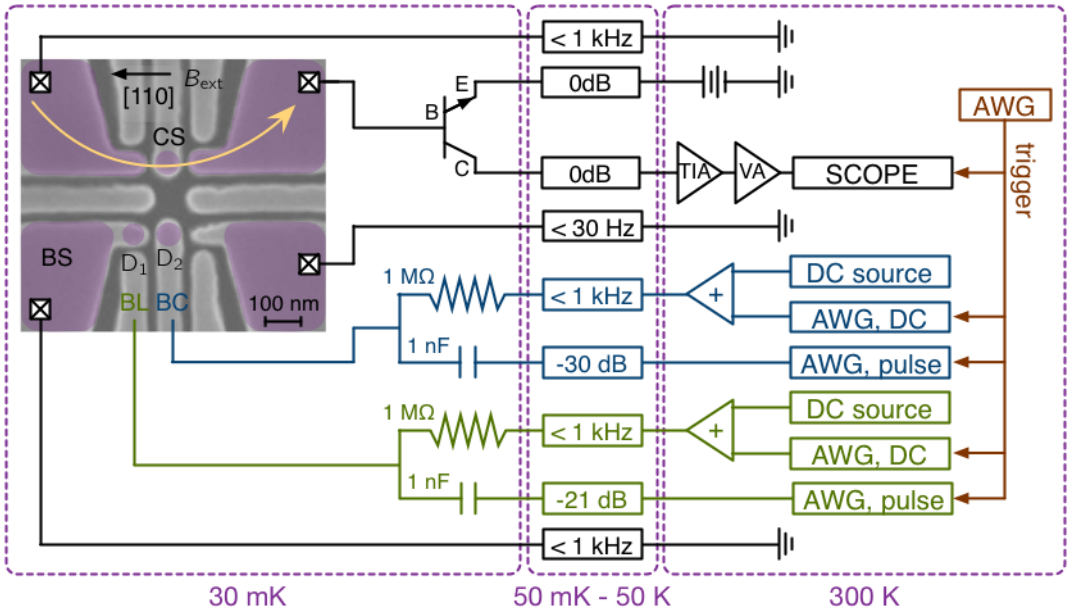

Figure 5.1: Schematic of the wiring and instruments relevant to pulsing and qubit control. The purple shading on the SEM image indicates the approximate position of the two-dimensional electron gas, the two quantum dots (D_1 and D_2), and the sensing dot (CS). The dashed purple boxes indicate the temperature of the different components.

5.1 Experimental setup and technical considerations

The experiments presented in the following chapter were performed in an Oxford Triton dry dilution refrigerator. Filtered DC lines as well as attenuated coax lines connect the sample, which is anchored to the cold finger at a temperature of 30 mK, to the breakout box situated at room temperature. Fig. 5.1 shows a scanning electron miscroscopy (SEM) image of a split-wire accumulation gate (SWAG) device similar to the one used, as well as the wiring and instruments relevant to the pulsing experiments. The device is tuned to form a double quantum dot (DQD) in the bottom wire, while the top wire is tuned to form a large dot that is used as a charge sensor (see Sec. 2.3.4). The drain of the charge sensor is connected to a current-biased silicon-germanium heterojunction bipolar transistor (CB-HBT) [119, 120]. This HBT is located on the printed circuit board used to mount the device and improves the signal-to-noise ratio by amplifying the charge-sensed signal before any noise is introduced at higher temperatures. The bottom left (BL) and bottom centre (BC) gates of the device are the ones used for pulsing. A superconducting magnet is used to

apply a uniform magnetic field in plane along the [110] crystallographic axis of the silicon substrate. The electron temperature was measured to be ~ 300 mK[1].

5.1.1 Pulse shaping

As stated in Sec. 2.3.5, DC lines must be filtered in order to achieve low electron temperatures. Because of this filtering, DC lines cannot be used to transmit the fast pulses needed to perform qubit control. However, the coax lines, which are attenuated in order to reduce sources of thermally induced noise (e.g. charge noise, Johnson voltage fluctuations from higher stages in the dilution refrigerator, etc.), are also not ideal for transmitting the control pulses to the device gates because of the large DC offsets of these pulses (usually between 2 V and 5 V for the SWAG devices). As an example, let's consider the case where a DC offset of $V_{\mathrm{BL}} = -4$ V must be maintained on gate BL while it is pulsed and the coax line leading to the gate is attenuated by 20 dB. This means that the waveform generator used must output a pulse with a DC offset of -40 V in order for the desired voltage to reach the device. Not only are there few arbitrary waveform generators (AWGs) capable of outputting such a large voltage while maintaining sufficient precision on the amplitude of the pulse, but the power dissipated through the attenuator would cause significant heating of the dilution refrigerator. To circumvent these problems, the gates chosen for pulsing are connected to bias tees located on the printed circuit board, as illustrated in Fig. 5.1. The DC bias is applied through the resistor, while the RF pulse is applied through the capacitor. The device gate, connected to the ouput of the bias tee, sees a combination of both signals.

While bias tees allow precision pulses with large DC offsets to be applied to the pulsing gates, they also introduce concerns regarding pulse shaping. Indeed, the bias tees used in this experiment, which are composed of a 1 MΩ resistor and a 1 nF capacitor, have an RC time constant of $\tau = R \cdot C = 1000$ µs. This means that any voltage applied to the RF path will decay as

$$V(t) = V_0 \, \mathrm{e}^{-t/\tau}, \tag{5.1}$$

[1]The electron temperature in this experimental setup was measured by Patrick Harvey-Collard using techniques similar to the ones described in Sec. 2.3.5.

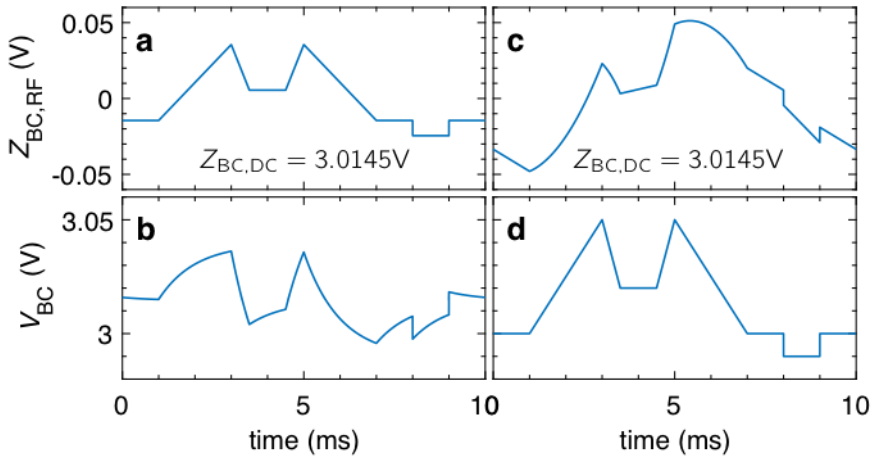

Figure 5.2: (a) Example of a voltage pulse applied by an AWG to the RF path of a bias tee with $\tau = 1000$ µs. A constant voltage of 3.0145 V is applied to the DC path. **(b)** Total voltage pulse from **(a)** as seen by the device at the output of the bias tee. **(c)** Compensated voltage pulse that must be applied by an AWG to the RF path of a bias tee with $\tau = 1000$ µs in order to achieve the effective pulse shown in **(d)** at the output of the bias tee.

where V_0 is the voltage applied at time $t = 0$. Any pulse applied to the RF path of the bias tee will therefore be deformed by the time it reaches the pulsing gate, as illustrated in Fig. 5.2(a-b). Consequently, if a specific voltage pulse $V(t)$ must be applied to a pulsing gate, the pulse applied by the AWG must be designed to compensate for this decay.

Shaping a voltage pulse to compensate for bias tee relaxation can be achieved in the following manner. First, the AWG sampling rate (λ) is chosen and the voltage pulse is discretized:

$$V(t) \mapsto \{V_0, V_1, ..., V_N\},$$

where V_n is the voltage at time $t_n = n \cdot \delta t$, and $\delta t = 1/\lambda$ is the time step between points. The sampling rate must be chosen such that $\delta t \ll \tau$. Next, the DC offset is calculated and subtracted from the pulse:

$$Z_{DC} = \frac{1}{N} \sum_n V_n$$
$$V_n' = V_n - Z_{DC}.$$

Z_{DC} corresponds to the constant voltage that must be applied to the DC path of the bias tee. Using Eq. (5.1), the decay in voltage $\delta V'_n$ caused by the bias tee that occurs during time δt between points n and $n+1$ can be calculated:

$$\begin{aligned} V'_n(\delta t) &= V'_n \, \mathrm{e}^{-\delta t/\tau} \\ &\approx V'_n \left(1 - \frac{\delta t}{\tau}\right) \\ \Rightarrow \delta V'_n &= V'_n(\delta t) - V'_n = -V'_n \left(\frac{\delta t}{\tau}\right). \end{aligned}$$

This means that, if we want the voltage seen by the device to change by $\Delta V'_n = V'_{n+1} - V'_n$ between times t_n and t_{n+1}, the voltage applied by the AWG between these times must change by:

$$\begin{aligned} \Delta Z_n = Z_{n+1} - Z_n &= \Delta V'_n - \delta V'_n \\ &= V'_{n+1} - V'_n + V'_n \left(\frac{\delta t}{\tau}\right). \\ \Rightarrow Z_{n+1} &= Z_n + V'_{n+1} - V'_n \left(1 - \frac{\delta t}{\tau}\right) \end{aligned} \tag{5.2}$$

Finally, Eq. (5.2) can be used to calculate all the Z_n voltage points of Z_{RF}, the pulse that must be applied to RF path of the bias tee in order to achieve the desired pulse $V(t)$. Fig. 5.2(c) shows a compensated voltage pulse calculated in this manner from the desired pulse shown in Fig. 5.2(d).

5.1.2 Increasing data acquisition speed

Being able to acquire data as rapidly as possible is desirable not only because it is preferable to acquire data faster than the slow drift that is usually observed in semiconducting devices, but also because fridge time is valuable and you never know when a power outage might befall, altering your device forever. Investing time to plan and implement efficient data acquisition protocols pays off rather quickly.

In a typical pulsing scan, a different pulse is applied at each point (and is usually repeated multiple times to acquire statistics). Pulse parameters, such as the duration or detuning of a certain segment of the pulse, are varied along the x and y axes of

the scan. This means that both the RF and DC components of the pulse may differ from point to point.

One possible way of acquiring a pulsing scan would be to load a single pulse to the AWGs connected to the RF lines, adjust the DC offsets of the gates, trigger the AWGs to play the waveforms while the scope acquires the data, and transfer the data from the scope to the computer before repeating all of these steps again for each of the remaining points in the scan. This method, however, requires communication between the computer and the instruments for every point in the scan, which significantly slows down the data acquisition process. In order to speed things up, communication with the instruments should be reduced as much as possible.

In the experiments presented in the following sections of this chapter, the RF pulses on BC and BL are applied by two synchronized channels on the same Keysight 33500B AWG. In order to reduce the number of communications between the computer and this AWG, as many pulses as possible are loaded to the instrument during each exchange. The number of pulses loaded at once is limited by the memory available on the waveform generator, the length of the pulses, and the chosen sampling rate. If the parameters of the scan are judiciously chosen, it is usually possible to simultaneously load all of the waveforms for a single line of the scan, if not the entire scan. Using the AWG in *sequence* mode means that an external trigger, rather than a prompt from the computer, can be used to indicate to the AWG that it should play the next waveform of the scan. The sequences used are constructed in the following manner: 1) Wait for trigger, 2) play waveform #1 N times, then wait for trigger, 3) play waveform #2 N times, then wait for trigger, and so on until all the waveforms loaded to the volatile memory of the instrument have been played.

In order to reduce the number of interactions between the computer and the instruments applying the DC offsets to the pulsing gates, AWGs can be used instead of DC voltages sources. In the following experiments, the DC biasses on BL and BC are applied by two channels on a second Keysight 33500B AWG. The desired offsets are loaded to the instrument in the form of short waveforms of constant voltage. To move between points in the pulsing scan, an external trigger is used in conjunction with the *sequence* mode of the instrument in the manner described above.

The Keysight DSO9054H oscilloscope used for acquiring the data is operated in *segmented* mode in a further attempt to reduce the number of communications involving the computer. When operated in segmented mode, time traces (i.e. seg-

ments) acquired by the scope are stored to its internal memory rather than sent immediately to the computer. The number of segments to be acquired as well as their time length must be communicated to the device ahead of time and an external trigger is used to indicate to the scope when it should begin recording a new segment. Once all the segments have been acquired, the data is sent to the computer in a single communication.

Finally, a third Keysight 33500B AWG is used not to apply voltages to the device, but to serve as an external trigger to all the other instruments mentioned above (as shown in red in Fig. 5.1). It is set up so that, once it receives a command from the computer to do so, it outputs a short square pulse at regular time intervals for a specified number of periods. In a sense, this AWG serves as a sort of conductor, indicating to all the other instruments when it is time to move on to the next point of the pulsing scan and ensuring that everything stays in perfect synchronization.

Using the method described above, the computer usually only needs to communicate with the instruments at the beginning and the end of each line of a pulsing scan. At the beginning of the line, the waveforms and sequences are loaded to the AWGs applying the RF pulses and DC offsets to the devices gates, the number and duration of the segments to be acquired are relayed to the oscilloscope, and the number and time between the trigger bursts is given to the third AWG. The computer then tells this AWG to start triggering the other instruments. Once sufficient time has elapsed for the data of the entire line to be acquired, the computer retrieves the data segments stored in the scope. This procedure is repeated for each of the remaining lines of the scan. A new pulsing code was developed following this method and was used to reduce data acquisition time by up to a factor of 18 compared with the previous point-by-point pulsing code.

An astute reader may have noticed that, in Fig. 5.1, the DC paths of both bias tees are connected to a DC voltage source in addition to an AWG. Though not strictly necessary, this is done because the Keysight 33500B has a tendency to jump to 0 V output whenever an error is encountered or if sufficient care is not taken when switching between waveforms. Such abrupt jumps in voltage on the device gates are undesirable and can lead to significant drift in qubit characteristics. In order to prevent these jumps and give the user peace of mind, a DC voltage source is used to output the larger part of the DC offset and is kept constant throughout the pulsing experiment. Using a voltage adder, the AWG is used to make small changes (on

the order of mVs) to the pulse's DC offset. Therefore, if a problem occurs during pulsing and the AWG suddenly outputs 0 V, the device will only experience a small jump in voltage and should be unaffected.

5.2 The singlet-triplet qubit Hamiltonian

In the experiments presented in this chapter, the system considered is a double quantum dot (DQD) tuned to the few-electron regime. Dot D_1 is situated beneath the BS gate, while dot D_2 is underneath BC, as shown in Fig. 5.1. The number of electrons in the DQD is denoted (N_1, N_2), where N_1 (N_2) is the number of electrons in D_1 (D_2). The DQD is coupled to a single reservoir situated beneath BS. When there are two electrons in the DQD, the spin state of the system can be expressed in the singlet-triplet (ST) basis :

$$\left.\begin{aligned} |S\rangle &= \frac{1}{\sqrt{2}}\left(|\uparrow\downarrow\rangle - |\uparrow\downarrow\rangle\right) \\ |T_0\rangle &= \frac{1}{\sqrt{2}}\left(|\uparrow\downarrow\rangle + |\uparrow\downarrow\rangle\right) \end{aligned}\right\} m = 0$$
$$|T_-\rangle = |\downarrow\downarrow\rangle \qquad m = -1$$
$$|T_+\rangle = |\uparrow\uparrow\rangle \qquad m = +1$$

where m indicates the projection of the total spin along the quantization axis. The $m = 0$ subspace, which is composed of S and T_0 and forms a decoherence-free subspace relative to fluctuations in the global magnetic field, is chosen as the computational basis for the qubit [45]. The Hamiltonian of the two-electron DQD system, expressed in the $\{|(2,0)S\rangle, |(2,0)T_0\rangle, |(1,1)S\rangle, |(1,1)T_0\rangle\}$ basis is [56, 91]:

$$\hat{H}(t) = \frac{1}{2}\begin{pmatrix} \varepsilon(t) & 0 & -t_S & 0 \\ 0 & 2J_{(2,0)} + \varepsilon(t) & 0 & -t_T \\ -t_S{}^* & 0 & -\varepsilon(t) & -\Delta E_Z \\ 0 & -t_T{}^* & -\Delta E_Z{}^* & 2J_{(1,1)} - \varepsilon(t) \end{pmatrix}. \tag{5.3}$$

In the equation above, $\varepsilon = E_{(1,1)} - E_{(2,0)}$ is the detuning, i.e. the difference in energy between the $(1,1)$ and $(2,0)$ states of the DQD, $J = E_{T_0} - E_S$ is the exchange

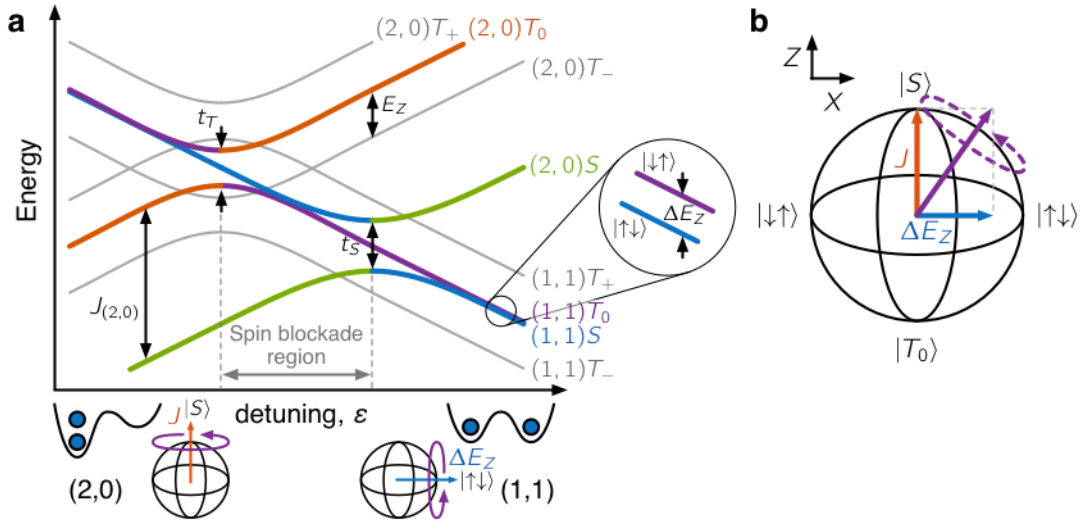

Figure 5.3: (a) Energy level diagram showing the eigenenergies of the ST qubit. The states belonging to the $m = 0$ subspace used to encode the qubit are drawn in colour, while the states that are neglected are shown in grey. **(b)** Bloch sphere representation of the ST qubit and its relevant driving energies.

interaction arising from the overlap of the electron wave functions, t_S is the tunnel coupling between $(1,1)S$ and $(2,0)S$, and t_T is the tunnel coupling between $(1,1)T_0$ and $(2,0)T_0$. Finally, ΔE_Z is the difference in the Zeeman energy between the two dots along the quantization axis. This difference in energy arises from spin-orbit effects and will be discussed in more detail in Sec. 5.2.1. The detuning can be controlled electrostatically through the voltages applied to gates BL and BC, and $\varepsilon = 0$ is chosen to correspond with the (2,0)-(1,1) charge transition. The energy of the four eigenstates of the Hamiltonian presented in Eq. (5.3) are plotted in Fig. 5.3(a). By applying an external magnetic field, B_{ext}, the energies of the $T_\pm$ states are shifted by the Zeeman energy $E_Z = \pm g\mu_B B_{\text{ext}}$, lifting the degeneracy between the three triplet states. The energies of the $T_\pm$ states are shown in grey in Fig. 5.3(a).

A convenient way of visualizing the ST qubit is with the help of a Bloch sphere, as shown in Fig. 5.3(b). The S and T_0 states lie at the poles, along the Z axis, while the $|\uparrow\downarrow\rangle$ and $|\downarrow\uparrow\rangle$ states lie on the equator, along the X axis. At large negative detuning, the two electrons occupy the same dot and the exchange, $J_{(2,0)}$, dominates. In this regime, S and T_0 are the eigenstates of the system and J drives rotations around the Z axis of the Bloch sphere, between $|\uparrow\downarrow\rangle$ and $|\downarrow\uparrow\rangle$. On the other hand, at large positive detuning, the two electrons occupy different dots and the exchange energy

is small ($J_{(1,1)} \approx 0$). In this regime, $|\uparrow\downarrow\rangle$ and $|\downarrow\uparrow\rangle$ are the eigenstates of the system and ΔE_Z drives rotations around the X axis of the Bloch sphere, between $|S\rangle$ and $|T_0\rangle$.

5.2.1 Effect of spin-orbit coupling

From Schrödinger's equation, we know that the time evolution of a spin 1/2 with initial state $|\psi(0)\rangle = \alpha\,|\downarrow\rangle + \beta\,|\uparrow\rangle$ in the presence of an external magnetic field, B, is given by:

$$\begin{aligned} |\psi(t)\rangle &= \alpha\, e^{-iE_\downarrow t/\hbar}\,|\downarrow\rangle + \beta\, e^{-iE_\uparrow t/\hbar}\,|\uparrow\rangle \\ &= \alpha\, e^{+i\omega t/2}\,|\downarrow\rangle + \beta\, e^{-i\omega t/2}\,|\uparrow\rangle\,, \end{aligned} \tag{5.4}$$

where $E_{\uparrow(\downarrow)} = (-)\frac{1}{2} g \mu_B B = (-)\hbar\omega/2$ is the energy of the spin when it is in the state $|\uparrow\rangle$ ($|\downarrow\rangle$). In this equation, μ_B is the Bohr magneton, $g = 2$ is the electron g-factor in silicon, and ω is the Larmor precession frequency of the spin.

Though spin-orbit effects are small in bulk silicon, recent work has shown that the strong confinement of the electron wave functions at the Si/SiO_2 interface can lead to a difference in the effective electron g-factors, $\Delta g = g_2 - g_1$, between the two QDs [59, 60]. This results in different Zeeman energies for each dot and means that the frequency of a spin's Larmor precession will depend on its position in the DQD. Using Eq. (5.4), we find that the time evolution of the singlet state in the (1,1) charge stability region is:

$$\begin{aligned} |\psi(0)\rangle &= \frac{1}{\sqrt{2}}\left(|\uparrow\downarrow\rangle - |\downarrow\uparrow\rangle\right) \\ \Rightarrow |\psi(t)\rangle &= \frac{1}{\sqrt{2}}\left(e^{-i\omega_1 t/2}\, e^{+i\omega_2 t/2}\,|\uparrow\downarrow\rangle - e^{+i\omega_1 t/2}\, e^{-i\omega_2 t/2}\,|\downarrow\uparrow\rangle\right) \\ &= \frac{1}{\sqrt{2}}\, e^{+i(\omega_2-\omega_1)t/2}\left(|\uparrow\downarrow\rangle - e^{-i(\omega_2-\omega_1)t}\,|\downarrow\uparrow\rangle\right)\,, \end{aligned} \tag{5.5}$$

where $\omega_i = g_i \mu_B B_{ext}/\hbar$ is the Larmor precession frequency of the electron in D_i. The factor $e^{+i(\omega_2-\omega_1)t/2}$ is a global phase and, therefore, will have no effect on the outcome of a measurement performed on the system. From Eq. (5.5), it is clear that a system that is in the $(1,1)S$ state at time $t = 0$ will oscillate between the S and T_0 states at a frequency of $2\pi f = \Delta\omega = \omega_2 - \omega_1 = \Delta g \mu_B B_{ext}/\hbar$. This corresponds to

rotations about the X axis of the Bloch sphere. The energy driving these rotations is

$$\Delta E_Z = E_{Z,2} - E_{Z,1} = \hbar\Delta\omega = \Delta g \mu_B B_{\text{ext}}\,, \tag{5.6}$$

the difference in Zeeman energy between the two QDs. This situation is analogous to one where rotations arise from the difference in Zeeman energy caused by a difference in the local magnetic field between two QDs. Because of this, the difference in SO-coupling between the dots can be likened to a magnetic field gradient.

A distinction worth noting between the ΔE_Z obtained here and one resulting from a magnetic field gradient is that it is achieved without the need of external components, such as micromagnets or transmission line resonators, that can complicate device fabrication. Additionally, the strength of ΔE_Z can be tuned by adjusting the strength of the external magnetic field, as is evident in Eq. (5.6). In the experiments presented in the following chapter, B_{ext} is applied along the [110] crystallographic axis of the Si substrate in order to maximize Δg [59].

5.3 Pulsing basics

Once a working device has been identified and cooled down in a dilution refrigerator, charge sensing has been established, the DQD has been formed and tuned to the few electron regime, and the dot-lead tunnel rate has been adjusted to a reasonable value (using techniques described in Chapter 2), it is finally time to perform pulsing experiments on the qubit. In order to facilitate their construction, the pulses are broken down into "steps". Each step serves a different purpose and is composed of a ramp to a specified point in the charge stability diagram followed by time spent idling at that point. The following section goes over the usual steps composing the pulses used to perform the experiments presented in the remainder of this thesis.

Fig. 5.4(a) shows a charge stability diagram tuned to the (2,0)-(1,1) anticrossing. The BL and BC gates are the ones wired in such a way as to apply RF pulses to the device, as described in Sec. 5.1. The position of the eight usual pulsing steps are indicated by red dots. These steps are:

(I) ***Initialize*** is used to reset the system in the (1,0) charge region in order to begin each pulse in a well known state. The I point is placed near the L point in order to avoid any unexpected trajectories while ramping between these points.

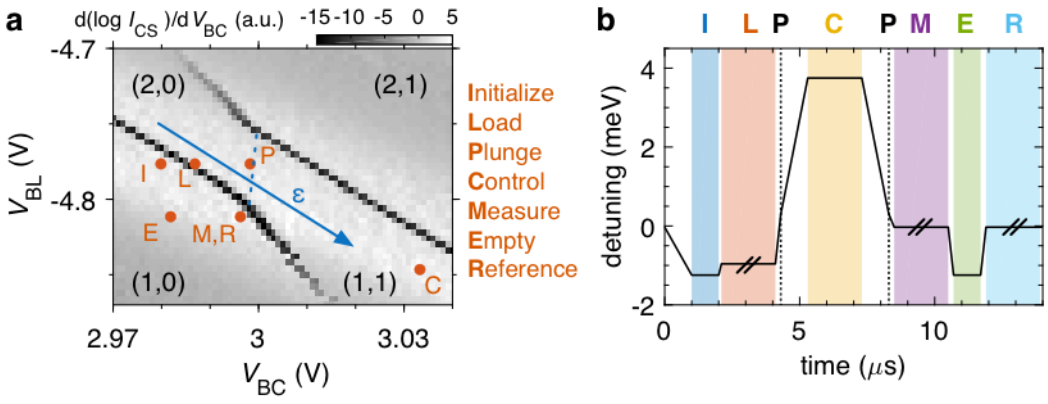

Figure 5.4: (a) Charge stability diagram of a double QD tuned to the (2,0)-(1,1) charge transition. The dashed blue line corresponds to the zero detuning line and the arrow indicates the direction of increasing detuning between the dots. The red dots indicate the position of the steps for a typical pulse sequence. **(b)** Example of a pulse used to control the ST qubit. The plateaus corresponding to the different steps of the pulse are labelled above the graph. The *Load* (L), *Measure* (M), and *Reference* (R) times have been shortened for clarity.

(L) ***Load*** is located in the (2,0) charge stability region near the (1,0)-(2,0) charge transition line. This step is used to load the second electron onto the DQD. Adjusting the position of this point determines whether the second electron is loaded into a singlet or triplet state, as explained in Sec. 5.4.

(P) ***Plunge*** is located near the (2,0)-(1,1) charge transition. Like *I*, it is used to ensure that the pulse is well behaved as it transitions into the *C* step.

(C) ***Control*** is the step that is used to perform qubit operations. Adjusting the ramp times to and from this step determines whether the spin and charge are transferred diabatically or adiabatically into (1,1), as discussed in Sec. 5.5. The position and length of time spent idling at this point affect the operation performed on the qubit. Alternatively, rather than idling at a fixed detuning point, the position of *C* can be pulsed in order to achieve more elaborate qubit operations, as in Sec. 5.7.2 and Sec. 5.8.

(P) ***Plunge*** serves the same purpose as the previous *P* point. It is important that this *Plunge* step be situated between the *S* and T_0 avoided crossings in order for latched readout, described in Sec. 5.4, to work properly [67].

(M) ***Measure*** is situated in the (1,0) charge stability region and is used to measure the spin state of the qubit through spin to charge conversion. The position

and duration of this point must be carefully calibrated in order for readout to function properly (see Sec. 5.4).

(E) ***Empty*** is located in the (1,0) charge region near the *M* point and is used to ensure that the second electron has been emptied from the DQD.

(R) ***Reference*** is located at the same point as *M* and is used to determine what the charge-sensed signal would have been had a singlet been measured. This value is used to adjust the measurement signal acquired during the *M* step in order to compensate for slow drift in the charge-sensed signal.

As mentioned previously, each step of the pulse is composed of a voltage ramp (from the voltage point of the previous step to the voltage point of the current step) followed by a plateau at fixed voltage. The only exception to this is the *Control* step, where RF pulses may be applied to the position of *C* in lieu of a plateau at constant voltage. Depending on the measurement being performed, some of these pulse steps may be omitted or more may be added. The ramp times and wait times used for typical pulses are listed in Tab. 5.1. A pulse constructed with the listed pulse steps and ramp/wait times is shown in Fig. 5.4(b). It is important to note that, in Fig. 5.4(b) as well as in all pulses shown in the remainder of this thesis, it is the pulse as seen by the device that is drawn, not the compensated voltage pulses output by the the control instruments (see Sec. 5.1.1).

Table 5.1: Typical time scales used for pulsing. The ramp time indicates the time spent sweeping the voltage on the pulsing gates to go from the previous pulse point to the desired voltage for the pulse step in question. The wait time indicates the time spent idling once the desired voltage point has been reached.

Pulse step	ramp time (μs)	wait time (μs)
Initialize	1	1
Load	0	20
Plunge	0.2	0
Control	*variable*	*variable*
Plunge	*variable*	0
Measure	0.2	50
Empty	0.2	1
Reference	0.2	50

5.4 Latched readout

Before attempting to perform coherent operations on the state of any spin qubit, it is important to first have the means of reading said state. One method commonly used to perform readout on ST qubits relies on Pauli spin blockade (PSB) [64]. With this method, the measurement point is placed near the (1,1)-(2,0) charge transition, in the spin blockade region indicated in Fig. 5.3(a). In this region, it is energetically favourable for singlets to occupy the (2,0) charge state, while the preferred state for triplets remains (1,1). Therefore, the spin state of the system can be read by using the charge sensor to measure the charge configuration of the DQD.

An obvious drawback of the PSB readout described above is that the charge sensor must be sensitive enough to tell the difference between the (1,1) and (2,0) charge configurations, both of which contain two electrons. The signal can be optimized by orienting the DQD dipole towards the charge sensor so that changing the charge configuration results in moving an electron slightly closer to, or further from, the charge sensor. This, however, adds a significant constraint to the device layout and may, in cases such as donor-dot qubits [53, 54], be out of the user's control. From the relative position of the DQD and the charge sensor shown in Fig. 5.1, PSB is expected to lead to a very small signal in these experiments. Indeed, this is confirmed by the absence of a visible interdot transition line in the stability diagram shown in Fig. 5.4(a). An alternate readout scheme is therefore needed in order to measure the spin state in this system.

The readout method used in the following experiments relies on the fact that the DQD is only connected to one lead which is tunnel coupled to D_1, as shown in Fig. 5.1. The absence of a second reservoir connected to D_2 leads to hysteresis, also referred to as charge latching, in the system [121]. This hysteretic behaviour is clearly exhibited in Fig. 5.5, where it is shown that the sweep direction of V_{BC} chosen when measuring a charge stability diagram affects the position of the D_2 charge transition lines. When V_{BC} is lowered and the system is swept over the (1,1)-(1,0) charge transition line (blue dot in Fig. 5.5(a)), the electron in D_2 cannot be emptied because it is not directly tunnel coupled to the lead. Nor can it tunnel through D_1 because the (2,0) charge state is inaccessible. The system will therefore remain in the (1,1) charge state until it relaxes through processes involving metastable states [67] or until V_{BC} reaches the extension of the interdot transition line and the (2,0) charge

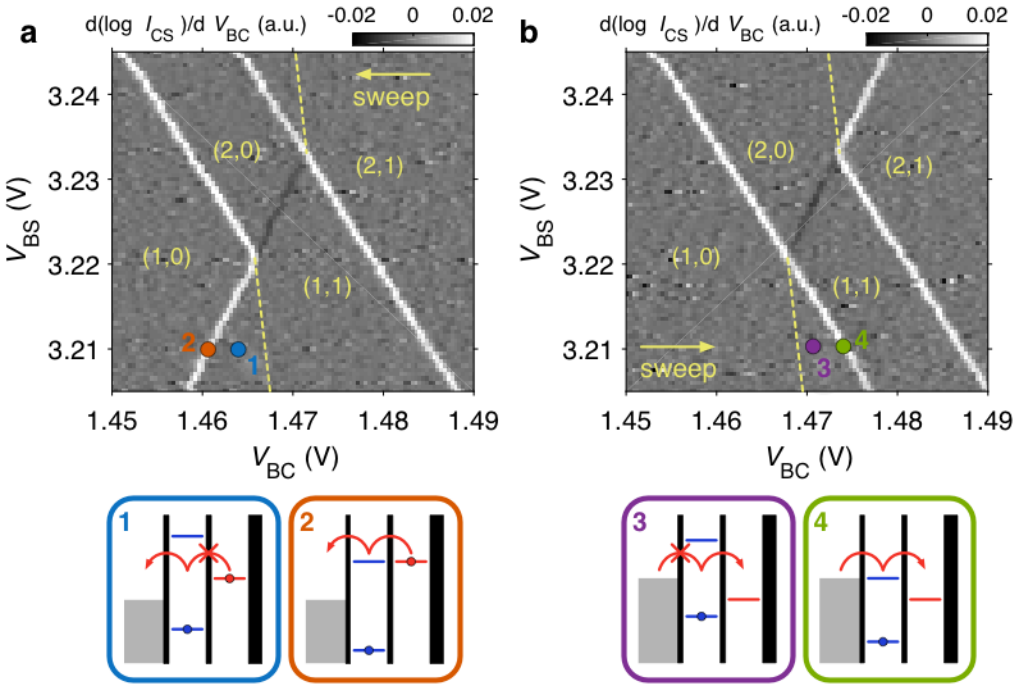

Figure 5.5: Charge stability diagrams taken by sweeping V_{BC} towards the left **(a)** and towards the right **(b)**. The dashed yellow lines indicate where the transition lines of the right dot would be if there weren't any latching.

state becomes accessible (red dot in Fig. 5.5(a)). This causes the D_2 transition line to appear as an extension of the interdot transition line. A similar phenomenon occurs when V_{BC} is raised and swept over the (1,0)-(1,1) charge transition (purple dot in Fig. 5.5(b)). In this case, no electron will be able to tunnel onto D_2 until V_{BC} has reached the extension of the (1,0)-(2,0) transition line (green dot in Fig. 5.5(b)), and the D_2 transition line will appear as an extension of that of D_1.

Turning the electron latching described above into readout of the ST qubit is done following the method described in Harvey-Collard *et al.* [67]. After having performed any desired qubit operations at the control point C of the pulse (see Fig. 5.4(C)), the system is moved to the P point located in the PSB region. The $(1,1)S$ state becomes $(2,0)S$, while the $(1,1)T_0$ state remains in the (1,1) charge configuration, as in conventional PSB readout. The system is then ramped to point M, which is situated in the (1,0) charge stability region, in the extension of the PSB region. Once at point M, the $(2,0)S$ state is free to tunnel to $(1,0)$, while the $(1,1)T_0$ state will experience latching and remain unchanged. The difference in signal that must

be measured by the charge sensor in order to differentiate between a singlet and a triplet is now of one full electron charge and does not depend on the orientation of the DQD dipole relative to the sensor. This readout method is referred to as enhanced latching readout (ELR).

The method followed to choose the measurement point for ELR is shown in Fig. 5.6. The first step is to identify the extension of the PSB area in the (1,0) charge stability region. This is done by placing the L point sufficiently deep in (2,0) to load a mixture of singlets and triplets, and then transferring the triplets to (1,1) by ramping to point P in the PSB region. The measurement point is then swept in the area of interest, indicated by a red rectangle in Fig. 5.6(a). The charge-sensed signal as a function of the position of point M is shown in Fig. 5.6(b), where the extension of the PSB region is highlighted by dashed white lines. Next, the charge-sensed signal is measured while sweeping the L and M points across the (1,0)-(2,0) charge transition line and the latching readout region, respectively, as shown in Fig. 5.6(c). When L is sufficiently close to the D_1 transition line, the (2,0)T states are inaccessible and only singlets are loaded, allowing the qubit to be prepared in the $|S\rangle$ state. This loading window is obvious by the absence of triplet signal in the measurement window, as highlighted by the white dashed lines in Fig. 5.6(c).

Once the L and M points have been chosen, the last step in the readout tuning process is to calibrate the conversion of charge-sensed signal to triplet probability. This is done by fitting a Fermi-Dirac distribution to a line trace of the charge-sensed signal as M is swept across the measurement window, as shown in Fig. 5.6(d). The equation used for the fit is

$$I_{CS}(V_{BC}) = \frac{A}{\exp((V_{BC} - V_0)/d) + 1} + m \cdot V_{BC} + b,$$

where A is the amplitude of the step function, V_0 is its position, and d is its width. b and m describe the offset and slope of the charge-sensed signal, which is tuned to be in a linear region on the edge of a Coulomb blockade peak. Here, A corresponds to the difference in signal between 100% singlets ($P(T) = 0$) and 100% triplets ($P(T) = 1$). This fit, however, is not used to extract the the offset of the charge-sensed signal corresponding to 100% singlets because this value tends to drift slowly over time. In order to limit the effect of this drift on the calculated triplet probability, the *Empty* and *Reference* points are added to the pulse, as described in Sec. 5.3. The E

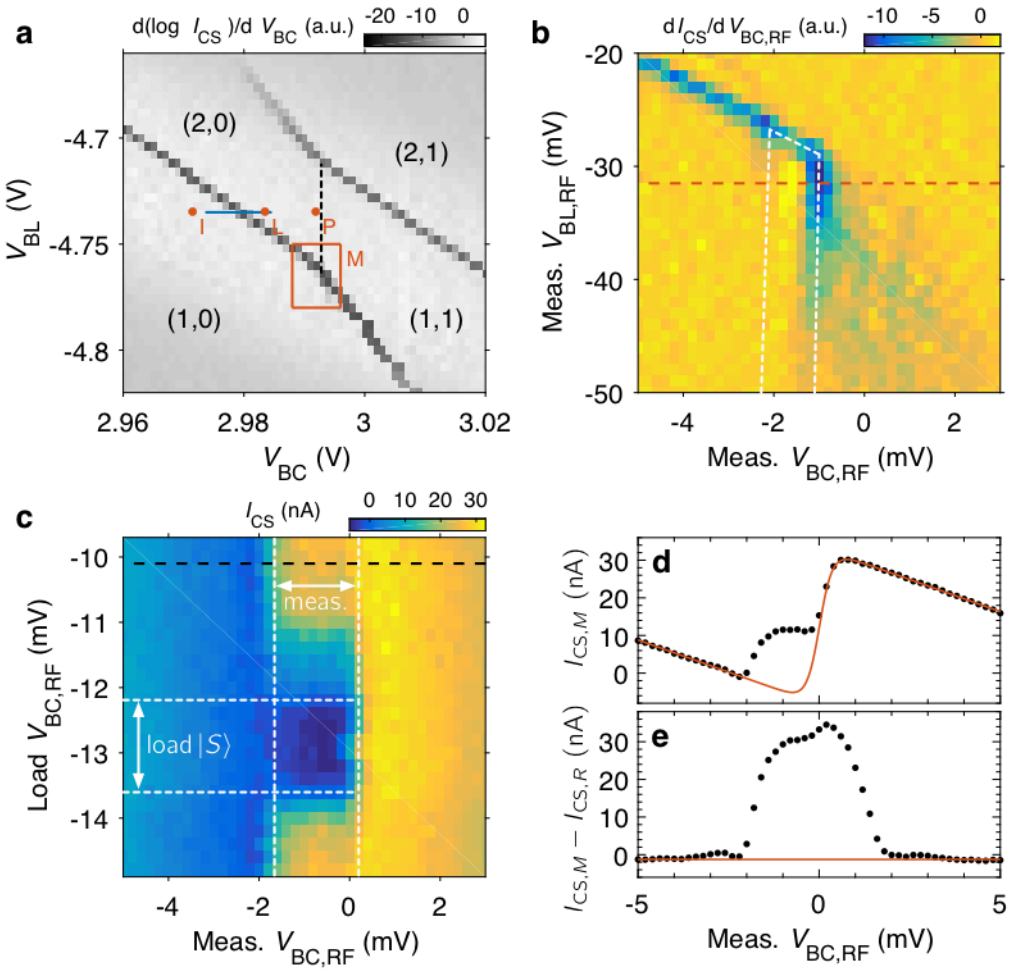

Figure 5.6: (a) Charge stability diagram of a double QD tuned to the (2,0)-(1,1) charge transition. The *Initialize* (I), *Load* (L) and *Plunge* (P) points of the pulse are indicated by red dots. The dashed black line highlights the interdot transition. **(b)** Latching readout region (highlighted by dashed white lines) measured by moving the *Measure* (M) point of the pulse to different voltages inside the red rectangle drawn in **(a)**. **(c)** Mapping of the load and measure windows achieved by sweeping V_{BC} of the loading point across the blue line in **(a)** and V_{BC} of the measurement point along the red dashed line in **(b)**. **(d)** Charge-sensed signal measured across the dashed black line in **(c)**. The red line is a fit to the data to extract the amplitude of the readout signal. **(e)** Referenced signal measured across the dashed red line in **(c)**. The red line is a fit to the data to extract the offset of the readout signal. See the main text for more details. The applied external magnetic field is 1.2 T.

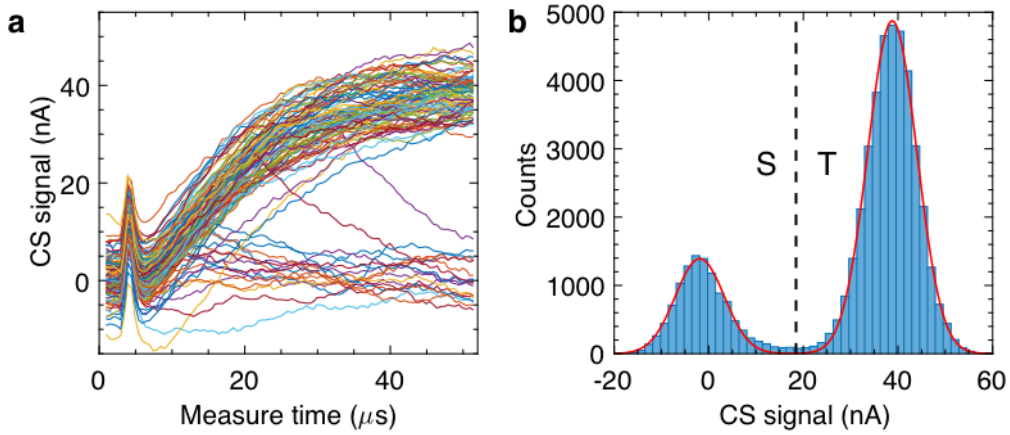

Figure 5.7: (a) Charge sensor signal during the 50 µs-long *Measure* portion of the pulse, after a mixture of S and T has been loaded. A reference current of 451 nA was subtracted from the data. 100 traces are shown. **(b)** Histogram of the average signal during the last 10 µs of measurement window (50000 data points in total). The red line is a double-Gaussian fit to the data. The black dashed line is mid-way between the two peaks and corresponds to the chosen ST threshold. The applied external magnetic field is 1.2 T.

step ensures that the DQD occupancy is (1,0), and the R step measures the signal of this charge state at the same point as M, which corresponds to the signal that would have been measured for a singlet. In order to account for any possible hysteresis or memory in the charge sensor, the average referenced signal ($I_{CS,R} - I_{CS,M}$) is measured by sweeping the position of both M and R across the measurement window allowing the global offset C to be measured, as shown in Fig. 5.6(e). Finally, the CS signal can be converted to triplet probability in the following manner:

$$P(T) = \frac{I_{CS,R} - I_{CS,M}}{A} + C.$$

5.4.1 Single-shot spin readout

In the experiments presented in this chapter, the use of a current-biased silicon-germanium heterojunction bipolar transistor (CB-HBT) [120] leads to a large enough signal-to-noise ratio for single-shot readout of the qubit to be performed. Fig. 5.7(a) shows 100 single-shot time traces of the current through the charge sensor taken during the 50 µs-long M step of a pulse where the qubit was initialized in a random state and immediately measured. An average reference current of 451 nA is

subtracted from the data. It is clear from this data that, after a response time of ~ 30 µs, the individual traces are split into two clusters. Indeed, when the average current during the last 10 µs of 50000 such traces is plotted in histogram from, as in Fig. 5.7(b), two distinct peaks are observed. The low current peak corresponds to singlets, while the high current peak corresponds to triplets. To determine whether a single trace will be labeled as S or T, a simple thresholding method similar to the one described in Eng *et al.* [122] is used. A double Gaussian function is fit to the current distribution of the single shot traces, and the midpoint between the two peaks is chosen as the ST threshold. If the charge sensor's current during the last 10 µs of the M step is above (below) this threshold, the shot in question will be counted as a triplet (singlet). Calculating the triplet probability in this case is straightforward: it is simply the number of triplet counts divided by the total number of shots measured.

It is important to note that, with the method described above, any triplet that decays during the first 40 µs of the measurement window will be counted as a singlet. Making the measurement window shorter will result in fewer triplet decays, but if it is too short compared to the rise time of the CB-HBT, the separation between the S and T current distributions will be reduced, causing a larger overlap between between them and increasing the probability of mislabelling the outcome of a shot. A rigorous optimization of the readout process is, however, not the focus of this work and the chosen method leads to results that are more than satisfactory. In order to improve the readout fidelity in future experiments, one might consider thresholding based on a peak-signal filter rather than a boxcar filter as is done in this work [123].

5.5 RAP/SAP measurement

Once qubit initialization and readout has been established, it is important to characterize how the ramping speed through the charge anticrossing affects the qubit. In order to do this, the qubit is initialized in the $(2,0)S$ state and the triplet probability is measured as a function of the wait time, t_{wait}, at a *Control* point situated at deep detuning. The ramp time, t_{ramp}, to and from this point is also varied, as shown in Fig. 5.8.

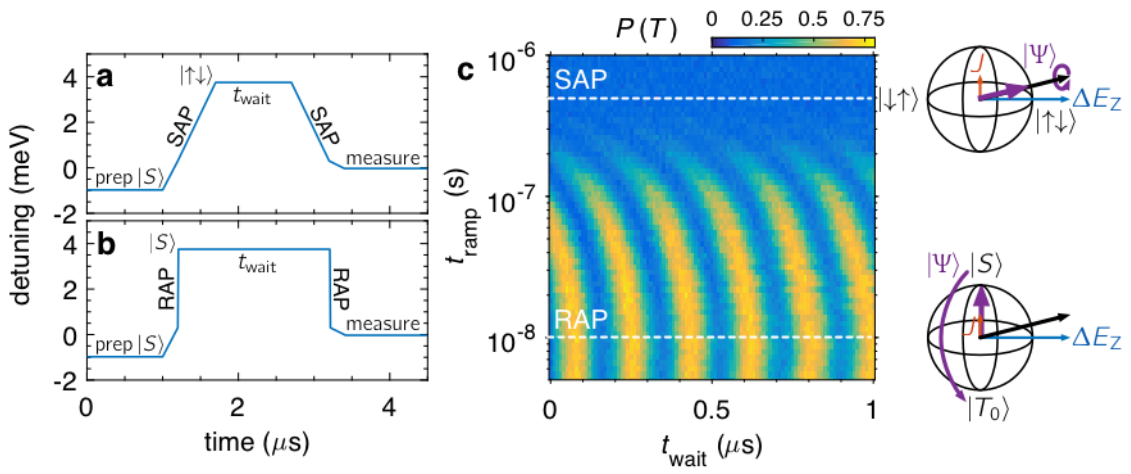

Figure 5.8: Pulse sequences resulting in **(a)** slow and **(b)** rapid adiabatic passage between the (2,0) and (1,1) charge states. **(c)** Triplet return probability as a function of the the wait time (t_{wait}) and the ramp time (t_{ramp}) to/from a *Control* pulse point situated at $\varepsilon = 3.75$ meV. The applied external magnetic field is 1.1 T. Ramp times resulting in slow and rapid adiabatic passage are indicated by white dashed lines.

If the ramp through the anticrossing is very slow, the qubit will remain in the ground state of the system throughout the ramp and will be in $|\uparrow\downarrow\rangle$, the ground state of (1,1), once it reaches point *C*. If the ramp back to *P* is equally slow, the system will be transferred back to $(2,0)S$, resulting in a low triplet signal during measurement. This is indeed what is observed in Fig. 5.8(c) for $t_{ramp} > 400$ ns. If the system were in $|\downarrow\uparrow\rangle$, the excited state of (1,1), the slow ramp to (2,0) would result in $(2,0)T_0$. This charge transfer method is referred to as slow adiabatic passage (SAP) because the ramp is slow with respect to both the charge and the spin of the system [56].

If the ramp time to and from *C* is made sufficiently short, the spin state will not evolve during the ramp and the $(2,0)S$ state will become $(1,1)S$. Because *S* is not an eigenstate in the (1,1) region, the system will begin to rotate around the *X* axis of the Bloch sphere, as described in Sec. 5.2.1. A fast ramp back to the PSB region will result in $(1,1)S$ becoming $(2,0)S$, and $(1,1)T_0$ remaining unchanged.[2] The varying wait time at *C* results in oscillations of the triplet probability measured at the end of the pulse, as seen in Fig. 5.8(c) for $t_{ramp} < 30$ ns. This charge transfer method is called rapid adiabatic passage (RAP) because the ramp is adiabatic with respect to charge, but not with respect to spin.

[2] If the ramp out of the (1,1) region were to go past the *T* avoided crossing rather than stopping in the PSB region, $(1,1)T_0$ would become $(2,0)T_0$.

If the ramp time through the charge anticrossing is between the RAP and SAP regimes, the spin state will be transferred adiabatically with a certain Landau-Zener probability, P_{LZ} [124, 125]. In this case, only the $1 - P_{\mathrm{LZ}}$ portion of the spins that were transferred through RAP will result in ST rotations, resulting in a reduction in the visibility of the rotations. This effect can be seen in Fig. 5.8(c) for t_{ramp} between 30 ns and 400 ns. The frequency of the rotations, however, remains unchanged. The slight curvature of the striations at larger t_{ramp} is due to the ramp time becoming long enough for the spin rotation occurring during the ramp to become noticeable.

It is important to note that, in the case of the pulsing code used in this work, it is the ramp time that is specified when building a pulse. However, it is the ramp rate (μeV/s) that is relevant when determining the slow and rapid adiabatic passage regimes. The ramp times resulting in RAP and SAP are therefore dependent on the position of point C. In the experiment presented in Fig. 5.8, C is placed at $\varepsilon = 3.75$ meV and the resulting SAP and RAP times are 500 µs and 10 ns, respectively. If C is moved to smaller detuning, shorter ramp times may be needed to achieve RAP.

5.6 Spin funnel measurement

It is not unlikely that, despite having successfully tuned qubit initialization and readout (as described in Sec. 5.4), no qubit rotations are observed in the RAP/SAP measurement (detailed in Sec. 5.5). One potential cause may be a tunnel coupling between the dots that is far smaller than the ideal range of values (which is a few tens of μeV for these experiments). If this is the case, it is useful to have a way of confirming that the tunnel coupling is to blame before undertaking the task of tuning the device to a new regime. Thankfully, the spin funnel measurement can be used to measure the tunnel coupling over an extremely wide range of values and doesn't rely on coherent rotations to do so [20, 126].

The idea behind the spin-funnel measurement is quite simple. After being initialized in the $(1,1)S$ state, the system is quickly ramped to a specified detuning point, C. After being left at C for a fixed time t_{wait}, the system is quickly ramped back to the PSB region and read out using ELR. The idea is that, if C is situated exactly at the S-T_- anticrossing, incoherent mixing between the S and T_- states will occur, causing an increased triplet signal during readout. If C is not at this degeneracy point, no triplets will be generated. Measuring the position of the anticrossing as

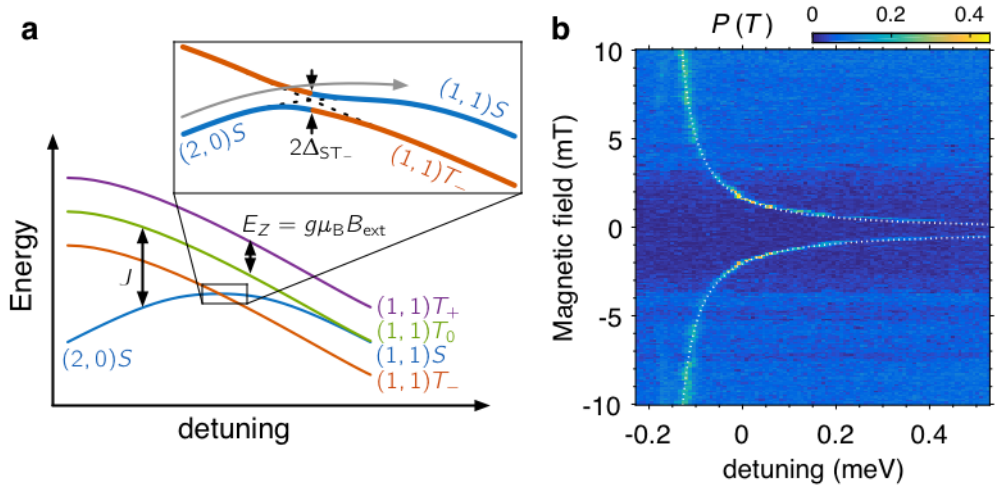

Figure 5.9: (a) Energy level diagram for the ST qubit in the presence of an external magnetic field B. The inset shows the S-T_- anticrossing. **(b)** Spin funnel measurement showing triplet probability as a function of the detuning of the *Control* portion of the pulse and the strength of the external magnetic field. The white dotted line is a fit to the data.

a function of the applied external magnetic field, B_{ext}, results in the funnel-shaped feature shown in Fig. 5.9. Because the S-T_- degeneracy occurs at $J(\varepsilon) = g\mu_B B_{\text{ext}}$, a fit to the spin funnel allows the extraction of various parameters, including the tunnel coupling.

The exchange interaction is, by definition, the energy difference between the lower branch of singlets and the lower branch of T_0 triplets, E_S and E_T, respectively (see Sec. 5.3). These energies are given by:

$$E_S(\varepsilon) = -\frac{1}{2}\sqrt{\varepsilon^2 + {t_S}^2}\,,$$
$$E_T(\varepsilon) = \frac{1}{2}\left(J_{(2,0)} - \sqrt{\left(\varepsilon + J_{(2,0)}\right)^2 + {t_T}^2}\right),$$

where $J_{(2,0)}$ is the exchange interaction between the two spins in the (2,0) charge configuration, and t_S (t_T) is the tunnel coupling between the singlet (triplet) states. It is assumed that $J_{(1,1)} = 0$ when the spins are well separated in different dots.

Table 5.2: Parameters extracted from a fit to the spin funnel measurement.

Parameter	energy (μeV)
t_S	12.88
t_T	8.971
ε_0	-161.5
c	-0.0223

Using these expressions, the equation used to fit the exchange energy is obtained:

$$J(\varepsilon) = \frac{1}{2}\left(J_{(2,0)} - \sqrt{\left(\varepsilon - \varepsilon_0 + J_{(2,0)}\right)^2 + {t_T}^2} + \sqrt{(\varepsilon - \varepsilon_0)^2 + {t_S}^2}\right) + c\,. \tag{5.7}$$

Here, ε_0 is used to account for the fact that the zero detuning point has not been finely tuned and may need adjusting. An offset, c, has been added to correct for any hysteresis in the magnetic field applied by the superconducting magnet. $J_{(2,0)} = 330\ \mu$eV is extracted from a magnetospectroscopy scan (Sec. 2.3.6), while t_S, t_T, ε_0, and c are kept as fit parameters. The values of these parameters extracted from a fit to the spin funnel measurement (dotted white line in Fig. 5.9(b)) are listed in Tab. 5.2.

5.7 Two-axis DC-controlled gates

In order to achieve universal quantum control of a qubit, one must be able to perform rotations around at least two non-collinear axes of the Bloch sphere [45, 127]. With the ST qubit used here, there are different ways to achieve this. The first, detailed in the following section, is by performing "DC-controlled" gates. These gates are referred to as DC because the detuning is held constant during the *Control* step of the pulse. The two axes of rotation are determined by the position of C.

5.7.1 Spin-orbit-driven gates

The first DC-controlled gate is driven by spin-orbit coupling (Sec. 5.2.1). In order to observe these rotations, the qubit is initialized in the $(2,0)S$ state, then transferred to $(1,1)S$ through RAP to point C at deep detuning (see Sec. 5.5). As described in

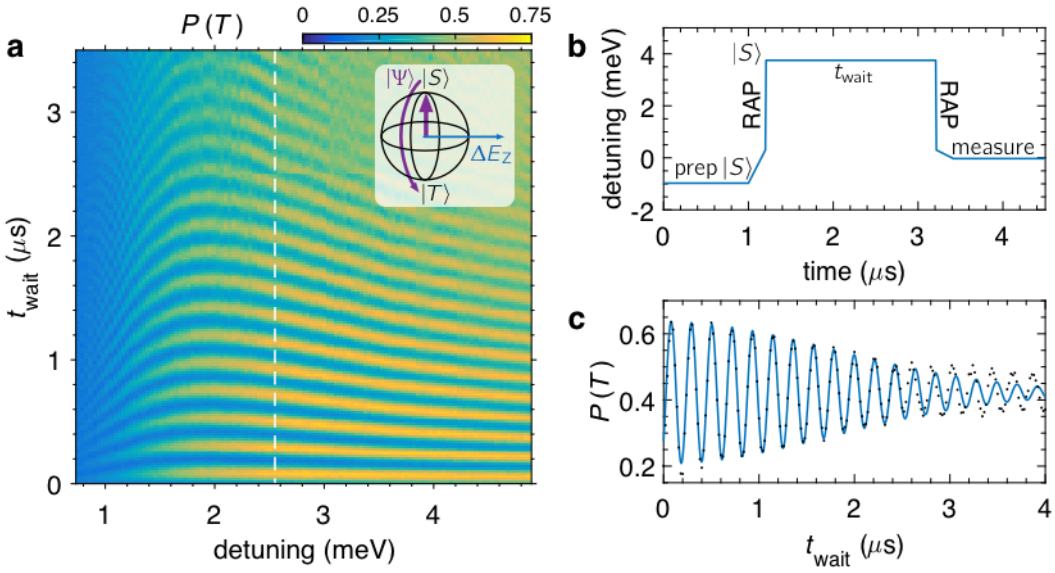

Figure 5.10: (a) Triplet return probability as a function of the duration and operating point of the pulse sequence shown in **(b)**. **(c)** Line cut taken along the dashed white line in **(a)** showing decaying oscillations of the triplet probability. The solid line corresponds to a fit to the data. The applied external magnetic field is 1.1 T.

Sec. 5.2.1, this will lead to rotations between the $(1,1)S$ and $(1,1)T_0$ states, around the X axis of the Bloch sphere. After letting the system evolve for a certain time t_{wait}, the system is ramped back to the PSB region through RAP and measured using ELR (see Sec. 5.4). Fig. 5.10 shows these spin-orbit-driven rotations as a function of the detuning point chosen for C. At deep detuning, the exchange coupling, J, is very small compared to the spin-orbit drive, ΔE_Z. The rotation axis, therefore, will be very nearly aligned with the X axis of the Bloch sphere. As point C is moved to smaller detuning, J increases. This results in an increase in the rotation frequency because the driving energy is now a vector sum of J and ΔE_Z: $f = \frac{1}{h}\sqrt{J^2 + \Delta E_Z{}^2}$, where h is Planck's constant. The increase in J also causes a decrease in the angle $\phi = \arctan(\Delta E_Z / J)$ between the rotation axis and the Z axis of the Bloch sphere. This in turn effects a decrease in the visibility of the rotations. When the chosen operating point is at large detuning (where J is very small), these spin-orbit-driven rotations are referred to as rotations around the X axis of the Bloch sphere.

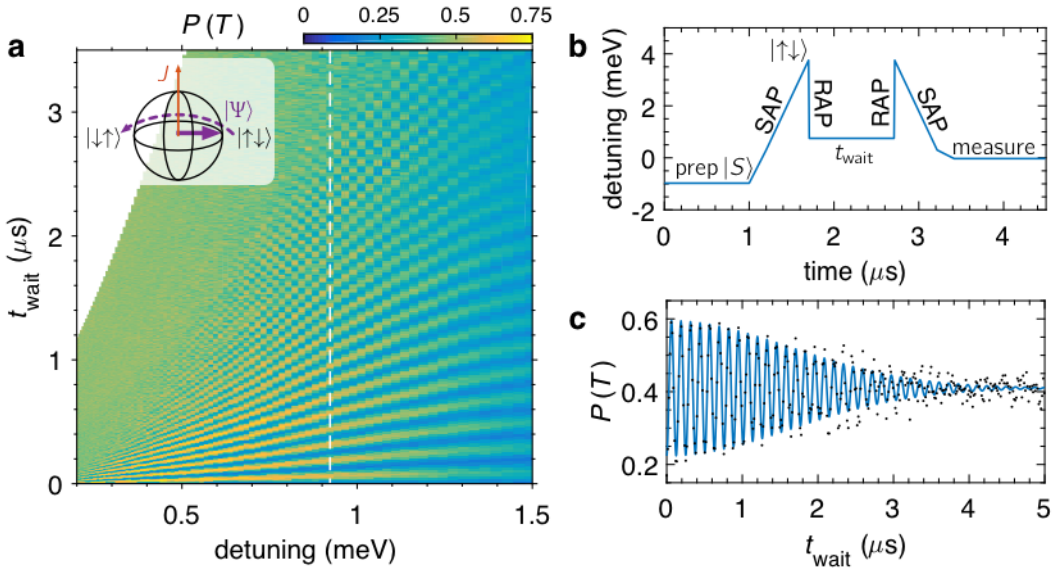

Figure 5.11: (a) Triplet return probability as a function of the duration and operating point of the pulse sequence shown in **(b)**. The deep detuning point from which the J pulse originates is situated at $\varepsilon = 3.75$ meV. **(c)** Line cut taken along the dashed white line in **(a)** showing decaying oscillations of the triplet probability. The solid line corresponds to a fit to the data. The applied external magnetic field is 1.1 T.

5.7.2 Exchange-driven gates

The second DC-controlled gate is driven by the exchange interaction between the two electrons in the DQD. In order to observe these rotations, the qubit is initialized along the X axis of the Bloch sphere by loading $(2,0)S$ then transferring the state to $|\uparrow\downarrow\rangle$ through SAP to point C at deep detuning. Then, J is turned on by ramping rapidly to smaller detuning. The system is left to evolve for a time t_{wait} before turning J off by ramping rapidly back to point C. Finally, the system is transferred through SAP to the PSB region and the spin state is measured using ELR. Fig. 5.11 shows such J-driven rotations as a function of the detuning point at which t_{wait} occurs. The point C at which the $|\uparrow\downarrow\rangle$ state is initialized and from which the rapid J pulse originates is at $\varepsilon = 3.75$ meV. As expected, increasing the detuning decreases J, which in turn decreases the frequency of the observed rotations. This reduction in J also causes the angle ϕ to increase, meaning that the rotation axis starts to approach the X axis of the Bloch sphere, resulting in a drop in the visibility of the rotations. Because ΔE_Z is never completely off in the (1,1) region, the axis of these J-driven rotations will never be exactly aligned with the Z axis of the Bloch sphere, even

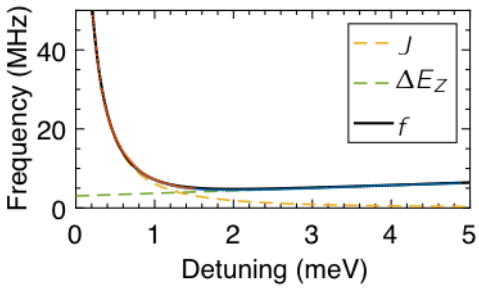

Figure 5.12: Frequency of the spin-orbit-driven (blue data points) and J-driven (red data points) rotations as a function of detuning. The data was extracted by fitting decaying sine waves to vertical line cuts in Fig. 5.10(a) and Fig. 5.11(a), respectively. The black solid line is a fit to the data. The dashed yellow and green lines show the contributions of J and ΔE_Z, respectively, to the total frequency of the qubit.

when C is near $\varepsilon = 0$. Because of this, these J-driven rotation will not be referred to as rotations around the Z axis, but rather as rotations around a N axis whose angle relative to the axes of the Bloch sphere is dependent on the choice of operating point.

5.7.3 Extracting device parameters from DC-controlled measurements

For both the spin-orbit-driven and J-driven DC-controlled gates, measuring a time trace at a fixed detuning point yields data showing qubit rotations which decay over time. Examples of two such time traces are shown in Fig. 5.10(c) and Fig. 5.11(c). These decaying time traces are, in fact, sine waves with a Gaussian-shaped envelope, and can be fit using

$$P_T(t) = A\,\mathrm{e}^{-(t/t_{\mathrm{rel}})^2}\sin(2\pi f t + \theta) + C,$$

where f is the frequency of the qubit rotations, A is their initial amplitude, t_{rel} is the relaxation time, θ is the phase of the sine wave and C is the triplet probability to which the oscillations decay. By applying this fit to all vertical line cuts of Fig. 5.10(a) and Fig. 5.11(a), the qubit frequency can be extracted for a wide range of detuning. This data is shown in Fig. 5.12. Because the qubit frequency is dependent on the total driving energy, it can be used to extract various device parameters, such as the tunnel coupling, as described below.

The expression used for the exchange interaction is

$$J(\varepsilon) = \frac{1}{2}\left(J_{(2,0)} - \sqrt{\left(\varepsilon + J_{(2,0)}\right)^2 + {t_T}^2} + \sqrt{\varepsilon^2 + {t_S}^2}\right), \tag{5.8}$$

which is equivalent to Eq. (5.7), previously used while performing a fit to the spin funnel. The expression for ΔE_Z is far more straightforward than the one for J. In Fig. 5.12, it is obseved that the qubit frequency varies linearly at large detuning, where J becomes negligible and ΔE_Z dominates. The difference in Zeeman energy between the dots can therefore be expressed as:

$$\Delta E_Z(\varepsilon) = h \cdot (m \cdot \varepsilon + b), \tag{5.9}$$

where $h = 4.136 \times 10^{-3}$ μeV/MHz is Planck's constant, and m and b are merely the slope and offset of the linear change in frequency observed in Fig. 5.12, respectively. The total frequency of the qubit, which is driven by the vector sum of J and ΔE_Z, is therefore given by

$$\begin{aligned} f(\varepsilon) &= \frac{1}{h} \cdot \sqrt{J(\varepsilon)^2 + \Delta E_Z(\varepsilon)^2} \\ &= \text{sqrt}\left[\frac{1}{4h^2}\left(J_{(2,0)} - \sqrt{\left(\varepsilon - \varepsilon_0 + J_{(2,0)}\right)^2 + {t_T}^2} + \sqrt{(\varepsilon - \varepsilon_0)^2 + {t_S}^2}\right)^2 \right. \\ &\qquad \left. + (m \cdot (\varepsilon - \varepsilon_0) + b)^2\right]. \end{aligned} \tag{5.10}$$

In Eq. (5.10), ε_0 is used to compensate for any error in the choice of the zero-detuning point. $J_{(2,0)} = 330$ μeV is extracted from a magnetospectroscopy measurement (see Sec. 2.3.6), while t_S, t_T, ε_0, m and b are kept as fit parameters. The values of these parameters extracted from a fit to the qubit frequency (solid black line in Fig. 5.12) are listed in Tab. 5.3.

Table 5.3: Parameters extracted from a fit to the frequency of the DC-controlled gates.

Parameter	value
t_S	21.97 μeV
t_T	22.00 μeV
ε_0	-92.73 μeV
m	6.799×10^{-4} MHz/ μeV
b	2.967 MHz

5.8 AC-controlled gates

As mentioned previously, DC-controlled gates are not the only way to perform quantum operations on a ST qubit. Rotations can also be achieved by varying the detuning during the *Control* pulse in such a way as to generate an oscillating exchange energy, $J(t)$. This oscillating J can, under the right conditions, generate qubit rotations in a manner reminiscent of nuclear magnetic resonance [128] or electron spin resonance [39]. In order to understand how this AC control works, it is helpful to start by studying the more simple example of a single electron spin in an oscillating magnetic field. This is done in Sec. 5.8.1, where helpful tools such as the rotating reference frame and the rotating wave approximation are introduced. In Sec. 5.8.2, these concepts are adapted in order to achieve AC control of the spin-orbit-driven ST qubit. Finally, data taken in the strong driving regime, where the rotating wave approximation no longer applies, is shown in section Sec. 5.8.3.

5.8.1 The rotating frame and the rotating wave approximation

In order to understand how an oscillating field can generate rotations, it is useful to start by studying the case of an electron spin in an oscillating magnetic field. We consider a case where the total magnetic field felt by the spin is:

$$\begin{aligned}\vec{B}(t) &= B_0\hat{\mathbf{z}} + 2B_1\cos(\omega t)\hat{\mathbf{x}} \\ &= B_0\hat{\mathbf{z}} + \{B_1\cos(\omega t)\hat{\mathbf{x}} + B_1\sin(\omega t)\hat{\mathbf{y}}\} \\ &\quad + \{B_1\cos(-\omega t)\hat{\mathbf{x}} + B_1\sin(-\omega t)\hat{\mathbf{y}}\}\,. \end{aligned} \tag{5.11}$$

The total field is the sum of a static field of strength B_0 applied in the $\hat{\mathbf{z}}$ direction and a time-dependent field oscillating in the $\hat{\mathbf{x}}$ direction with amplitude $2B_1$ and angular frequency ω. This oscillating component of the magnetic field can be expressed as the sum of two rotating fields: one rotating counterclockwise and the other clockwise in the xy-plane (first and second brackets in Eq. (5.11), respectively).

The hamiltonian of an electron spin in this magnetic field is given by:

$$H(t) = \underbrace{\frac{\hbar\omega_0}{2}\sigma_z}_{\text{static field}} + \underbrace{\frac{\hbar\omega_1}{2}\begin{pmatrix} 0 & e^{-i\omega t} \\ e^{+i\omega t} & 0 \end{pmatrix}}_{\text{counterclockwise field}} + \underbrace{\frac{\hbar\omega_1}{2}\begin{pmatrix} 0 & e^{+i\omega t} \\ e^{-i\omega t} & 0 \end{pmatrix}}_{\text{clockwise field}} \tag{5.12}$$

where $\omega_i = g\mu_B B_i/\hbar$ is the Larmor frequency associated with the magnetic field of strength B_i, and σ_z is a Pauli matrix.[3] Because this Hamiltonian is time-dependent, it is not immediately obvious how the electron spin will evolve. A useful trick is to examine the system from a reference frame that is rotating counterclockwise around the $\hat{\mathbf{z}}$ axis at the same frequency, ω, as the oscillating magnetic field. $R(t) = \exp(+i\omega t\sigma_z/2)$ is the unitary operator used to move from the fixed lab frame, where the spin state is $|\psi(t)\rangle$, to the rotating frame, where the state is $|\widetilde{\psi}(t)\rangle = R(t)\,|\psi(t)\rangle$. In this rotating reference frame, Eq. (5.12) becomes (the time dependence is dropped to simplify notation):

$$\begin{aligned} \widetilde{H} &= RHR^\dagger + i\hbar\left(\frac{\mathrm{d}}{\mathrm{d}t}R\right)R^\dagger \\ &= \underbrace{-\frac{\hbar\Delta\omega}{2}\sigma_z}_{\text{static field}} + \underbrace{\frac{\hbar\omega_1}{2}\sigma_x}_{\text{c-clockwise field}} + \underbrace{\frac{\hbar\omega_1}{2}\begin{pmatrix} 0 & e^{+2i(\omega_0+\Delta\omega)t} \\ e^{-2i(\omega_0+\Delta\omega)t} & 0 \end{pmatrix}}_{\text{clockwise field}}, \end{aligned} \tag{5.13}$$

where $\Delta\omega = \omega - \omega_0$. We see that, in the rotating frame, the portion of the Hamiltonian resulting from the counterclockwise-rotating field (i.e. the rotating term) is no longer time dependent. On the other hand, the portion of the Hamiltonian resulting from the clockwise-rotating field (i.e. the counter-rotating term) evolves quickly at a frequency of $2(\omega_0 + \Delta\omega)$.

[3] The Pauli matrices are: $\sigma_x = \left(\begin{smallmatrix} 0 & 1 \\ 1 & 0 \end{smallmatrix}\right)$, $\sigma_y = \left(\begin{smallmatrix} 0 & -i \\ i & 0 \end{smallmatrix}\right)$, and $\sigma_z = \left(\begin{smallmatrix} 1 & 0 \\ 0 & -1 \end{smallmatrix}\right)$.

In order to continue the analysis of the system, the rotating wave approximation (RWA) must be applied. In this approximation, the counter-rotating term of Eq. (5.13), which evolves quickly over time, is neglected. This is a valid approximation if the drive is small ($\omega_1 \ll \omega_0 + \Delta\omega$) and if the oscillating magnetic field is near resonance with the static field ($\Delta\omega \ll \omega_0$). Finally, using the RWA and choosing $\omega = \omega_0$, the Hamiltonian of the spin can be written as:

$$\widetilde{H}_{\text{RWA}} = \frac{\hbar\omega_1}{2}\sigma_x. \tag{5.14}$$

It is clear from this Hamiltonian that an oscillating magnetic field applied in the $\hat{\mathbf{x}}$ direction will result in rotations around the $\hat{\mathbf{x}}$ axis of the rotating reference frame if it is resonant with the Larmor frequency of the static field applied in the $\hat{\mathbf{z}}$ direction. Rotations around the $\hat{\mathbf{y}}$ axis of the rotating frame can be achieved in a similar fashion, simply by adding a phase to the oscillating magnetic field:

$$\vec{B}(t) = B_0\hat{\mathbf{z}} + 2B_1\cos(\omega t + \pi/2)\hat{\mathbf{x}}.$$

5.8.2 AC-controlled gates on a ST qubit

Now that it has been demonstrated how an oscillating transverse magnetic field can be used to generate rotations of a spin 1/2 particle in a static magnetic field, similar techniques can be used to perform coherent rotations of the spin-orbit-driven ST qubit. Deep in the (1,1) charge stability region, ΔE_Z dominates and will play the role of the static magnetic field. J is small and oriented perpendicular to ΔE_Z, and will be used in lieu of the transverse oscillating magnetic field. In this case, the rotating reference frame will be turning in a counterclockwise direction around the X axis of the Bloch sphere in the fixed laboratory frame. This direction will be referred to as the Z axis of the rotating frame. The oscillating strength of J will produce rotations around the X axis of the rotating frame.

A time dependent J of the form $J(t) = A\sin(2\pi f t + \phi) + B$ can be achieved by using Eq. (5.8) to calculate the appropriate signal $\varepsilon(t)$ that must be applied to the detuning. However, solving this equation is not trivial and requires a precise knowledge of the device parameters (which may have drifted slightly since the last time they were measured and would require lengthy measurement and analysis to

extract anew). In the AC-controlled experiments presented in this thesis, an oscillating detuning signal of the form $\varepsilon(t) = A\sin(2\pi ft + \phi) + \varepsilon_C$ is applied to the device. Here, A is the chosen driving amplitude and ε_C is the detuning of the *Control* step. In this case, the resulting $J(t)$ is more complex, but as it is a periodic function, it can be written as a sum of a sine wave with frequency f and its harmonics. As f is chosen to be on resonance with ΔE_Z, any harmonic will be off resonance by at least $\omega = 2\pi f$. Therefore, in situations where the RWA applies, these harmonics should also have a negligible effect on the qubit rotations.

Another detail to keep in mind is that ΔE_Z varies with detuning, as seen in Fig. 5.12. This means that oscillations in detuning will result in oscillations of ΔE_Z. However, the resulting relative change in ΔE_Z can, in most cases, be chosen to be smaller than the relative change in J. As the average value of ΔE_Z while the detuning is oscillating is $\Delta E_Z(\varepsilon_C)$, this is the energy that must be taken into account when choosing the frequency of the oscillating field.

In order to produce AC-controlled rotations of the ST qubit, the system is initialized along the X axis of the Bloch sphere by loading $(2,0)S$ then transferring the state to $|\uparrow\downarrow\rangle$ through SAP to point C at deep detuning. An oscillating detuning signal is then applied for a certain time, t_{drive}. If the oscillating signal is applied on resonance with the spin-orbit-driven rotations observed at point C, Rabi rotations between the $|\uparrow\downarrow\rangle$ and $|\downarrow\uparrow\rangle$ states are produced. These rotations correspond to a SWAP operation between the two spins in the DQD. SAP back to the PSB region maps $|\uparrow\downarrow\rangle$ and $|\downarrow\uparrow\rangle$ to $|S\rangle$ and $|T_0\rangle$, respectively, before readout of the spin state is performed using ELR. Rotations of the ST qubit performed using this AC-control scheme are shown in Fig. 5.13.

The effect of the driving frequency on the Rabi rotations is shown in Fig. 5.13(a). As expected from Eq. (5.13), the qubit rotations increase in frequency and decrease in visibility as the drive frequency is moved away from resonance, creating a chevron-like pattern. This chevron is centred at $\sim$ 6.2 MHz (dashed white line), which is consistent with the spin-orbit-driven rotation frequency of 6.17 MHz which was measured at the *Control* point shortly before the scan. The slight wobble seen in the centre position of the chevron in Fig. 5.13(a) is a consequence of magnetic noise and a slow drift in the qubit resonance frequency over the course of the scan, which took 24 minutes to acquire (see Sec. 6.5).

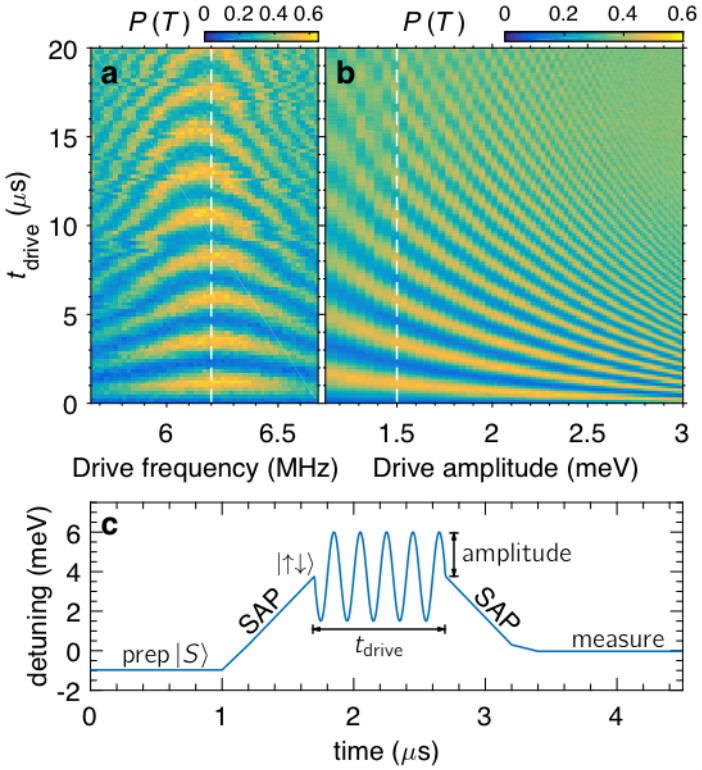

Figure 5.13: (a) Triplet return probability as a function of the frequency and duration of the AC drive applied in the pulse sequence shown in **(c)**. The amplitude of the AC drive used is 1.5 meV (dashed white line in **(b)**). **(b)** Triplet return probability as a function of the amplitude and duration of the AC drive applied. The frequency of the AC drive used is 6.2 MHz (dashed white line in **(a)**). **(c)** Typical pulse used to perform AC-driven rotations on the ST qubit. A sine wave is applied to the detuning point during the *Control* portion of the pulse. The external magnetic field is 1 T.

The effect of the driving amplitude on the Rabi rotations is shown in Fig. 5.13(b). In this measurement, the qubit is driven on resonance, at a frequency of 6.2 MHz in order to maximize the visibility of the Rabi oscillations. Increasing the amplitude of the detuning drive results in an increase in the amplitude of the resulting J signal. This, in turn, leads to an increase in the Rabi frequency of the resulting AC-driven rotations, as expected from Eq. (5.14).

5.8.3 Strong driving regime

As mentioned in Sec. 5.8.1, in order for the rotating wave approximation (RWA) to be reasonable, the Rabi frequency, ω_1, must be small compared to the Larmor frequency, ω_0. On the other hand, the desire to perform qubit operations quickly in order to achieve high fidelity has led to proposals for how to control qubits beyond the limits of the RWA [129, 130]. For most semiconducting qubits, however, this regime is incredibly difficult to reach. Indeed, when a coplanar waveguide is used to generate oscillating magnetic fields, photon-assisted tunnelling and device heating limit the strength of the microwave power, and therefore the amplitude of the oscillating magnetic field, that can be applied [39]. In devices where micromagnets are used [131], the amplitude of the slanting fields which generate the oscillating magnetic fields have thus far been small compared the external fields applied to magnetize the micromagnets. Strong driving (i.e. driving in a regime where the RWA breaks down) has been demonstrated in a nitrogen vacancy center in diamond [132], where large microwave powers could be applied because the experiment was performed at room temperature, and in a microwave-dressed donor-bound electron spin in silicon [133], where strong driving could be reached with moderate microwave power because the precession frequency of the dressed qubit is much smaller than that of its spin qubit counterpart. Until now, strong driving of a semiconducting spin qubit has never been demonstrated at low temperature.

The spin-orbit-driven ST qubit is an ideal candidate for studying the strong driving regime. Indeed, J, which serves as the oscillating field, can easily be pulsed to values largely exceeding that of ΔE_Z, which serves as the static field. In order to increase the amplitude of the oscillating J signal, one must simply increase the amplitude of the AC drive applied to the detuning during the *Control* step of the pulse (see Fig. 5.13(c)). The Rabi rotations resulting from strong driving are shown in Fig. 5.14. In this regime, the AC-controlled gate resembles a series of exchange-driven gates (Sec. 5.7.2) performed on resonance with the external magnetic field rather than a smooth rotation around a fixed axis. This is because the amplitude of the AC drive on J is comparable to (or even larger than) ΔE_Z. Every time J is turned on the qubit turns by a significant angle around the Z axis of the Bloch sphere. This is highlighted by the time traces shown in Fig. 5.14(b-d) where rotations of $\pi/2$, $\pi/3$, and $\pi/4$, respectively, are applied every time that J is turned on during the

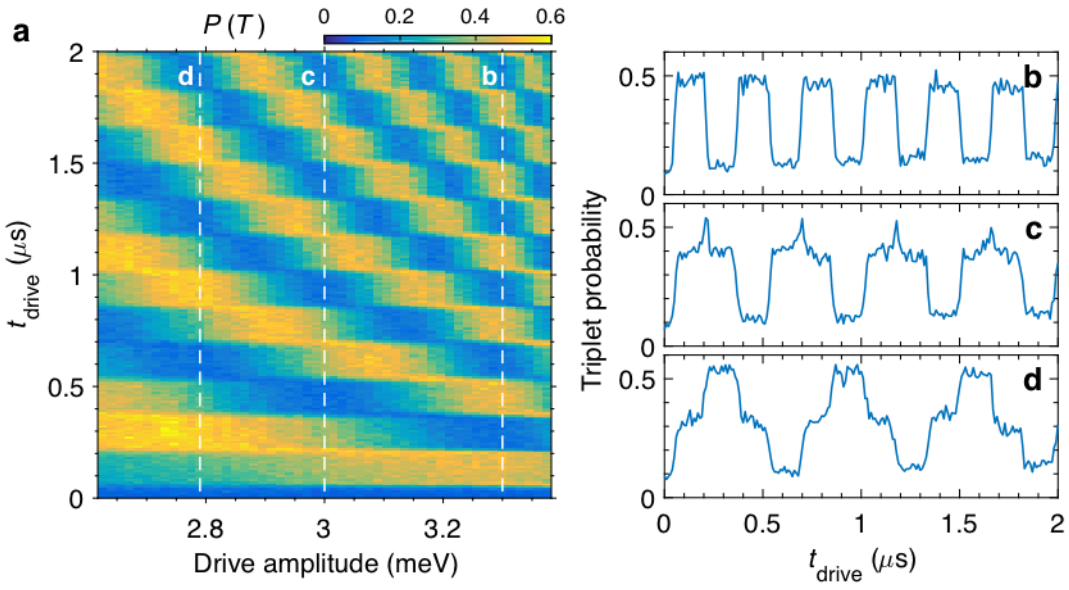

Figure 5.14: (a) Triplet return probability as a function of the amplitude and duration of the AC drive applied. The frequency of the AC drive used is 6.2 MHz. The external magnetic field applied is 1 T. **(b-d)** Line cuts taken along the dashed white lines in **(a)**.

AC drive. During the portion of the drive where J is small, the qubit does not evolve and plateaus are observed. This is what leads the illusion of horizontal stripes in Fig. 5.14(a). Because the Rabi rotations appear as a series of plateaus rather than a smooth curve, the drive amplitude as well as the drive time must be carefully calibrated in order to rotate the qubit by a specific angle.

It is obvious from Fig. 5.14 that the strong driving regime has been reached and that Eq. (5.14) can no longer be used to describe the evolution of the qubit when it is subjected to the oscillating signal on J. Furthermore, the strong drive can cause a change, know as the Bloch-Siegert shift, in the resonance frequency of the qubit [134]. Thankfully, several methods have already been developed to describe the qubit evolution in such situations [135, 136]. The high control on the drive strength and the ease with which the strong driving regime can be reached makes this spin-orbit-driven ST qubit and ideal candidate for testing proposed methods for improving qubit control and gate fidelity beyond the rotating wave approximation [129, 130, 137].

Chapter 6

Analyzing the fidelity of a spin-orbit-driven singlet-triplet qubit using gate set tomography

An important characteristic of any qubit operation is its fidelity, which is essentially a measure of how well and reliably it can be performed. For any given qubit, different values of fidelity can be reported for different types of operations such as state preparation, one- or two-qubit gate operations, and readout. A fidelity of 100% means that an operation can be performed without error every time, while a fidelity of 50% means that the results produced are entirely random. The presence of noise in the qubit's environment as well as other factors, such as limitations on the control electronics, will lead to lower fidelities. Because noise is unavoidable, quantum error correction [13, 14] will play an essential role when performing large computations on a quantum computer. In order to achieve fault tolerant quantum computation, unitary gate operations should have fidelities higher than 99% [138, 139], and fidelities largely exceeding this threshold (i.e. >99.9%) are usually the goal. Recently, one-qubit gate operations exceeding 99.9% fidelity [68] and two-qubit controlled-rotations of 98% fidelity [69] have been demonstrated in isotopically-enriched quantum dot devices fabricated in Si/SiGe and Si-MOS, respectively. These results mark important milestones towards building a universal quantum computer in silicon.

In Chapter 5, the spin-orbit-driven singlet-triplet qubit was studied and two distinct methods for achieving arbitrary single-qubit rotations were demonstrated: the AC-controlled gates (see Sec. 5.8), and the DC-controlled gates (see Sec. 5.7). In

the following chapter, gate set tomography is used to investigate the gate fidelity of this qubit and to determine which control scheme leads to the most reliable gate operations. Different methods that can be used for measuring the fidelity of quantum gate operations are presented in Sec. 6.1, and their various advantages and drawbacks are mentioned. In Sec. 6.2, gate set tomography is presented in greater detail. The method used to implement this relatively new tomography process is also discussed. Finally, the results obtained after performing gate set tomography on the AC- and DC-controlled gates are presented in Sec. 6.3 and Sec. 6.4, respectively.

Contributions: K.M. Rudinger, M.S. Carroll, and C.B.-O. designed the gate set tomography experiments. K.M. Rudinger, N.T. Jacobson, and E. Nielsen provided theoretical support. The data acquisition code used to acquire all the data presented in this chapter was written by C.B.-O. and is an adaptation of the acquisition code used for the experiments presented in Chapter 5. All the data acquisition and analysis of results was performed by C.B.-O.

6.1 Methods for measuring fidelity

6.1.1 Quality factor measurements

Different definitions of the quality factor, Q, can be found in the literature. Some define it as the number of qubit oscillations that occur during the time it takes for their amplitude decays to $1/e$ of its initial value [140, 141, 142, 143], while others define it as the number of qubit operations (e.g. π rotations) that can be performed in this same amount of time [68, 144, 145]. In this work, the first of these definitions is used and Q is calculated in the following manner:

$$Q = f T_{\text{decay}} \ , \tag{6.1}$$

where f is the rotation frequency of the qubit, and T_{decay} is the $1/e$ decay time. The quality factor of the qubit rotations is often used as a measure of how good a qubit is. Occasionally, it is used to compare two qubits when the gate fidelities are not available. Q can also be used to estimate the fidelity by assuming $\mathcal{F} \approx \mathrm{e}^{-(1/Q_N)}$ for

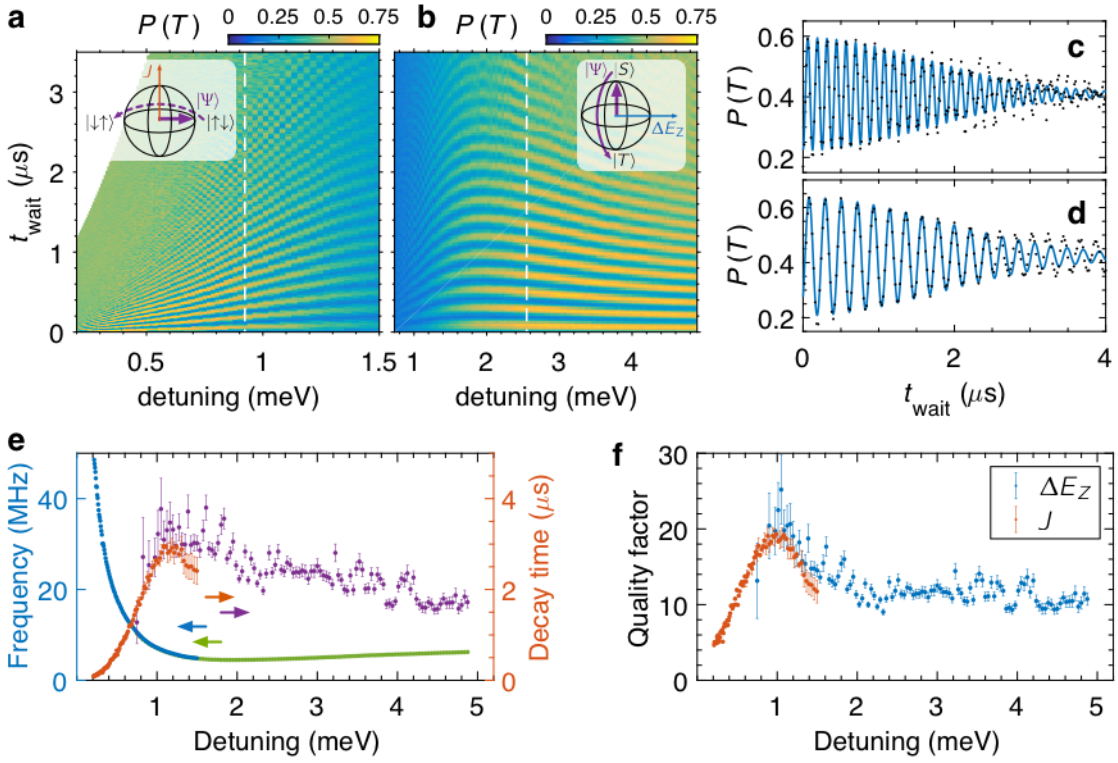

Figure 6.1: (a-b) Triplet return probability as a function of the duration and operating point for **(a)** exchange-driven and **(b)** spin-orbit-driven rotations. The applied external magnetic field is 1.1 T. **(c-d)** Line cuts taken along the dashed white lines in **(a-b)**, respectively, showing decaying oscillations of the triplet probability. The fits (solid blue lines) correspond to sine waves with Gaussian-shaped envelopes. **(e)** Qubit rotation frequency and decay time as a function of detuning, obtained by fitting a decaying sine wave, as shown in **(c-d)**, to all vertical line cuts of **(a)** (blue and red data points) and **(b)** (green and purple data points). **(f)** Quality factor as a function of detuning.

exponentially decaying oscillations [145] and $\mathcal{F} \approx \mathrm{e}^{-(1/Q_N)^2}$ for ones with Gaussian-shaped decay [143], though this practice is questionable. Here, $\mathcal{F}$ is the fidelity and Q_N is the number of qubit operations that can be performed during the $1/e$ decay time. $Q_N = 2Q$ for π rotations and $Q_N = 4Q$ for $\pi/2$ rotations.

Fig. 6.1 shows how the quality factor is measured for the DC-controlled gates (see Sec. 5.7). Decaying sine waves with a Gaussian-shaped envelope are fit to each individual time trace (vertical line cuts) in Fig. 6.1(a-b) using

$$P_T(t) = A\,\mathrm{e}^{-(t/T_{\mathrm{decay}})^2}\sin(2\pi f t + \theta) + C, \tag{6.2}$$

where $P_T(t)$ is the time-dependent triplet probabilty, A is the initial amplitude of the rotations, θ is the phase of the sine wave, and C is the signal to which the oscillations decay. The Gaussian shape of the decay envelope indicates that there is Gaussian-distributed low-frequency exchange noise present in the system [146]. Once the frequency and decay time have been extracted using this fit, (6.1) is used to calculate Q. We see from Fig. 6.1(f) that the quality factor is $Q = 10$ when the detuning is large. This value is relatively constant because the slowly decreasing T_{decay} is compensated by a slightly increasing frequency. At very small detuning, charge noise leads to short T_{decay}, which in turn leads to small values of Q. The highest quality factor of $Q = 20$ is observed at a detuning of $\varepsilon = 1.0$ meV.

Fig. 6.2 shows how the quality factor is measured for AC-controlled gates (see Sec. 5.8.2). Chevron scans, such as the one shown in Fig. 5.13(a), are measured for different drive amplitudes, and time traces are extracted at the qubit resonance frequency (i.e. at the frequency around which the chevron is centred). The frequency and decay time of the resonantly-driven AC-rotations are extracted by performing a fit to these time traces. This time, the fit is a decaying sine wave with an exponential envelope:

$$P_T(t) = A\,\mathrm{e}^{-(t/T_{\text{decay}})}\sin(2\pi f t + \theta) + A_2\,\mathrm{e}^{-(t/T')} + C\,.$$

where the second term has been added to account for the observed decay in the centre position of the sine wave, and all other variables are as defined previously. The exponential shape of the decay envelope indicates that there is either Lorentzian-distributed low-frequency exchange noise or Gaussian-distributed white noise in the system [146]. As expected, the Rabi frequency increases for larger drive amplitudes. The decay time, however, decreases with drive amplitude. This leads to a quality factor of $Q \approx 3$ which is more or less constant over the range of drive amplitudes studied.

6.1.2 Process tomography

One method commonly used to extract the fidelity of a qubit operation is quantum process tomography (QPT) [147, 148, 149, 150]. Though different implementations exist [151], most rely on having a good knowledge of the qubit state before and after the application of a quantum gate. If the initial and final states of the qubit are well

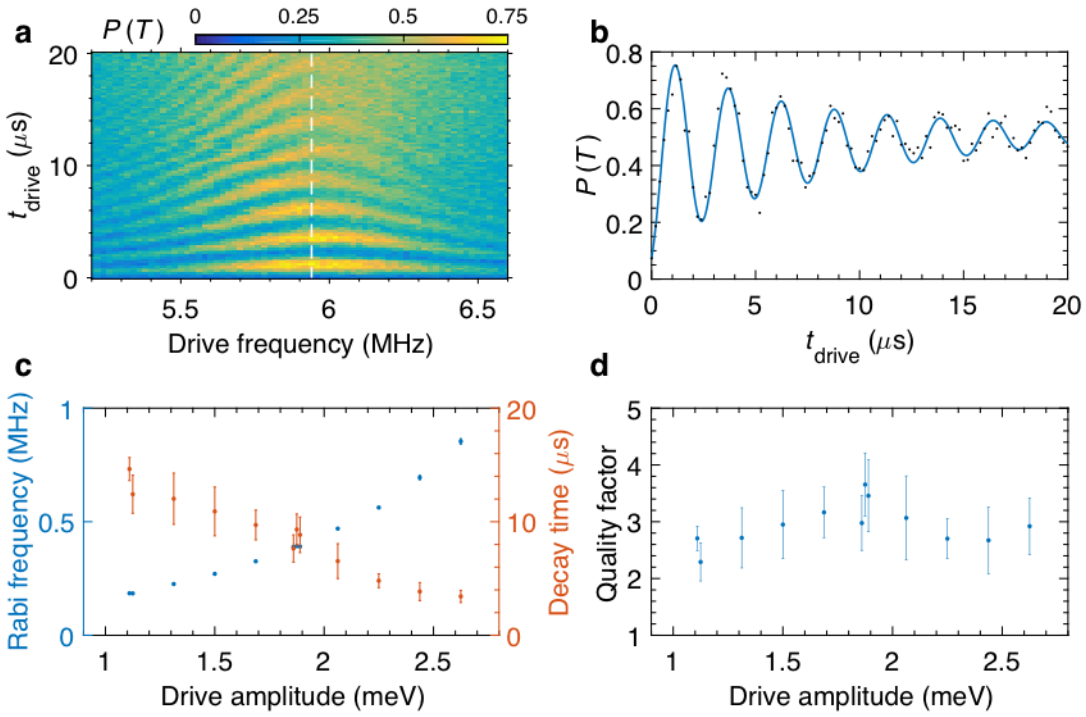

Figure 6.2: (a) Triplet return probability as a function of the duration and the driving frequency of AC-controlled rotations. The drive amplitude is 1.88 meV and the applied external magnetic field is 1.1 T. **(b)** Line cut taken along the dashed white line in **(a)** showing decaying oscillations of the triplet probability. The fit (solid blue line) corresponds to a sine wave with an exponential envelope. **(c)** Qubit rotation frequency (blue) and decay time (red) as a function of the drive amplitude obtained by fitting a decaying sine wave, as shown in **(b)**, to vertical line cuts taken at the resonance frequency of various chevron plots such as the one shown in **(a)**. **(d)** Quality factor as a function of the drive amplitude.

known, the operation that was performed to take the qubit from one state to the other can be inferred through linear algebra. Quantum state tomography [12] is therefore a crucial method to master in order to perform quantum process tomography. Quantum state tomography, for its part, consists in measuring the expectation values of a set of observables (e.g. along the bases of the qubit subspace) on many quantum systems prepared in an identical fashion in order to estimate their state.

One of the main drawbacks of quantum process tomography is that it cannot differentiate the error on the quantum gate of interest from those associated with the preparation or measurement processes. If the gates used to perform quantum state tomography are noisy, they will impose an upper bound on the fidelity reported

for the gate being studied [152]. Additionally, quantum process tomography does not inform the user if the gate performs equally well when it is the N^{th} gate in a concatenated sequence of gates as it does when it is the first (or only) one in the sequence. Finally, because the complexity of quantum process tomography scales exponentially with the number of qubits, it quickly becomes inefficient as the size of the quantum system is increased.

6.1.3 Randomized benchmarking

Randomized benchmarking (RB) [152, 153, 154, 155] is perhaps the most commonly used method for measuring a qubit's gate fidelity. Its usual implementation consists in applying random sequences of Clifford gates [156] to a qubit prepared in a known initial state. A recovery Clifford operation is then applied to align the qubit state with the measurement basis. Finally, readout is performed and the outcome of the measurement is compared to the expected result. By measuring the increase of the measurement error probability as a function of the length of the random sequence of Clifford gates, the average error per Clifford gate can be extracted. In practice, the single-qubit gates of interest are usually $\pi/2$ rotations around two orthogonal axes of the Bloch sphere (e.g. $G_X = X_{\pi/2}$ and $G_Y = Y_{\pi/2}$). In order to extract the fidelity of these gates using randomized benchmarking, the 24 Clifford gates must first be constructed using these two gates. When two orthogonal axes of rotation are available, each Clifford gate requires an average of 1.875 rotations [157]. Therefore, once the average error rate per Clifford gate is extracted, the value is divided by 1.875 in order to obtain the average error rate per gate rotation. More advanced variations of this RB method, such as interleaved RB [158, 159], have been developed and allow the average error rate of an individual quantum gate, rather than the average error per Clifford gate, to be extracted.

Because it relies on measuring the evolution of the error rate as a function of the length of the gate sequence applied to the qubit, randomized benchmarking can measure high gate fidelities without being limited by the accuracy of the state preparation and measurement, as was the case with quantum process tomography. However, randomized benchmarking is relatively insensitive to coherent errors [160] and provides little information on how to improve the individual quantum gates. Furthermore, in systems such as the ST qubit where the natural axes of control

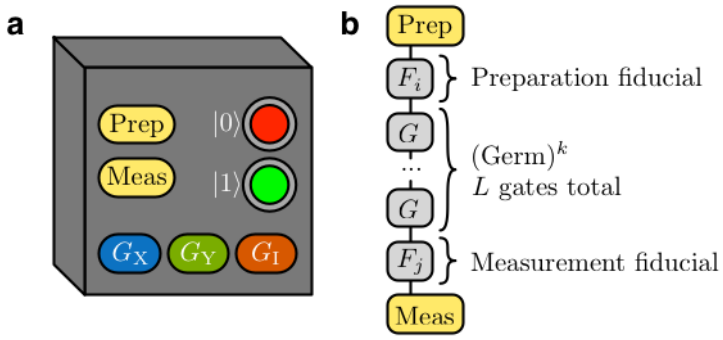

Figure 6.3: This figure is a reproduction of part of Figure 1 from Blume-Kohout *et al.* [167] **(a)** Black box representing the qubit, as seen by the GST model. The classical interface consists of buttons to prepare, measure, and apply gate operations to the qubit, as well as lights used to indicate the outcome of the measurement. **(b)** Construction of a gate sequence used in the GST experiment.

are non-orthogonal [56], the construction of Clifford gates is not trivial [161] and, consequently, randomized benchmarking is difficult to implement. An example of RB being implemented on a qubit with two rotation axes separated by 120°can be seen in Andrews *et al.* [162], where an average of 2.7 individual rotations of varying angles are needed to construct each of the Clifford gates.

6.1.4 Gate set tomography

Gate set tomography (GST) [163, 164, 165] is yet another tool that can be used to characterize qubit operations. It is based on the concept that playing around with a quantum device should provide the user with the information needed to deduce the device's behaviour and predict the outcomes of future experiments [164, 166]. When performing GST, the qubit can be seen as a black box with buttons that can be pressed to prepare the qubit in an initial state, to apply various gate operations, and to measure the qubit. The black box is also equipped with a means of reading the result of the qubit's two-outcome measurement. An example of this black box representation of a qubit is illustrated in Fig. 6.3(a). GST only relies on two assumptions: the first is that the qubit has a two-dimensional Hilbert space; the second is that the gate operations are Markovian and do not change over time [167]. No other assumptions regarding the initial state, the measurement basis, or the effect of the gate operations is needed for GST to work. However, having some inkling of the

effect of the gate operations can be helpful when constructing the GST experiment, as will be discussed in Sec. 6.2.

In contrast to RB, GST sequences are structured and periodic in order to amplify errors, and can analyze any gate set provided that it is rich enough to prepare an informationally complete set of probe and measurement states [167]. It provides a full description of every gate in the set, including the axis and angle of each rotation, as well as details about state preparation and measurement (SPAM). GST has already been implemented on orthogonal gate sets in ion-trap qubits [164, 167], in Si/SiGe charge qubits [168], and in spin qubits formed by an electron bound to a ^{31}P donor atom implanted in silicon [169]. It has also been successfully used to debug and optimize the performance of quantum gates in some of these devices [167, 169]. The main drawback of GST is that it assumes that the noise is Markovian. However, all experimental systems will have some degree of non-Markovian noise, such as slow drift or correlations between errors in consecutive gates, which can lead to model violations and bad fits in the GST analysis. Moreover, because GST assumes that the qubit is a two-dimensional Hilbert space, it is unable to identify errors caused by leakage to other states.

6.2 Method for performing GST

As mentioned in Sec. 6.1.4, it is not necessary to have any prior information regarding the effect of pressing the "buttons" on the black box qubit in order to perform GST. However, a user may have to play with the black box a very long time before randomly stumbling on the correct sequences in which to press the buttons in order to obtain enough relevant information to perform the GST analysis. Data acquisition for the GST experiment can be greatly optimized by having some prior knowledge of the ideal gates that the qubit is expected to perform.

For the spin-orbit-driven singlet-triplet qubit studied in this work, two distinct target gate sets are considered: the AC-controlled gates (Sec. 5.8) and the DC-controlled gates (Sec. 5.7). For the AC-controlled gate set, the target gates are G_X, G_Y, and G_I. G_X and G_Y are resonantly driven $\pi/2$ rotations around the X and Y axes of the rotating frame, respectively, while G_I is an identity gate that leaves the state of the qubit unchanged. For the DC-controlled gates, the target gates are G_X, G_N, and G_I. G_X and G_I are both spin-orbit-driven rotations (see Sec. 5.7.1) of $\pi/2$ and 2π rad,

respectively, while G_N is an exchange-driven rotation (see Sec. 5.7.2) of $\pi/2$ rad. The G_X and G_I gates are performed at a detuning of $\varepsilon = 3.75$ meV (see Fig. 6.1(b)), where the wavefunction overlap between the two electrons on the double quantum dot is small and the rotations are around the X axis of the Bloch sphere. The G_N gate is performed at small detuning (see Fig. 6.1(a)), where the exchange interaction between the electrons is large. The angle between the rotation axis of the G_N gate and the X axis of the Bloch sphere depends on the detuning at which the G_N gate is performed and can be predicted by performing the analysis described in Sec. 5.7.3.

Once the target gate set has been chosen, the gate sequences for the GST experiment can be constructed using the method illustrated in Fig. 6.3(b). Each gate sequence has three parts: 1) preparation of the qubit to a known initial state, 2) a series of gates, and 3) measurement in a known basis. The series of gates is itself divided into three parts: 1) a preparation fiducial followed by 2) a 'germ' sequence repeated an integer k amount of times and finally 3) a measurement fiducial. The goal of the preparation and measurement fiducials is to provide a sufficiently varied set of input states and measurements to thoroughly probe the effect of the germ studied. For a qubit with a two-dimensional Hilbert space, this requires a minimum of four different fiducials. The germs are operations of interest such as the gates themselves, as well as short sequences of gates that are specifically chosen to amplify errors such as over- or under-rotations in the individual gates and tilt errors on their rotation axes. Repeating the germs an integer k times will amplify these errors and allow deviations from the target gates to be measured with more accuracy. For more information on sequence design, see the 'Methods' section of Blume-Kohout *et al.* [167].

Tab. 6.1 shows the preparation and measurement fiducials, as well as the germs, used to construct the GST sequences for the AC-controlled gate set. The empty brackets, {}, is a null operation meaning "do nothing for no time". It is not the same as the G_I gate, which is also supposed to leave the qubit unchanged but has a non-zero operating time. In this experiment, the qubit is initialized in the $|\uparrow\downarrow\rangle$ state, which corresponds to the Z axis of the Bloch sphere in the rotating frame (see Sec. 5.8.2). The six preparation fiducials, F_i, are chosen to map this initial state to the six Pauli eigenstates (i.e. $\pm X$, $\pm Y$, and $\pm Z$). The measurement fiducials, F_j, are the same as the preparation fiducials and can therefore map any Pauli eigenstate to any other before measurement along the Z axis. The germ sequences are limited to the individ-

Table 6.1: Fiducials and Germs used to construct the GST sequences for the AC-controlled gate set. The G_X and G_Y gates are orthogonal.

Prep fiducials	Meas fiducials	Germs
$\{\}$	$\{\}$	$\{\}$
G_X	G_X	G_X
G_Y	G_Y	G_Y
$G_X G_X$	$G_X G_X$	G_I
$G_X G_X G_X$	$G_X G_X G_X$	
$G_Y G_Y G_Y$	$G_Y G_Y G_Y$	

ual gates studied. Ideally, longer germ sequences would have been used in addition to the ones listed [167]. However, they are discarded in this experiment for technical reasons chiefly pertaining to the memory available in the arbitrary waveform generators used to apply the pulses to the device (see Sec. 5.1). For similar reasons, the germs are repeated only $k = 1$ times when constructing the sequences. Once the germs and fiducials have been chosen, gate sequences of the form $(F_i)(G_m)^k(F_j)$ are constructed. Here, F_i and F_j are preparation and measurement fiducials, respectively, and G_m is a germ that is repeated k times. Gates are applied in reading order (i.e. the gate on the left is the first one to be applied). From the fiducials and germs listed in Tab. 6.1, this construction technique will lead to a list of 144 gate sequences. However, not all the sequences in this list are distinct. For example

$$\begin{aligned}(F_i)(G_m)^k(F_j) &= (G_X)(G_X)^1(G_X)\\ &= (G_X G_X)(\{\})^1(G_X)\\ &= (G_X)(\{\})^1(G_X G_X)\\ &= (G_X G_X G_X)(\{\})^1(\{\})\\ &= (\{\})(\{\})^1(G_X G_X G_X)\end{aligned}$$

are all different combinations of fiducials and germs that result in the same gate sequence: $G_X G_X G_X$. Removing such redundancies from the list of gate sequences leads to a list of 92 distinct experiments to be performed on the qubit.

Tab. 6.2 shows the preparation and measurement fiducials, as well as the germs used to construct the GST sequences for a DC-controlled gate set in which the rotation axes of the G_X and G_N gates are separated by 70°. In this experiment, the qubit

Table 6.2: Fiducials and Germs used to construct the GST sequences for a DC-controlled gate set in which the rotation axes of the G_N and G_X gates are separated by 70°.

Prep fiducials	Meas fiducials	Germs		
{}	{}		{}	
$G_X G_N$	$G_N G_X$	G_I	G_X	G_N
$G_N G_X G_X G_N$	$G_N G_X G_X G_N$	$G_X G_N$	$G_X G_I$	$G_N G_I$
$G_X G_X G_N G_X G_X G_X$	$G_X G_X G_X G_N G_X G_X$			

is initialized in the $|S\rangle$ state, which corresponds to the Z axis of the Bloch sphere in the fixed laboratory frame. Measurements are also performed along this axis. Only four fiducials are used. Their effect is to map the initial state, $|S\rangle$, to four informationally complete input states (forming a somewhat regular tetrahedron on the Bloch sphere). The list of gate sequences is constructed from these fiducials and germs in the same manner as described above for the AC-controlled gate set. Because there are fewer fiducials – and because the DC-controlled gates are faster than their AC counterparts, therefore requiring fewer points in the AWG's memory – germs and their repetitions of total length $L = 2$ are used in the construction of the GST sequences. For the gate set considered in Tab. 6.2, there are 160 experiments in this list. Removal of redundant gate sequences leads to a list of 154 distinct experiments to be performed on the qubit.

Once the list of gate sequences has been determined, it is time to perform these experiments on the qubit and acquire the results needed to conduct the GST analysis. In this work, each sequence in the list is measured a total of $N = 10000$ times. This is done in order to acquire enough statistics to obtain reasonable accuracy on the gate estimates and fidelity measurements. Performing 10^4 repeats for each of the $\mathcal{O}(100)$ sequences in the list requires several minutes of acquisition time ($\sim$ 10 mins). This is on the same time scale as the slow drift in the qubit's spin-orbit-driven precession frequency, which will be discussed in Sec. 6.5. Because this slow drift constitutes non-Markovian noise and may cause issues with the GST analysis, some thought must be put into how the GST experiment will be performed. One possible method, the one most convenient to an experimentalist, would be to consider each sequence in the list individually and repeat each one $N = 10^4$ times consecutively before moving on to the next sequence in the list (i.e. measuring one data set of 10^4 repeats). With

Table 6.3: Measurement outcomes obtained when performing a GST measurement on a DC-controlled gate set where the rotation axes of G_N and G_X gates are separated by 70°. Each data set consists of 100 consecutive measurements on each of the 154 sequences in the list. 100 data sets are acquired so that each sequence is measured a total of $N = 10^4$ times.

	set 1		set 2		set 3		...	set 100	
Sequence	S	T	S	T	S	T		S	T
$\{\}(\{\})\{\}$	74	26	69	31	77	23		75	25
$\{\}(\{\})G_N G_X$	47	53	43	57	48	52		51	49
$\{\}(\{\})G_N G_X G_X G_N$	45	55	46	54	34	66		42	58
⋮									
$G_X G_X G_N G_X G_X G_X (G_N G_I) G_N G_X G_X G_N$	30	70	38	62	38	62		48	52
$G_X G_X G_N G_X G_X G_X (G_N G_I) G_X G_X G_X G_N G_X G_X$	33	67	45	55	36	64		39	61

this approach, there is little drift over the time it takes to measure all 10^4 repeats of a single gate sequence. However, there might be significant differences between the G_m gates performed in the first sequence on the list and those performed in the last one on the list, as they will be measured several minutes apart. With regards to the GST analysis, it is preferable to have the gates be as uniform as possible across all the sequences in the list, even if this results in larger variations between repeats of a given sequence. Therefore, from a theoretical perspective, the ideal data acquisition method would be to measure each sequence in the list once, working through the entire list of sequences a total of 10^4 times (i.e. measuring 10^4 data sets of 1 repeat each). From an experimental standpoint, this approach is harder to implement and leads to longer data acquisition times because it requires more frequent interactions between the computer and the instruments (see Sec. 5.1.2). In this work, a middle ground between these two scenarios is used. Each sequence in the list is measured 100 times consecutively while scanning through the list of sequences 100 times in total (i.e. measuring 100 data sets of 100 repeats each). Single-shot readout (Sec. 5.4.1) is used to determine the outcome of each measurement.

Tab. 6.3 shows the results obtained after performing a GST measurement on a DC-controlled gate set where the rotation axes of the G_X and G_N gates are separated by 70°. The total number of singlet and triplet counts measured for each of the 154

sequences in the list are recorded. Once these results have been obtained, the GST analysis is performed using pyGSTi (python GST implementation), an open-source software developed at Sandia National Laboratories [170]. The report resulting from this analysis contains all the information gleaned regarding the gate set used to generate the data provided. This information includes, but is not limited to, the infidelity of each individual gate, each of their angles and axes of rotation, the operations performed during state preparation and measurement, as well as the error bars on all of these values. Some of the results extracted from GST analysis on the AC- and DC-controlled spin-orbit-driven qubits are presented and discussed in the following sections.

6.3 Gate set tomography of the AC-controlled qubit

Fig. 6.4 shows the "buttons" used to construct the sequences needed to perform GST on the AC-controlled qubit (see Sec. 5.8.2). The *Prep* button initializes the system into the $|\uparrow\downarrow\rangle$ state by loading $(2,0)S$ before ramping into the $(1,1)$ ground state through slow adiabatic passage (SAP, see Sec. 5.5). Similarly, the *Meas* button maps $|\uparrow\downarrow\rangle$ and $|\downarrow\uparrow\rangle$ to $|S\rangle$ and $|T_0\rangle$, respectively, through SAP back to the Pauli spin blockade region before readout of the spin is performed using the enhanced latching readout described in Sec. 5.4. The G_X, G_Y, and G_I gates are performed by applying an oscillating signal to the detuning. This oscillating signal is a sine wave centred around $\varepsilon = 3.75$ meV and its amplitude is varied between the different GST experiments. Driving amplitudes of 1.43 meV, 1.65 meV, and 1.88 meV are used.

For the qubit studied in this work, the frequency of the spin-orbit-driven rotations performed at $\varepsilon = 3.75$ meV are measured to be ~ 300 kHz slower than the AC driving resonance frequency identified by the symmetry point of the chevron scan. Similar shifts in resonance frequency have been reported for other devices, and the origin of this phenomena is not entirely well understood [171]. In the present case, this frequency shift may be due in part to the fact that the qubit is operated near the strongly-driven regime where the rotating wave approximation is not valid (see Sec. 5.8.3).

In order to account for this frequency shift, the frequency of the oscillating drive is calibrated by taking a horizontal line cut through a chevron scan (such as the one shown in Fig. 6.2(a)) and finding its symmetry point. The duration of the G_X and

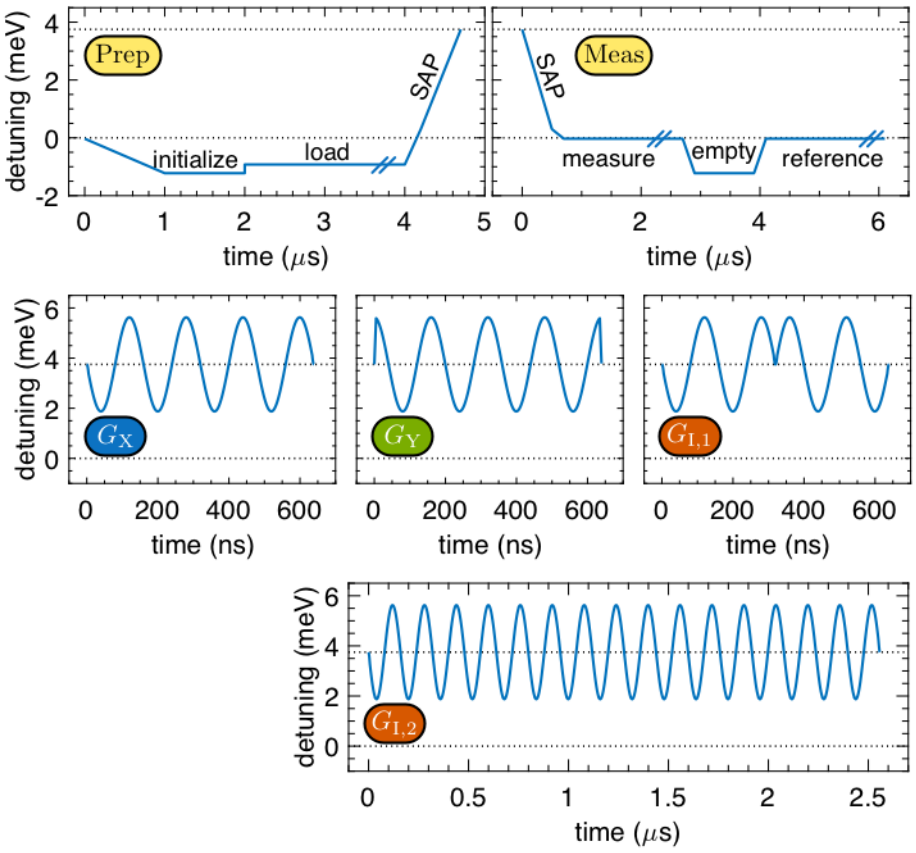

Figure 6.4: Different pulse elements used to construct the gate sequences for the AC-controlled gate set. The *Load*, *Measure*, and *Reference* times have been shortened for clarity. Black dotted lines indicate the $\varepsilon = 0$ meV and $\varepsilon = 3.75$ meV detuning points. The G_X and G_Y gates differ only by their phase. Two different implementations of the G_I pulse are investigated. The first consists of a $X_{\pi/4}$ rotation followed by a $-X_{\pi/4}$ rotation, while the second is a $X_{2\pi}$ gate.

G_Y gates is then calibrated in order to perform $\pi/2$ Rabi rotations. Normally, in the absence of any frequency shift, the G_I gate could be implemented by simply idling at the $\varepsilon = 3.75$ meV detuning point for a duration equal to an integer number of periods of the qubit precession frequency. However, the pulsing code used in this work wrongfully assumes that the qubit precession frequency in the absence of an AC drive is equal to the drive frequency. As this is not the case, performing a G_I gate in this manner would introduce phase errors to any gate sequence in the GST experiment containing such a G_I gate. To avoid this pitfall (and to avoid having to make significant changes to the pulsing code), the G_I gate is also driven. Two different versions of the G_I gate are tested. The first, $G_{I,1}$, consists of a $X_{\pi/4}$

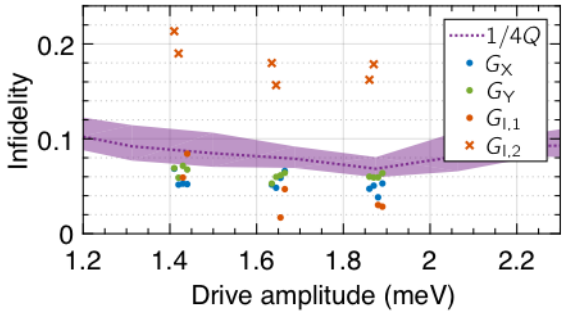

Figure 6.5: Infidelity of the AC-controlled gate set, extracted using GST, as a function of the AC drive's amplitude. The applied external magnetic field is 1.2 T. The purple dotted line and shaded area correspond to the expected infidelity for the G_X and G_Y gates, estimated using the quality factor and its error bars reported in Fig. 6.2 for the AC-controlled rotations.

followed by a $-X_{\pi/4}$ rotation. The second, $G_{I,2}$, is simply a $X_{2\pi}$ rotation. The first version is driven for the same total time as the G_X and G_Y gates, while the second is four times longer in duration. Because of its longer duration, the $G_{I,2}$ gate is expected to have a lower fidelity than the other three gates studied.

Using the "buttons" shown in Fig. 6.4, the 92 distinct experiments resulting from the fiducials and germs listed in Tab. 6.1 can be constructed. Each of these sequences is measured $N = 10^4$ times in the manner described previously. The gate infidelities ($\mathcal{I} = 1 - \mathcal{F}$) extracted through GST analysis of these measurements are shown in Fig. 6.5. The purple shaded region indicates the expected infidelity for the G_X and G_Y gates. These values are calculated from the quality factors reported in Fig. 6.2(d) and assuming

$$\mathcal{I} \approx 1 - e^{-(1/Q_N)} \approx 1/Q_N\,, \tag{6.3}$$

where $Q_N = 4Q$ is the number of G_X and G_Y gates that can be performed within the $1/e$ decay time of the AC-controlled oscillations [145]. Four GST experiments are performed at each of the three driving amplitudes studied: two experiments where the gate set is $\{G_X,G_Y,G_{I,1}\}$, and two experiments where the gate set is $\{G_X,G_Y,G_{I,2}\}$. In Fig. 6.5, some of the data points have been slightly offset horizontally to improve clarity.

The first thing to notice in Fig. 6.5 is that the GST infidelities measured for the G_X, G_Y, and $G_{I,1}$ gates are all of similar value. This is as expected, because these three

gates are of the same duration and differ mainly by the phase of the applied oscillating drive. Their infidelity, $\mathcal{I} \sim 0.06$, is slightly better than the infidelity estimated from the Q-factor measurements. It is important to note, however, that the quality factor measurements were performed with an applied external magnetic field of $B_{\text{ext}} = 1.1$ T, while the GST experiments were performed with an applied field of $B_{\text{ext}} = 1.2$ T. Because of this, the qubit's Rabi frequency was about 9% faster in the GST experiment than in the Q-factor measurement. If the decay time of the oscillations is not made 9% worse by the increase in magnetic field, this could account, at least in part, for the discrepancy between the estimated and measured infidelities. The infidelity of the $G_{\text{I},2}$ gate, $\mathcal{I} \sim 0.18$, is significantly higher than that of the other gates. This is also as expected because the $G_{\text{I},2}$ gate is four times longer than the other three gates tested. Finally, the amplitude of the drive does not seem to have a significant impact on the gate fidelity, though this claim cannot be made with much certainty given the small number of different drive amplitudes measured. This insensitivity to the driving amplitude is also consistent with the quality factor predictions.

In order to confirm that the GST analysis was reasonably successful and that the infidelity values provided can be trusted, the Rabi oscillations are reproduced using the estimated logic gate operations provided in the GST report. This is done using the superoperators (also known as process matrices or Pauli transfer matrices) that describe the logic gate operations, and which are calculated during the GST analysis. An example of the superoperators obtained for the G_{X} and G_{Y} gates are shown in Fig. 6.6(a-b), respectively. Applying the superoperator once to the initial state, which is $|\uparrow\downarrow\rangle = +Z$ in the rotating frame, yields the expectation value of a measurement after a single gate has been performed. Plotting the measurement outcome as a function of the number of gates applied leads to Rabi oscillations, as shown in Fig. 6.6(d-e). In these plots, the X axis is converted to time for a more straightforward comparison with the measured Rabi oscillations shown in Fig. 6.6(c). A decaying sine wave is fit to these calculated Rabi oscillations using

$$P_T(t) = A\, \mathrm{e}^{-(t/T_{\text{decay}})} \sin(2\pi f t + \theta) + C\,. \tag{6.4}$$

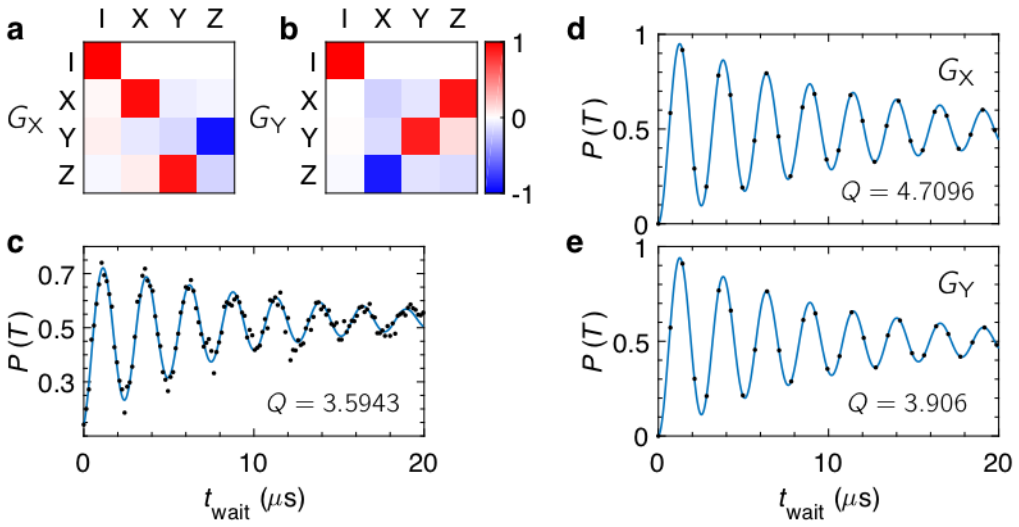

Figure 6.6: (a-b) Superoperator of **(a)** the AC-controlled G_X gate and **(b)** the AC-controlled G_Y gate extracted from the GST report. **(c)** Decay of the Rabi oscillations observed experimentally. **(d-e)** Decay of **(d)** the G_X and **(e)** the G_Y oscillations calculated from the superoperators shown in **(a)** and **(b)**, respectively. Each black dot corresponds to the application of one additional gate (i.e. one matrix multiplication between the superoperator and the vector representing the state of the qubit). The drive amplitude in both the GST and Q-factor experiments is 1.88 meV.

Because GST assumes a Markovian noise model, the decay envelope is exponential. This fit allows the quality factor of the calculated Rabi oscillations to be compared with that of the Rabi oscillations that were measured experimentally.

It is clear from Fig. 6.6(d-e) that the GST gate estimates for G_X and G_Y perform rotations that are slightly larger than $\pi/2$. This may be due to a miscalibration of the time during which the resonant drive is applied, or to a change in the driving driving frequency between the time when the G_X and G_Y gates were calibrated and the time when the GST experiment was performed. It is important to note that, if this over-rotation is systematic and constant throughout the entire duration of the GST measurement, it will not negatively impact the infidelity calculated for these gates. This is because GST makes no assumptions about the effect of the gates being studied (see Sec. 6.1.4). For example, if a gate G_m performs very reliable rotations of 96°around a rotation axis that is separated from the X axis of the Bloch sphere by 2°, the GST analysis will say that the infidelity of G_m is low. The fact that the user wanted to perform an $X_{\pi/2}$ rotation is irrelevant to the GST analysis. The angle and

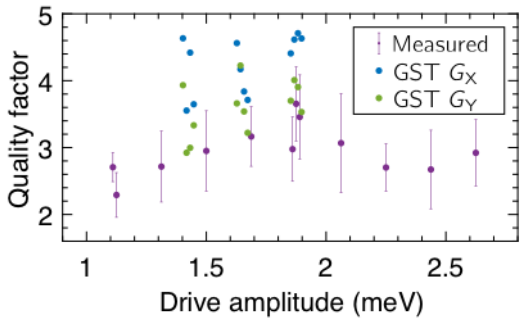

Figure 6.7: Comparison between the measured (purple points) and calculated (blue and green points) quality factors for the AC-controlled qubit rotations. The calculated values are obtained using the superoperators provided by the GST analysis for the G_X and G_Y gates.

axis of the rotation performed by the G_m gate are provided in the GST report and the user can use this information make adjustments to the gate if desired.

Using the method described above, the quality factors of the G_X and G_Y gates are calculated for all the GST experiments that were performed on the AC-controlled qubit. Fig. 6.7 compares these calculated values (blue and green points) to the experimental Q-factors presented in Fig. 6.2(d) (purple points). The Q-factors calculated from the GST gate estimates appear to be consistently higher than the ones measured experimentally. However, this discrepancy is relatively small and some of the calculated Q-values fall within the error bars of the experimentally measured values. As mentioned previously, the GST experiments were performed with a magnetic field of 1.2 T, while the field during the Q-factor measurements was 1.1 T. It is suspected that the measured Q-factors would have been slightly larger had the experiment been performed at 1.2 T, which would have further improved the agreement between the two data sets. Because the GST analysis seems to have provided reasonable gate estimates for the G_X and G_Y gates, it is concluded that the GST analysis of the AC-controlled gate set was successful and that the infidelities reported in Fig. 6.5 accurately describe the performance of the AC-controlled gates.

It is worth mentioning that the G_X and G_Y gates perform a $\sqrt{SWAP}$ operation between the two electron spins that form the ST qubit. Had it been possible to independently initialize and measure each of the two spins, these gates would be referred to as a two-qubit operation. Though the 94% fidelity measured for these gates is not very good when compared to $\mathcal{F} > 99\%$ generally achieved for single-

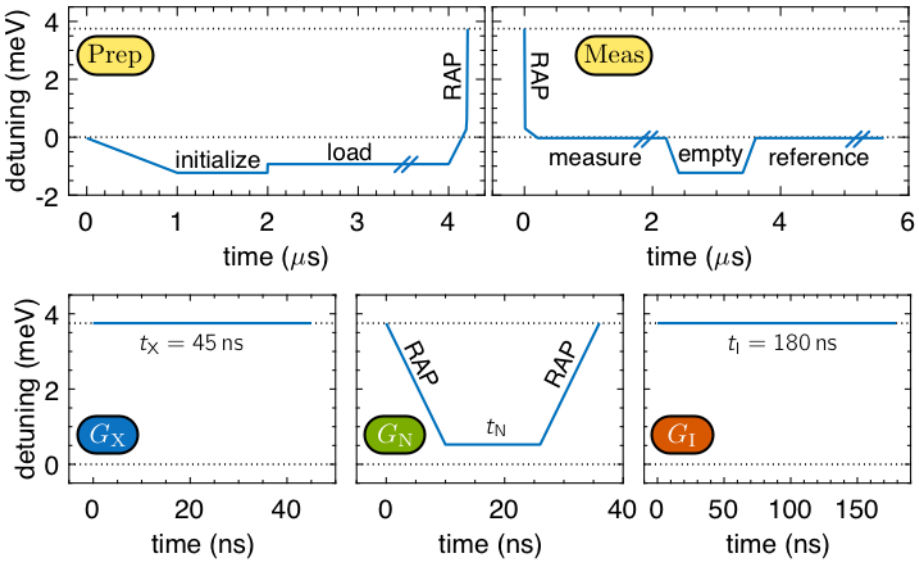

Figure 6.8: Different pulse elements used to construct the gate sequences for the DC-controlled gate set. The *Load*, *Measure*, and *Reference* times have been shortened for clarity. Black dotted lines indicate the $\varepsilon = 0$ meV and $\varepsilon = 3.75$ meV detuning points. t_X (t_I), the control time for the G_X (G_I) gate, is calibrated to perform a $\pi/2$ (2π) rotation around the X axis of the Bloch sphere. The operating point of the G_N gate is varied between GST experiments. t_N, the control time of the G_N gate, is calibrated to perform a $\pi/2$ rotation around the N axis.

qubit operations in isotipically enriched silicon [30], it is more on par with the 92% to 98% fidelities reported for two-qubit gates [69, 172].

6.4 Gate set tomography of the DC-controlled qubit

Fig. 6.8 shows the "buttons" used to construct the sequences needed to perform GST on the DC-controlled qubit (see Sec. 5.7). The *Prep* button initializes the system into the $(1,1)S$ state by loading $(2,0)S$ and ramping across the charge anticrossing to large detuning ($\varepsilon = 3.75$ meV) through rapid adiabatic passage (RAP, see Sec. 5.5). The *Meas* button reads out the qubit along the Z axis of Bloch sphere by ramping through RAP to the Pauli spin blockade region and performing enhanced latching readout (see Sec. 5.4). The G_X gate is performed by idling at the large detuning point for the time, t_X, needed to perform a $\pi/2$ rotation. The G_I gate is similar to the G_X gate, but the idle time, $t_I = 4t_X$, is four times longer in order to perform a 2π rotation. Finally, the G_N gate consists of a rapid ramp to smaller detuning in order

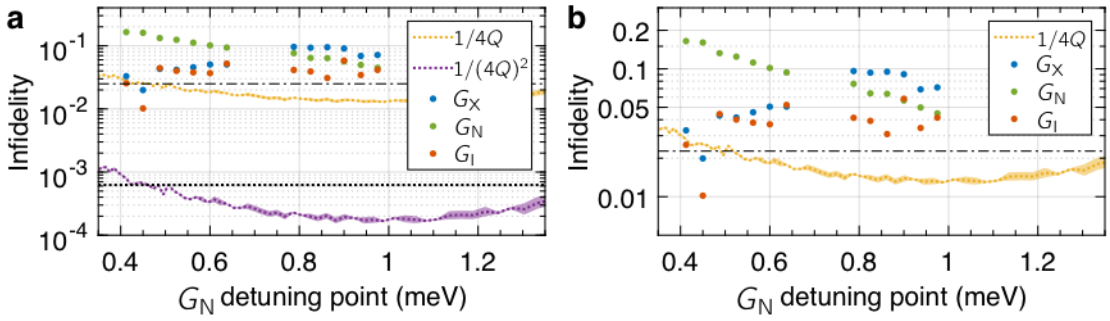

Figure 6.9: (a) Infidelity of the DC-controlled gate set, extracted using GST, as a function of the detuning point at which the G_N gate is performed. The G_X and G_I gates are performed at a detuning of $\varepsilon = 3.75$ meV for all experiments. The applied external magnetic field is 1.2 T for $\varepsilon > 0.7$ meV and 1.1 T for $\varepsilon < 0.7$ meV. The purple and yellow shaded areas correspond to the expected infidelity for the G_N gate, calculated using two different methods (see main text). The black dotted and dash-dotted lines, respectively, indicate the corresponding values expected for the G_X gate. These estimates are obtained using the quality factors reported in Fig. 6.1 for the DC-controlled rotations. **(b)** Vertical zoom in the plot shown in **(a)**.

to turn on the exchange between the two spins, followed by a specified idle time, t_N, before a rapid ramp back to large detuning to turn off the exchange. The detuning at which the G_N gate is performed is varied for each iteration of the experiment, and the t_N time is recalibrated in order to perform a $\pi/2$ rotation around the changing N axis of the Bloch sphere. Because the point at large detuning is the same in all experiments, the infidelity of the G_X and G_I gates are not expected to change. The infidelity of the G_N gate is expected to increase for small detunings, where charge noise causes the quality factor of the qubit rotations to rapidly drop (see Fig. 6.1(f)).

The 154 distinct sequences resulting from the fiducials and germs listed in Tab. 6.2 are constructed using the "buttons" shown in Fig. 6.8. Each of these sequences is measured $N = 10^4$ times, in the manner described in Sec. 6.2. The gate infidelities extracted through GST analysis of these measurements are shown in Fig. 6.9. The GST data taken for $\varepsilon > 0.7$ meV was taken with an external magnetic field of $B_{ext} = 1.2$ T, while data for $\varepsilon < 0.7$ meV was taken on a different day with $B_{ext} = 1.1$ T. The purple shaded region indicates the expected infidelity for the G_N gates, while the black dotted line shows the value expected for G_X. Both these values

are calculated from the quality factors reported in Fig. 6.1(f) and assuming

$$\mathcal{I} \approx 1 - \mathrm{e}^{-(1/Q_N)^2} \approx (1/Q_N)^2, \tag{6.5}$$

where $Q_N = 4Q$ is the number G_X or G_N gates that can be performed within the $1/e$ decay time of the DC-controlled oscillations [143]. This equation differs from Eq. (6.3), which was used for the same purpose in the previous section, because the decay envelope of the DC-controlled rotations is Gaussian-shaped, while the AC-controlled rotations discussed previously exhibit exponential decay. The infidelity estimates calculated for the G_N gates using (6.3) are nonetheless shown in Fig. 6.9 (shaded yellow area) as a means of comparison. The corresponding estimate for the G_X gate is also shown (dash-dotted black line).

The most noticeable detail about the results presented in Fig. 6.9 is that the infidelities extracted from the GST analysis are significantly larger than the values predicted using the quality factor. While the quality factor measurements indicate that extremely good gates are to be expected ($\mathcal{I} < 1 \times 10^{-3}$), the GST analysis seems to indicate that the DC-controlled gates studied are all, in fact, rather poor. $\mathcal{I} \geq 0.03$ is measured for the G_X and G_I gates, while $0.04 \leq \mathcal{I} \leq 0.2$ is measured for the G_N gates. Despite this, the infidelity of the G_N gate does increase at smaller detuning, which is consistent with what was predicted. It is harder to comment on the G_X gate because there is a noticeable difference in the infidelities of this gate between the two sets of experiments. Not only were the experiments performed with slightly different magnetic fields, but they were taken on two different days. It is possible that the qubit parameters may have drifted slightly between the two data sets. However, there does not seem to be any obvious variation in the infidelity of G_X within each data set, which is also in agreement with what was predicted.

In an effort to determine if the GST analysis was at all successful in estimating the DC-controlled gate set, the spin-orbit-driven and exchange-driven rotations are calculated from the GST gate estimates. This is done using the superoperators for the G_X and G_N gates, respectively, in the manner described previously in Sec. 6.3 for the AC-controlled gate set. An example of the superoperators calculated for these gates is shown in Fig. 6.10. The qubit rotations are calculated by applying these superoperators multiple times to the initial state, which is $|S\rangle = +Z$ in the fixed laboratory reference frame. These calculated rotations are shown in Fig. 6.10(b,e).

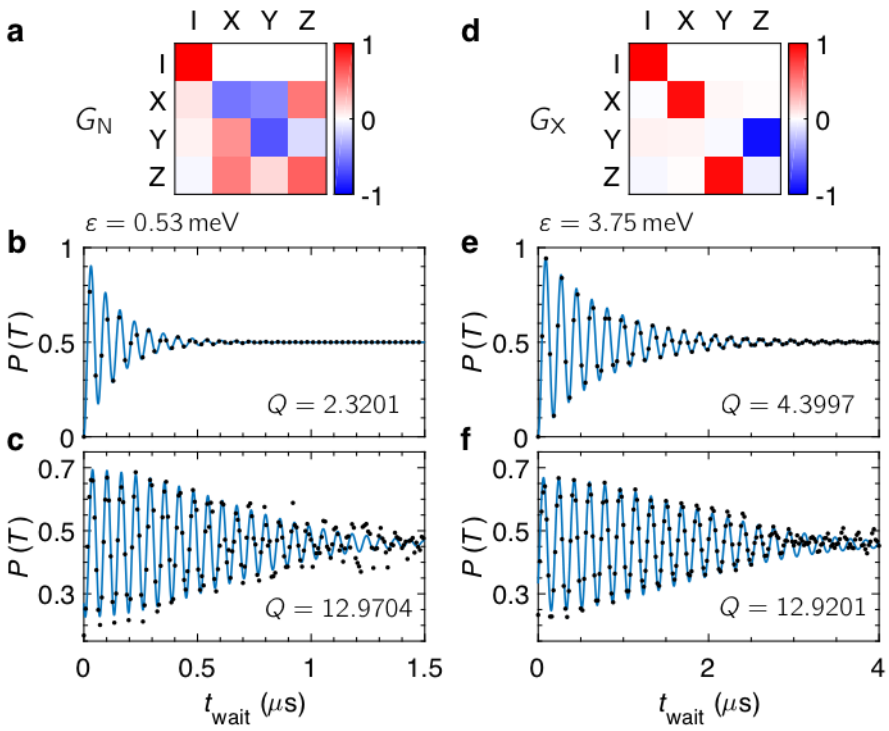

Figure 6.10: (a) Superoperator of the G_N gate provided in the GST report. **(b)** Decay of the exchange-driven G_N oscillations calculated from the superoperator shown in **(a)**. Each black dot corresponds to the application of one additional G_N gate. **(c)** Decay of the G_N oscillations observed experimentally. **(d-f)** Same as **(a-c)**, but for the spin-orbit-driven G_X gate. The G_N gate is performed at $\varepsilon = 0.53$ meV and the G_X is performed at $\varepsilon = 3.75$ meV. The external magnetic field is 1.1 T.

The quality factor is extracted by fitting a sine wave with an exponentially decaying envelope to these points (see Eq. (6.4)). When comparing these calculated decaying oscillations to the ones measured experimentally (shown in Fig. 6.10(c,f)), it is clear that the two do not agree. The difference in the shape of the decay envelope between the calculated and measured oscillations is to be expected. GST assumes a Markovian noise model, which results in the exponential decay of the calculated oscillations, while the presence of non-Markovian noise in the real experiment causes the Gaussian-shaped decay of the measured oscillations. What is unexpected is the marked difference in the decay time of the oscillations. For both the G_X and the G_N gates, the decay time of the calculated rotations is significantly shorter than the one extracted from the experimental data, leading to smaller quality factors than expected. In the case of the G_N gate, there is a factor 5.6 difference between the

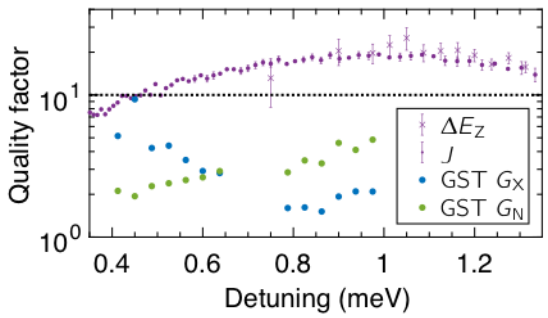

Figure 6.11: Comparison between the measured (purple) and calculated quality factors for the DC-controlled rotations. The calculated values are obtained using the superoperators provided by the GST analysis for the G_X (blue) and G_N (green) gates. The black dotted line is the measured quality factor for the G_X gate.

calculated and measured quality factors. In the case G_X, a factor 2.9 difference is observed.

Fig. 6.11 shows the quality factors calculated in the manner described above for all the GST experiments performed on the DC-controlled gate set and compares them to the quality factors measured at different detunings. It is clear from these results that the Q-factors calculated using the GST gate estimates are consistently much smaller than what is measured experimentally. This observation naturally leads to the suspicion that the GST analysis has failed to properly characterize the DC-controlled qubit and that the infidelities reported in Fig. 6.9 are too large and do not reflect the true performances of the gates. There remain, however, important points to be considered before concluding that the GST experiment has failed.

The first thing to consider is whether or not the measured and calculated quality factors are even supposed to be the same. In Sec. 6.5, the time dependence of the spin-orbit-driven qubit's resonance frequency is measured and discussed. The analysis performed on this data shows the effect that averaging can have on the quality factor and highlights the importance of specifying the amount of averaging as well as the timescales of the experiments when discussing quality factors. The exchange-driven data in Fig. 6.1(a) is an average of 5 scans with a total acquisition time of 20 hours, while the spin-orbit-driven data in Fig. 6.1(b) is an average of 10 scans with a total acquisition time of 60 hours. Because of the small number scans being averaged and the long time delay between these scans, the resulting Q-factors will be mostly affected by noise that occurs over very long time scales. On the other hand, given the method chosen to perform the GST experiment (see Sec. 6.2), the

GST data is essentially an average of 100 scans with a total acquisition time of about 10 minutes. This large number of averages performed over a relatively short period of time means that the Q-factor calculated for the GST experiment will be affected by noise that occurs on much shorter time scales. In fact, the time scales of the GST experiments are much more comparable to the time scales of the repeated spin-orbit-driven oscillations in Fig. 6.12 (see Sec. 6.5) than to the time scales used in Fig. 6.1 to calculate the Q-factors of the DC-controlled rotations. From Fig. 6.12(c), we find that the Q-factor calculated using the GST gate estimates ($Q = 4.3997$ in Fig. 6.10(d)) should be compared to $Q = 25.5$, the value obtained for 100 averaged time traces measured over the course of 10 minutes. This realization only serve to increase the discrepancy between the calculated and measured quality factors for the G_X gate to a factor of 5.8.

The next thing to consider is the effect that the non-Markovian noise will have on the GST analysis. We know that such noise is present in the system because of the Gaussian-shaped decay of the DC-controlled rotations and the observation of slow ($\sim$ 4 kHz/min) drift in the resonance frequency of the spin-orbit-driven rotations (see Fig. 6.12(b) in Sec. 6.5). However, one of the basic assumptions of GST is that the gate operations are Markovian and do not change over time. The presence of non-Markovian noise can lead to model violations and bad fits during the GST analysis. Therefore, the presence of correlated noise in the system may explain to some extent the discrepancy between the expected and measured results. The fact that the AC-controlled oscillations show a decay that is rather more exponential than Gaussian-shaped would also serve to explain why the GST analysis seems to have been more successfull for the AC-controlled gate set. It would be surprising, however, for the presence of correlated noise to have such a big effect as to be solely responsible for the large discrepancy observed between the Q-factors. In order to determine the relative effect of non-Markovian noise on the GST analysis and the Q-factor measurements, one could use software such as QuTiP (Quantum Toolbox in Python) [173] to simulate the results of these experiments in the presence of both correlated and uncorrelated noise of varying strengths.

It is important to note that there is a big difference between the exchange-driven rotations performed during a quality factor measurement and those reproduced using the G_N gate estimate provided by the GST analysis. In the Q-factor measurement, the system is pulsed from large to small detuning, left to evolve for a chosen

time t_{wait}, then pulsed back to large detuning (see Fig. 5.11(b)). For long t_{wait}, the ramps to and from the small detuning point represent a negligible fraction of the total gate operation time. When these rotations are reproduced by applying the G_{N} superoperator several times consecutively to the qubit's initial state, it amounts to repeatedly ramping the system to and from the small detuning point in order to perform multiple $N_{\pi/2}$ rotations (i.e. repeatedly pushing the G_{N} button in Fig. 6.8). It is not unreasonable to assume that the ramp is the "noisy" part of the pulse and that the presence of many ramps would cause the qubit state to be lost more quickly. These fast ramps may, for example, cause leakage towards states outside of the two-dimensional Hilbert space chosen to encode the qubit. It follows that the exchange-driven rotations calculated from the GST gate estimates are expected to decay more quickly than those measured in normal pulsing experiments.

The same explanation cannot be used to explain why the spin-orbit driven rotations performed during a quality factor measurement outlive those reproduced using the G_{X} gate estimates provided by the GST analysis. Because the G_{X} element of the DC-controlled gate set merely consists in idling at large detuning for a specified time t_{X} (see G_{X} pulse element in Fig. 6.8), applying the G_{X} gate repeatedly to a qubit initialized in the $(2,0)S$ state results in the same pulse as the one used for the quality factor measurement (see Fig. 5.10(b)). However, one must bear in mind that, from a GST perspective, a gate must perform equally well at all times for it to be deemed good, regardless of where it is in a pulse sequence. This means that, for the G_{X} gate to be good, it must perform the same operation when it is applied after a G_{Y} gate as when it is applied after another G_{X} gate. In Sec. 5.1.1, it was discussed how the voltage pulses output by the control instruments must be carefully compensated in order to account for the time constant of the bias tee used for wiring the pulsing gates. Other adjustments to the pulses must also be made to correct for any signal delays introduced by the wiring, and to account for the bandwidth of the poly-silicon gates. Given the short timescales of the G_{N} and G_{X} gates, if these adjustments to the pulses aren't perfect, they could result in some pulsing lags or unexpected pulse trajectories at the device level. If this is the case, the ramp at the end of a G_{Y} gate might "bleed" into a subsequent G_{X} gate, altering the operation performed. This would result in an increased infidelity for the G_{X}.

Finally, a last possible explanation for the poor results observed when performing GST on the DC-controlled gates is that gate set tomography, as it is implemented

in this work, merely is not capable of characterizing non-orthogonal gate sets. Theoretically, GST is expected to be able to characterize gate sets where the rotation axes are not separated by 90°, but this has not yet been demonstrated experimentally. To the best of the author's knowledge, the work presented here constitutes the first time that it has been attempted. Thankfully, there exists a simple experiment that can be implemented in order to determine if GST can, in fact, perform equally well for non-orthogonal gate sets as for orthogonal ones. In Sec. 6.3, GST was successfully used to characterize the AC-controlled gate set. An advantage of such resonantly-driven rotations is that it is easy to construct orthogonal gate sets: there must simply be a $\pi/2$ phase difference between the resonant drives of the G_X and G_Y gates (see Sec. 5.8). However, it is equally easy to construct non-orthogonal gate sets by choosing a different angle (e.g. $\pi/4$) as this phase difference. If equally good infidelities are measured for non-orthogonal resonantly-driven gate sets as for their orthogonal counterparts, we will be forced to conclude that GST is, in fact, able to characterize non-orthogonal gate sets and that there is something intrinsic to the DC-controlled gates studied in this work that make them perform unreliably despite their impressively high quality factors.

6.5 Noise in the spin-orbit-driven singlet-triplet qubit

The following section describes the measurement performed to characterize the noise affecting the spin-orbit-driven singlet-triplet qubit. The goal is to measure the change in the resonance frequency of the qubit as a function of time. The qubit is initialized in the $(2,0)S$ state, then transferred to $(1,1)S$ through rapid adiabatic passage (see Sec. 5.5) to a control point C situated at $\varepsilon = 3.75$ meV. At this detuning, the electrons are well separated and there is no exchange interaction between them ($J_{(1,1)} = 0$). The difference in Zeeman energy between the two electrons, ΔE_Z, dominates and the qubit precesses around the X axis of the Bloch sphere, as described in Sec. 5.7.1. After letting the system evolve for a chosen time, t_{wait}, it is ramped back to the Pauli spin blockade region through rapid adiabatic passage and the spin state is measured using enhanced latching readout (see Sec. 5.4). This pulse is equivalent to the one shown in Fig. 5.10(b).

Fig. 6.12(a) shows qubit rotations observed by varying the time spent idling at large detuning. Identical times traces are repeatedly measured over the course of

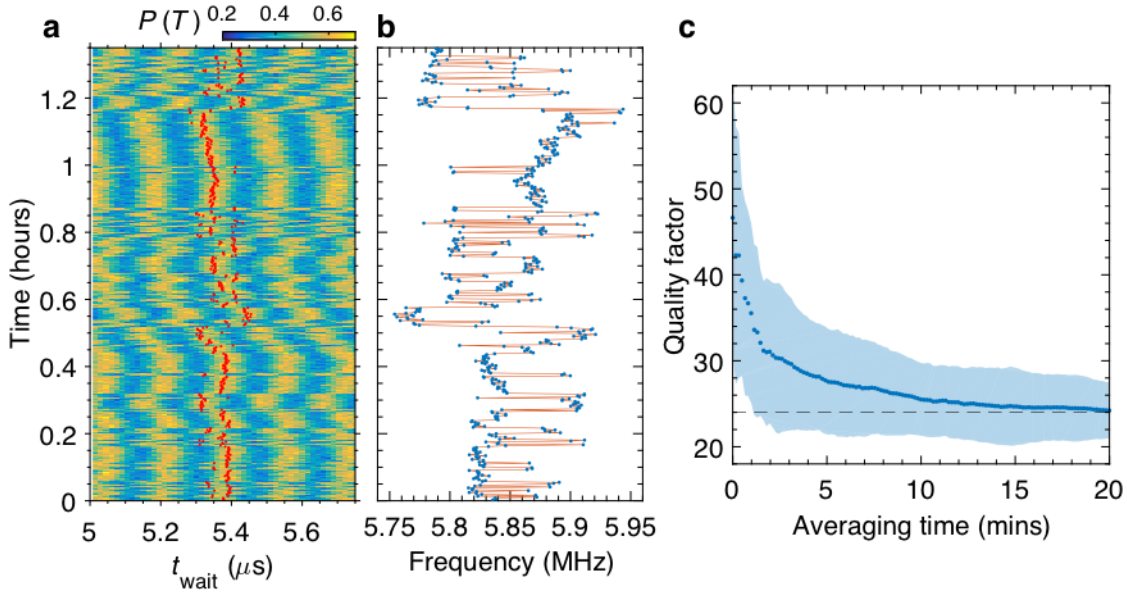

Figure 6.12: (a) Repeated time traces showing the triplet return probability as a function of the duration of the spin-orbit-driven rotations. The rotations are performed at $\varepsilon = 3.75$ meV. The applied external magnetic field is 1.1 T. **(b)** Change in the Larmor frequency of the qubit extracted by performing a fit to the data shown in **(a)**. **(c)** Effect of averaging consecutive time traces on the measured quality factor.

several hours. The time traces (horizontal line cuts of Fig. 6.12(a)) are each taken approximately 10 seconds apart. It is evident, from the shifts and jitter in the measured rotations, that the resonance frequency of the qubit changes over time. A red dot is placed on the 32$^{\text{nd}}$ peak of the measured triplet probability, $P(T)$, in each time trace so as to highlight this jitter. By using Eq. (6.2) to fit a decaying sine wave to each time trace, the time evolution of the qubit's resonance frequency is extracted. The qubit resonance frequency as a function of time is shown in Fig. 6.12(b). From this data, it seems that there is an element of slow random drift, onto which is overlaid a faster "switching" component. The slow drift seems to be on the order of 240 kHz/hour (4 kHz/min), while the fast frequency switching occurs between consecutive time traces and is of varying amplitude, but generally between 40 kHz and 80 kHz. This fast switching noise is likely caused by residual ^{29}Si atoms in the substrate [174]. Flipping of one (or several) of these nearby nuclear spins will modify the local magnetic field felt by one (or both) quantum dots. This will result in a change in the Zeeman energy difference between the dots, ΔE_Z, which will directly affect the resonance frequency of the qubit. Attempting to reproduce this data using

a hidden Markov model might therefore provide useful information regarding the two-level fluctuators, i.e. the ^{29}Si nuclear spins, causing this noise (though this type of analysis is not performed in this work). As for the slow drift, it might be caused, at least in part, by drift in the electrical environment of the qubit. At the control point where the rotations are performed, the resonance frequency varies linearly with detuning (see Fig. 5.12). Therefore, any drift in the electrical environment that results in changes to the detuning at point C will also result in changes in the qubit's resonance frequency.

Fig. 6.12(c) shows the effect that the amount of averaging has on the quality factor measured for an averaged set of data. The data is obtained by averaging together an increasingly large number of consecutive time traces from Fig. 6.12(a) and fitting a decaying sine wave (see Eq. (6.2)) to the averaged time trace in order to extract the quality factor. Repeating this analysis on 44 data sets similar to the one shown in Fig. 6.12(a) results in the mean (blue points) and spread (shaded blue area) of the Q-factor values shown in Fig. 6.12(c). Here, the averaging time is defined as the total time needed to acquire the data that is being averaged. For example, if the first 30 time traces of Fig. 6.12(a) are averaged, the averaging time will be 5 minutes because each time trace takes 10 seconds to acquire. We see that, though the quality factor of a single time trace is $Q = 45$, this value drops rapidly when multiple time traces are averaged. After 5 minutes of averaging, this value has already dropped to $Q = 28$. As the averaging time is increased, the decrease in quality factor slows and seems to saturate at $Q \sim 24$ after about 15-20 minutes. This data highlights the importance of specifying how the data was acquired and what degree of averaging is applied when speaking of the quality factor.

Conclusion

Summary

This thesis studies a spin qubit formed in an isotopically-enriched silicon metal-oxide-semiconductor device. Here, we recall the main results of each chapter.

The thesis begins with Chapter 1, providing brief historical context of the field of quantum information as well as an overview of the advantages and challenges of spin qubits in semiconductors. Singlet-triplet qubits have the advantage of naturally lending themselves to all-electrical control and allow for relaxed spacial constraints when performing two-qubit entangling gates. The choice of spin-orbit coupling as a driving mechanism allows universal single-qubit control to be achieved without the need for external components such as microwave waveguides or micromagnets.

Chapter 2 presents the two different device geometries that are used throughout this work and briefly describes the experimental setup used to perform the measurements. It describes various experimental techniques used to form electrostatically-defined quantum dots and characterize them, including room temperature characterization, charge stability diagrams, Coulomb diamonds, charge sensing, electronic temperature measurements, tunnel rate measurements, excited state spectroscopy, and magnetospectroscopy. After performing the experiments presented in this chapter, the device is ready to attempt coherent spin control experiments.

The following two chapters are focussed on advanced tuning and characterization techniques. Chapter 3 presents experiments on donor-dot devices implanted with Sb and P donors. Donor-based devices are of particular interest because of their potential for very high fidelity rates. A numerical, capacitance-based technique is proposed and used to triangulate the position of an implanted donor with precision. Being able to easily triangulate a donor's position is of particular interest due to the

stochastic nature of the donor implantation technique. Finally, spin-to-charge conversion and energy-selective tunnelling is used to demonstrate single-shot readout of a donor electron.

With respect to advanced tuning techniques, a simple model that can be used to reliably predict dot-lead tunnel rates as a function of applied gate voltage is developed in Chapter 4. The method requires a few simple measurements to be performed in order to extract the tunnel rate lever arms of the device gates. It can then reliably predict tunnel rates for arbitrary combinations of gate voltage. Because the model makes no assumptions about device geometry and gate layout, it can be applied to a wide variety of systems and its range of applications is large. Additionally, the model can be integrated with existing computer-automated tuning procedures, complementing their charge-tuning protocols with ones meant to adjust tunnel rates.

The next chapters focus specifically on the spin-orbit-driven singlet-triplet qubit formed in a double quantum dot. Chapter 5 explains how to calibrate the qubit initialization and readout, identify the slow and rapid adiabatic transfer regimes, and measure the tunnel coupling between the dots. Two different methods for performing arbitrary single-qubit rotations are demonstrated. The "DC-controlled" method performs rotations around two non-orthogonal axes by rapidly pulsing between a regime of large exchange interaction and another dominated by the difference in the Zeeman energy between the dots. The "AC-controlled" method resembles electron spin resonance and is achieved by oscillating the strength of the exchange coupling at the frequency of the qubit. Universal quantum control of the ST qubit can be achieved using either one of these control schemes. By applying AC-controlled rotations with increasing drive amplitude, it is shown that the system can be pushed to the strongly-driven resonant regime where the rotating wave approximation can no longer be used to describe the qubit's evolution. To the best of the author's knowledge, this is the first time that the strong driving regime has been reached using a low-temperature semiconducting spin qubit.

Finally, Chapter 6 presents gate set tomography (GST) as an alternative to process tomography and randomized benchmarking. It is used to investigate the gate fidelity of the spin-orbit-driven singlet-triplet qubit and to determine which of the two proposed control schemes leads to the most reliable gate operations. Though further experiments are needed in order to reach firm conclusions, preliminary re-

sults seem to indicate that the AC-controlled gates have equally high fidelities as the DC-controlled gates despite the fact that the former are much slower and have quality factors 5-7 times smaller than the latter. These results highlight the danger of equating good quality factors to high fidelities, as it is often tempting to do. To the best of the author's knowledge, the results presented in this chapter constitute the first time gate set tomography has been used to assess the performance of qubit rotations around non-orthogonal rotation axes.

Outlook

The fact that the qubit studied can be pushed to the strong driving regime is of particular interest. For most semiconducting qubits, this regime is incredibly difficult to reach. Coplanar waveguides cannot provide sufficiently strong power without heating the device, while micromagnets cannot provide sufficiently large field gradients to compete with the applied external magnetic field. For spin-orbit-driven singlet-triplet qubits, however, this regime is surprisingly easy to reach because the exchange interaction, which serves as the oscillating field, can easily be pulsed to values largely exceeding that of the difference in the Zeeman energy between the dots, which serves as the static field. The large range of driving amplitudes available makes this qubit an ideal system in which to study the transition between the weak and strong driving regimes. This qubit would also be a good candidate for testing various methods that have been proposed for improving qubit control and gate fidelity beyond the rotating wave approximation.

On another topic, one of the many advantages boasted for GST is that it can be used to characterize non-orthogonal sets of gates. Unfortunately, the results presented in this thesis are not sufficient to conclude if it succeeds in performing this task. There is a huge discrepancy between the infidelities reported for the DC-controlled gates and those estimated from the quality factor of the qubit rotations, but the experiments performed do not allow us to determine with any certainty what the cause of this discrepancy might be. It may be due to the fact that GST fails in its promise to provide a proper estimate of these non-orthogonal gates, though this does not seem likely. It seem more probable that the GST results are correct and that there is something regarding the design of the pulse or the implementation of

the experiment that is introducing excessive amounts of error to the gates. A simple experiment involving resonantly driven gates has been suggested and it would finally provide an answer to the question of whether or not GST works equally well for non-orthogonal gates as it does for orthogonal ones. Assuming that this question is answered in the affirmative, GST will become an invaluable tool for objectively characterizing and comparing non-orthogonal control schemes across a wide range of devices.

Bibliography

[1] R. P. Feynman, "Simulating physics with computers," International Journal of Theoretical Physics **21**, 467 (1982).

[2] A. Montanaro, "Quantum algorithms: an overview," npj Quantum Information **2**, 15023 (2016).

[3] P. W. Shor, "Algorithms for quantum computation: discrete logarithms and factoring," in *Proceedings 35th Annual Symposium on Foundations of Computer Science* (1994) pp. 124–134.

[4] P. W. Shor, "Polynomial-time algorithms for prime factorization and discrete logarithms on a quantum computer," SIAM J. on Computing **26**, 1484 (1997).

[5] L. K. Grover, "A fast quantum mechanical algorithm for database search," in *Proceedings of the twenty-eighth annual ACM symposium on Theory of computing*, STOC '96 (ACM, New York, NY, USA, 1996) pp. 212–219.

[6] L. K. Grover, "Quantum mechanics helps in searching for a needle in a haystack," Phys. Rev. Lett. **79**, 325 (1997).

[7] C. H. Bennett and G. Brassard, "Quantum cryptography: Public key distribution and coin tossing," Theoretical Computer Science **560**, 7 (2014).

[8] A. Aspuru-Guzik, A. D. Dutoi, P. J. Love, and M. Head-Gordon, "Simulated quantum computation of molecular energies," Science **309**, 1704 (2005).

[9] B. P. Lanyon, J. D. Whitfield, G. G. Gillett, M. E. Goggin, M. P. Almeida, I. Kassal, J. D. Biamonte, M. Mohseni, B. J. Powell, M. Barbieri, A. Aspuru-Guzik, and A. G. White, "Towards quantum chemistry on a quantum computer," Nature Chemistry **2**, 106 (2010).

[10] D. P. DiVincenzo, "The physical implementation of quantum computation," Fortschritte der Physik **48**, 771 (2000).

[11] A. Barenco, C. H. Bennett, R. Cleve, D. P. DiVincenzo, N. Margolus, P. Shor, T. Sleator, J. A. Smolin, and H. Weinfurter, "Elementary gates for quantum computation," Phys. Rev. A **52**, 3457 (1995).

[12] M. A. Nielsen and I. L. Chuang, *Quantum Computation and Quantum Information* (Cambridge University Press, Cambridge, UK, 2000).

[13] A. R. Calderbank and P. W. Shor, "Good quantum error-correcting codes exist," Phys. Rev. A **54**, 1098 (1996).

[14] A. Steane, "Multiple-particle interference and quantum error correction," Proceedings of the Royal Society of London. Series A: Mathematical, Physical and Engineering Sciences **452**, 2551 (1996).

[15] E. Knill, R. Laflamme, and G. J. Milburn, "A scheme for efficient quantum computation with linear optics," Nature **409**, 46 (2001).

[16] D. Kielpinski, C. Monroe, and D. J. Wineland, "Architecture for a large-scale ion-trap quantum computer," Nature **417**, 709 (2002).

[17] Y. Makhlin, G. Schön, and A. Shnirman, "Quantum-state engineering with Josephson-junction devices," Rev. Mod. Phys. **73**, 357 (2001).

[18] I. Chiorescu, Y. Nakamura, C. J. P. M. Harmans, and J. E. Mooij, "Coherent quantum dynamics of a superconducting flux qubit," Science **299**, 1869 (2003).

[19] T. Hayashi, T. Fujisawa, H. D. Cheong, Y. H. Jeong, and Y. Hirayama, "Coherent manipulation of electronic states in a double quantum dot," Phys. Rev. Lett. **91**, 226804 (2003).

[20] J. R. Petta, A. C. Johnson, J. M. Taylor, E. A. Laird, A. Yacoby, M. D. Lukin, C. M. Marcus, M. P. Hanson, and A. C. Gossard, "Coherent manipulation of coupled electron spins in semiconductor quantum dots," Science **309**, 2180 (2005).

[21] J. T. Muhonen, J. P. Dehollain, A. Laucht, F. E. Hudson, R. Kalra, T. Sekiguchi, K. M. Itoh, D. N. Jamieson, J. C. McCallum, A. S. Dzurak, and A. Morello, "Storing quantum information for 30 seconds in a nanoelectronic device," Nature Nanotechnology **9**, 986 (2014).

[22] M. V. Gurudev Dutt, L. Childress, P. Hemmer, A. Zibrov, F. Jelezko, and M. Lukin, "Spectroscopy and coherent control of single nitrogen-vacancy (NV) centers," in *APS Division of Atomic, Molecular and Optical Physics Meeting Abstracts*, APS Meeting Abstracts, Vol. 37 (2006) p. W1.040.

[23] T. D. Ladd, F. Jelezko, R. Laflamme, Y. Nakamura, C. Monroe, and J. L. O'Brien, "Quantum computers," Nature **464**, 45 (2010).

[24] I. Buluta, S. Ashhab, and F. Nori, "Natural and artificial atoms for quantum computation," Reports on Progress in Physics **74**, 104401 (2011).

[25] R. Hanson, L. P. Kouwenhoven, J. R. Petta, S. Tarucha, and L. M. K. Vandersypen, "Spins in few-electron quantum dots," Rev. Mod. Phys. **79**, 1217 (2007).

[26] J. Clarke and F. K. Wilhelm, "Superconducting quantum bits," Nature **453**, 1031 (2008).

[27] F. A. Zwanenburg, A. S. Dzurak, A. Morello, M. Y. Simmons, L. C. L. Hollenberg, G. Klimeck, S. Rogge, S. N. Coppersmith, and M. A. Eriksson, "Silicon quantum electronics," Rev. Mod. Phys. **85**, 961 (2013).

[28] B. E. Kane, "A silicon-based nuclear spin quantum computer," Nature **393**, 133 (1998).

[29] D. Loss and D. P. DiVincenzo, "Quantum computation with quantum dots," Phys. Rev. A **57**, 120 (1998).

[30] M. Veldhorst, J. C. C. Hwang, C. H. Yang, A. W. Leenstra, B. de Ronde, J. P. Dehollain, J. T. Muhonen, F. E. Hudson, K. M. Itoh, A. Morello, and A. S. Dzurak, "An addressable quantum dot qubit with fault-tolerant control-fidelity," Nature Nanotechnology **9**, 981 (2014).

[31] J. J. Pla, K. Y. Tan, J. P. Dehollain, W. H. Lim, J. J. L. Morton, F. A. Zwanenburg, D. N. Jamieson, A. S. Dzurak, and A. Morello, "High-fidelity readout and control of a nuclear spin qubit in silicon," Nature **496**, 334 (2013).

[32] C. H. Yang, R. C. C. Leon, J. C. C. Hwang, A. Saraiva, T. Tanttu, W. Huang, J. Camirand Lemyre, K. W. Chan, K. Y. Tan, F. E. Hudson, K. M. Itoh, A. Morello, M. Pioro-Ladrière, A. Laucht, and A. S. Dzurak, "Operation of a silicon quantum processor unit cell above one kelvin," Nature **580**, 350 (2020).

[33] X. Rong, J. Geng, F. Shi, Y. Liu, K. Xu, W. Ma, F. Kong, Z. Jiang, Y. Wu, and J. Du, "Experimental fault-tolerant universal quantum gates with solid-state spins under ambient conditions," Nature Communications **6**, 8748 (2015).

[34] T. Frey, P. J. Leek, M. Beck, A. Blais, T. Ihn, K. Ensslin, and A. Wallraff, "Dipole coupling of a double quantum dot to a microwave resonator," Phys. Rev. Lett. **108**, 046807 (2012).

[35] K. D. Petersson, L. W. McFaul, M. D. Schroer, M. Jung, J. M. Taylor, A. A. Houck, and J. R. Petta, "Circuit quantum electrodynamics with a spin qubit," Nature **490**, 380 (2012).

[36] S. G. Carter, T. M. Sweeney, M. Kim, C. S. Kim, D. Solenov, S. E. Economou, T. L. Reinecke, L. Yang, A. S. Bracker, and D. Gammon, "Quantum control of a spin qubit coupled to a photonic crystal cavity," Nature Photonics **7**, 329 (2013).

[37] L. P. Kouwenhoven, T. H. Oosterkamp, M. W. S. Danoesastro, M. Eto, D. G. Austing, T. Honda, and S. Tarucha, "Excitation spectra of circular, few-electron quantum dots," Science **278**, 1788 (1997).

[38] J. M. Elzerman, R. Hanson, L. H. Willems van Beveren, B. Witkamp, L. M. K. Vandersypen, and L. P. Kouwenhoven, "Single-shot read-out of an individual electron spin in a quantum dot," Nature **430**, 431 (2004).

[39] F. H. L. Koppens, C. Buizert, K. J. Tielrooij, I. T. Vink, K. C. Nowack, T. Meunier, L. P. Kouwenhoven, and L. M. K. Vandersypen, "Driven coherent oscillations of a single electron spin in a quantum dot," Nature **442**, 766 (2006).

[40] F. H. L. Koppens, J. A. Folk, J. M. Elzerman, R. Hanson, L. H. W. van Beveren, I. T. Vink, H. P. Tranitz, W. Wegscheider, L. P. Kouwenhoven, and L. M. K. Vandersypen, "Control and detection of singlet-triplet mixing in a random nuclear field," Science **309**, 1346 (2005).

[41] W. M. Witzel, M. S. Carroll, A. Morello, L. Cywiński, and S. Das Sarma, "Electron spin decoherence in isotope-enriched silicon," Phys. Rev. Lett. **105**, 187602 (2010).

[42] L. M. K. Vandersypen, H. Bluhm, J. S. Clarke, A. S. Dzurak, R. Ishihara, A. Morello, D. J. Reilly, L. R. Schreiber, and M. Veldhorst, "Interfacing spin qubits in quantum dots and donors—hot, dense, and coherent," npj Quantum Information **3**, 34 (2017).

[43] E. P. Nordberg, G. A. T. Eyck, H. L. Stalford, R. P. Muller, R. W. Young, K. Eng, L. A. Tracy, K. D. Childs, J. R. Wendt, R. K. Grubbs, J. Stevens, M. P. Lilly, M. A. Eriksson, and M. S. Carroll, "Enhancement-mode double-top-gated metal-oxide-semiconductor nanostructures with tunable lateral geometry," Phys. Rev. B **80**, 115331 (2009).

[44] L. Hutin, B. Bertrand, R. Maurand, M. Urdampilleta, B. Jadot, H. Bohuslavskyi, L. Bourdet, Y. . Niquet, X. Jehl, S. Barraud, C. Bäuerle, T. Meunier, M. Sanquer, S. De Franceschi, and M. Vinet, "SOI CMOS technology for quantum information processing," in *2017 IEEE International Conference on IC Design and Technology (ICICDT)* (2017) pp. 1–4.

[45] J. Levy, "Universal quantum computation with spin-1/2 pairs and Heisenberg exchange," Phys. Rev. Lett. **89**, 147902 (2002).

[46] M. Ciorga, M. Pioro-Ladrière, P. Zawadzki, J. Lapointe, Z. Wasilewski, and A. S. Sachrajda, "Coulomb and spin blockade of two few-electron quantum dots in series in the cotunneling regime," Phys. Rev. B **70**, 235306 (2004).

[47] Z. Shi, C. B. Simmons, J. R. Prance, J. K. Gamble, T. S. Koh, Y.-P. Shim, X. Hu, D. E. Savage, M. G. Lagally, M. A. Eriksson, M. Friesen, and S. N. Coppersmith, "Fast hybrid silicon double-quantum-dot qubit," Phys. Rev. Lett. **108**, 140503 (2012).

[48] D. Kim, Z. Shi, C. B. Simmons, D. R. Ward, J. R. Prance, T. S. Koh, J. K. Gamble, D. E. Savage, M. G. Lagally, M. Friesen, S. N. Coppersmith, and M. A. Eriksson, "Quantum control and process tomography of a semiconductor quantum dot hybrid qubit," Nature **511**, 70 (2014).

[49] E. A. Laird, J. M. Taylor, D. P. DiVincenzo, C. M. Marcus, M. P. Hanson, and A. C. Gossard, "Coherent spin manipulation in an exchange-only qubit," Phys. Rev. B **82**, 075403 (2010).

[50] J. Medford, J. Beil, J. M. Taylor, E. I. Rashba, H. Lu, A. C. Gossard, and C. M. Marcus, "Quantum-dot-based resonant exchange qubit," Phys. Rev. Lett. **111**, 050501 (2013).

[51] L. Gaudreau, A. Kam, G. Granger, S. A. Studenikin, P. Zawadzki, and A. S. Sachrajda, "A tunable few electron triple quantum dot," Applied Physics Letters **95**, 193101 (2009).

[52] M. Russ, J. R. Petta, and G. Burkard, "Quadrupolar exchange-only spin qubit," Phys. Rev. Lett. **121**, 177701 (2018).

[53] M. Rudolph, P. Harvey-Collard, R. Jock, T. Jacobson, J. Wendt, T. Pluym, J. Domínguez, G. Ten-Eyck, R. Manginell, M. P. Lilly, and M. S. Carroll, "Coupling MOS quantum dot and phosphorous donor qubit systems," in *2016 IEEE International Electron Devices Meeting (IEDM)* (2016) pp. 34.1.1–34.1.4.

[54] P. Harvey-Collard, N. T. Jacobson, M. Rudolph, J. Dominguez, G. A. Ten Eyck, J. R. Wendt, T. Pluym, J. K. Gamble, M. P. Lilly, M. Pioro-Ladrière, and M. S. Carroll, "Coherent coupling between a quantum dot and a donor in silicon," Nature Communications **8**, 1029 (2017).

[55] J. R. Petta, H. Lu, and A. C. Gossard, "A coherent beam splitter for electronic spin states," Science **327**, 669 (2010).

[56] J. M. Taylor, J. R. Petta, A. C. Johnson, A. Yacoby, C. M. Marcus, and M. D. Lukin, "Relaxation, dephasing, and quantum control of electron spins in double quantum dots," Phys. Rev. B **76**, 035315 (2007).

[57] B. M. Maune, M. G. Borselli, B. Huang, T. D. Ladd, P. W. Deelman, K. S. Holabird, A. A. Kiselev, I. Alvarado-Rodriguez, R. S. Ross, A. E. Schmitz,

M. Sokolich, C. A. Watson, M. F. Gyure, and A. T. Hunter, "Coherent singlet-triplet oscillations in a silicon-based double quantum dot," Nature **481**, 344 (2012).

[58] X. Wu, D. R. Ward, J. R. Prance, D. Kim, J. K. Gamble, R. T. Mohr, Z. Shi, D. E. Savage, M. G. Lagally, M. Friesen, S. N. Coppersmith, and M. A. Eriksson, "Two-axis control of a singlet–triplet qubit with an integrated micromagnet," Proceedings of the National Academy of Sciences **111**, 11938 (2014).

[59] R. M. Jock, N. T. Jacobson, P. Harvey-Collard, A. M. Mounce, V. Srinivasa, D. R. Ward, J. Anderson, R. Manginell, J. R. Wendt, M. Rudolph, T. Pluym, J. K. Gamble, A. D. Baczewski, W. M. Witzel, and M. S. Carroll, "A silicon metal-oxide-semiconductor electron spin-orbit qubit," Nature Communications **9**, 1768 (2018).

[60] P. Harvey-Collard, N. T. Jacobson, C. Bureau-Oxton, R. M. Jock, V. Srinivasa, A. M. Mounce, D. R. Ward, J. M. Anderson, R. P. Manginell, J. R. Wendt, T. Pluym, M. P. Lilly, D. R. Luhman, M. Pioro-Ladrière, and M. S. Carroll, "Spin-orbit interactions for singlet-triplet qubits in silicon," Phys. Rev. Lett. **122**, 217702 (2019).

[61] G. Feher and E. A. Gere, "Electron spin resonance experiments on donors in silicon. II. Electron spin relaxation effects," Phys. Rev. **114**, 1245 (1959).

[62] P. Harvey-Collard, R. M. Jock, N. T. Jacobson, A. D. Baczewski, A. M. Mounce, M. J. Curry, D. R. Ward, J. M. Anderson, R. P. Manginell, J. R. Wendt, M. Rudolph, T. Pluym, M. P. Lilly, M. Pioro-Ladrière, and M. S. Carroll, "All-electrical universal control of a double quantum dot qubit in silicon MOS," in *2017 IEEE International Electron Devices Meeting (IEDM)* (2017) pp. 36.5.1–36.5.4.

[63] M. D. Shulman, O. E. Dial, S. P. Harvey, H. Bluhm, V. Umansky, and A. Yacoby, "Demonstration of entanglement of electrostatically coupled singlet-triplet qubits," Science **336**, 202 (2012).

[64] A. C. Johnson, J. R. Petta, C. M. Marcus, M. P. Hanson, and A. C. Gossard, "Singlet-triplet spin blockade and charge sensing in a few-electron double quantum dot," Phys. Rev. B **72**, 165308 (2005).

[65] J. K. Gamble, P. Harvey-Collard, N. T. Jacobson, A. D. Baczewski, E. Nielsen, L. Maurer, I. Montaño, M. Rudolph, M. S. Carroll, C. H. Yang, A. Rossi, A. S. Dzurak, and R. P. Muller, "Valley splitting of single-electron Si MOS quantum dots," Applied Physics Letters **109**, 253101 (2016).

[66] T. A. Baart, P. T. Eendebak, C. Reichl, W. Wegscheider, and L. M. K. Vandersypen, "Computer-automated tuning of semiconductor double quantum dots into the single-electron regime," Applied Physics Letters **108**, 213104 (2016).

[67] P. Harvey-Collard, B. D'Anjou, M. Rudolph, N. T. Jacobson, J. Dominguez, G. A. Ten Eyck, J. R. Wendt, T. Pluym, M. P. Lilly, W. A. Coish, M. Pioro-Ladrière, and M. S. Carroll, "High-fidelity single-shot readout for a spin qubit via an enhanced latching mechanism," Phys. Rev. X **8**, 021046 (2018).

[68] J. Yoneda, K. Takeda, T. Otsuka, T. Nakajima, M. R. Delbecq, G. Allison, T. Honda, T. Kodera, S. Oda, Y. Hoshi, N. Usami, K. M. Itoh, and S. Tarucha, "A quantum-dot spin qubit with coherence limited by charge noise and fidelity higher than 99.9%," Nature Nanotechnology **13**, 102 (2018).

[69] W. Huang, C. H. Yang, K. W. Chan, T. Tanttu, B. Hensen, R. C. C. Leon, M. A. Fogarty, J. C. C. Hwang, F. E. Hudson, K. M. Itoh, A. Morello, A. Laucht, and A. S. Dzurak, "Fidelity benchmarks for two-qubit gates in silicon," Nature **569**, 532 (2019).

[70] A. R. Mills, D. M. Zajac, M. J. Gullans, F. J. Schupp, T. M. Hazard, and J. R. Petta, "Shuttling a single charge across a one-dimensional array of silicon quantum dots," Nature Communications **10**, 1063 (2019).

[71] A. M. Tyryshkin, S. Tojo, J. J. L. Morton, H. Riemann, N. V. Abrosimov, P. Becker, H.-J. Pohl, T. Schenkel, M. L. W. Thewalt, K. M. Itoh, and S. A. Lyon, "Electron spin coherence exceeding seconds in high-purity silicon," Nat Mater **11**, 143 (2012).

[72] S. Rochette, M. Rudolph, A.-M. Roy, M. J. Curry, G. A. T. Eyck, R. P. Manginell, J. R. Wendt, T. Pluym, S. M. Carr, D. R. Ward, M. P. Lilly, M. S. Carroll, and M. Pioro-Ladrière, "Quantum dots with split enhancement gate tunnel barrier control," Applied Physics Letters **114**, 083101 (2019).

[73] R. Hanson, L. M. K. Vandersypen, L. H. W. van Beveren, J. M. Elzerman, I. T. Vink, and L. P. Kouwenhoven, "Semiconductor few-electron quantum dot operated as a bipolar spin filter," Phys. Rev. B **70**, 241304 (2004).

[74] K. Ono, D. G. Austing, Y. Tokura, and S. Tarucha, "Current rectification by Pauli exclusion in a weakly coupled double quantum dot system," Science **297**, 1313 (2002).

[75] C. Bureau-Oxton, *Fabrication de nanoaimants pour le contrôle rapide d'un spin électronique dans une boîte quantique double*, Master's thesis, Université de Sherbrooke (2014).

[76] L. P. Kouwenhoven, D. G. Austing, and S. Tarucha, "Few-electron quantum dots," Reports on Progress in Physics **64**, 701 (2001).

[77] K. K. Likharev, "Single-electron devices and their applications," Proceedings of the IEEE **87**, 606 (1999).

[78] D. I. Bradley, R. E. George, D. Gunnarsson, R. P. Haley, H. Heikkinen, Y. A. Pashkin, J. Penttilä, J. R. Prance, M. Prunnila, L. Roschier, and M. Sarsby, "Nanoelectronic primary thermometry below 4 mK," Nature Communications **7**, 10455 (2016).

[79] D. Maradan, L. Casparis, T. M. Liu, D. E. F. Biesinger, C. P. Scheller, D. M. Zumbühl, J. D. Zimmerman, and A. C. Gossard, "GaAs quantum dot thermometry using direct transport and charge sensing," Journal of Low Temperature Physics **175**, 784 (2014).

[80] L. Casparis, M. Meschke, D. Maradan, A. C. Clark, C. P. Scheller, K. K. Schwarzwälder, J. P. Pekola, and D. M. Zumbühl, "Metallic Coulomb blockade thermometry down to 10 mK and below," Review of Scientific Instruments **83**, 083903 (2012).

[81] S. Tarucha, D. G. Austing, T. Honda, R. J. van der Hage, and L. P. Kouwenhoven, "Shell filling and spin effects in a few electron quantum dot," Phys. Rev. Lett. **77**, 3613 (1996).

[82] M. Ciorga, A. S. Sachrajda, P. Hawrylak, C. Gould, P. Zawadzki, S. Jullian, Y. Feng, and Z. Wasilewski, "Addition spectrum of a lateral dot from Coulomb and spin-blockade spectroscopy," Phys. Rev. B **61**, R16315 (2000).

[83] Y. Hada and M. Eto, "Electronic states in silicon quantum dots: Multivalley artificial atoms," Phys. Rev. B **68**, 155322 (2003).

[84] W. H. Lim, C. H. Yang, F. A. Zwanenburg, and A. S. Dzurak, "Spin filling of valley–orbit states in a silicon quantum dot," Nanotechnology **22**, 335704 (2011).

[85] C. King, J. S. Schoenfield, M. J. Calderón, B. Koiller, A. Saraiva, X. Hu, H. Jiang, M. Friesen, and S. N. Coppersmith, "Lifting of spin blockade by charged impurities in Si-MOS double quantum dot devices," Phys. Rev. B **101**, 155411 (2020).

[86] J. Weis, R. J. Haug, K. v. Klitzing, and K. Ploog, "Competing channels in single-electron tunneling through a quantum dot," Phys. Rev. Lett. **71**, 4019 (1993).

[87] D. S. Duncan, D. Goldhaber-Gordon, R. M. Westervelt, K. D. Maranowski, and A. C. Gossard, "Coulomb-blockade spectroscopy on a small quantum dot in a parallel magnetic field," Applied Physics Letters **77**, 2183 (2000).

[88] R. M. Potok, J. A. Folk, C. M. Marcus, V. Umansky, M. Hanson, and A. C. Gossard, "Spin and polarized current from Coulomb blockaded quantum dots," Phys. Rev. Lett. **91**, 016802 (2003).

[89] J. M. Elzerman, R. Hanson, L. H. Willems van Beveren, L. M. K. Vandersypen, and L. P. Kouwenhoven, "Excited-state spectroscopy on a nearly closed quantum dot via charge detection," Applied Physics Letters **84**, 4617 (2004).

[90] T. Fujisawa, D. G. Austing, Y. Tokura, Y. Hirayama, and S. Tarucha, "Nonequilibrium transport through a vertical quantum dot in the absence of spin-flip energy relaxation," Phys. Rev. Lett. **88**, 236802 (2002).

[91] P. Harvey-Collard, *Qubits de spin composés de boîtes quanties et de donneurs dans le silicium*, Ph.D. thesis, Université de Sherbrooke, Sherbrooke, QC, Canada (2018).

[92] J. J. Pla, K. Y. Tan, J. P. Dehollain, W. H. Lim, J. J. L. Morton, D. N. Jamieson, A. S. Dzurak, and A. Morello, "A single-atom electron spin qubit in silicon," Nature **489**, 541 (2012).

[93] Y. He, S. K. Gorman, D. Keith, L. Kranz, J. G. Keizer, and M. Y. Simmons, "A two-qubit gate between phosphorus donor electrons in silicon," Nature **571**, 371 (2019).

[94] B. Koiller, X. Hu, and S. Das Sarma, "Exchange in silicon-based quantum computer architecture," Phys. Rev. Lett. **88**, 027903 (2001).

[95] C. J. Wellard, L. C. L. Hollenberg, F. Parisoli, L. M. Kettle, H.-S. Goan, J. A. L. McIntosh, and D. N. Jamieson, "Electron exchange coupling for single-donor solid-state spin qubits," Phys. Rev. B **68**, 195209 (2003).

[96] M. Singh, J. L. Pacheco, D. Perry, E. Garratt, G. Ten Eyck, N. C. Bishop, J. R. Wendt, R. P. Manginell, J. Dominguez, T. Pluym, D. R. Luhman, E. Bielejec, M. P. Lilly, and M. S. Carroll, "Electrostatically defined silicon quantum dots with counted antimony donor implants," Applied Physics Letters **108**, 062101 (2016).

[97] M. Simmons, F. Ruess, K. Goh, T. Hallam, S. Schofield, L. Oberbeck, N. Curson, A. Hamilton, M. Butcher, R. Clark, and T. Reusch, "Scanning probe microscopy for silicon device fabrication," Molecular Simulation **31**, 505 (2005).

[98] J. F. Ziegler, M. Ziegler, and J. Biersack, "SRIM – the stopping and range of ions in matter (2010)," Nuclear Instruments and Methods in Physics Research Section B: Beam Interactions with Materials and Atoms **268**, 1818 (2010), 19th International Conference on Ion Beam Analysis.

[99] W. G. van der Wiel, S. De Franceschi, J. M. Elzerman, T. Fujisawa, S. Tarucha, and L. P. Kouwenhoven, "Electron transport through double quantum dots," Rev. Mod. Phys. **75**, 1 (2002).

[100] N. C. Bishop, R. W. Young, G. A. Ten Eyck, J. R. Wend, E. S. Bielejec, K. Eng, L. A. Tracy, M. P. Lilly, M. S. Carroll, C. Borrás Pinilla, and H. L. Stalford, "Triangulating tunneling resonances in a point contact," arXiv e-prints , arXiv:1107.5104 (2011).

[101] F. A. Mohiyaddin, R. Rahman, R. Kalra, G. Klimeck, L. C. L. Hollenberg, J. J. Pla, A. S. Dzurak, and A. Morello, "Noninvasive spatial metrology of single-atom devices," Nano Letters **13**, 1903 (2013).

[102] R. H. Foote, D. R. Ward, J. R. Prance, J. K. Gamble, E. Nielsen, B. Thorgrimsson, D. E. Savage, A. L. Saraiva, M. Friesen, S. N. Coppersmith, and M. A. Eriksson, "Transport through an impurity tunnel coupled to a Si/SiGe quantum dot," Applied Physics Letters **107**, 103112 (2015).

[103] K. Nabors, S. Kim, J. White, and S. Senturia, *FastCap User's Guide*, Research Laboratory of Electronics, Department of Electrical Engineering and Computer Science, Massachusetts Institute of Technology, Cambridge, MA 02139 U.S.A. (1992).

[104] "COMSOL multiphysics," COMSOL AB, Stockholm, Sweden .

[105] X. Gao, E. Nielsen, R. P. Muller, R. W. Young, A. G. Salinger, N. C. Bishop, M. P. Lilly, and M. S. Carroll, "Quantum computer aided design simulation and optimization of semiconductor quantum dots," Journal of Applied Physics **114**, 164302 (2013).

[106] A. Morello, C. C. Escott, H. Huebl, L. H. Willems van Beveren, L. C. L. Hollenberg, D. N. Jamieson, A. S. Dzurak, and R. G. Clark, "Architecture for high-sensitivity single-shot readout and control of the electron spin of individual donors in silicon," Phys. Rev. B **80**, 081307 (2009).

[107] A. Morello, J. J. Pla, F. A. Zwanenburg, K. W. Chan, K. Y. Tan, H. Huebl, M. Mottonen, C. D. Nugroho, C. Yang, J. A. van Donkelaar, A. D. C. Alves, D. N. Jamieson, C. C. Escott, L. C. L. Hollenberg, R. G. Clark, and A. S. Dzurak, "Single-shot readout of an electron spin in silicon," Nature **467**, 687 (2010).

[108] R. Thalineau, S. Hermelin, A. D. Wieck, C. Bäuerle, L. Saminadayar, and T. Meunier, "A few-electron quadruple quantum dot in a closed loop," Applied Physics Letters **101**, 103102 (2012).

[109] T. Takakura, A. Noiri, T. Obata, T. Otsuka, J. Yoneda, K. Yoshida, and S. Tarucha, "Single to quadruple quantum dots with tunable tunnel couplings," Applied Physics Letters **104**, 113109 (2014).

[110] M. R. Delbecq, T. Nakajima, T. Otsuka, S. Amaha, J. D. Watson, M. J. Manfra, and S. Tarucha, "Full control of quadruple quantum dot circuit charge states in the single electron regime," Applied Physics Letters **104**, 183111 (2014).

[111] T. Fujita, T. A. Baart, C. Reichl, W. Wegscheider, and L. M. K. Vandersypen, "Coherent shuttle of electron-spin states," npj Quantum Information **3**, 22 (2017).

[112] P.-A. Mortemousque, E. Chanrion, B. Jadot, H. Flentje, A. Ludwig, A. D. Wieck, M. Urdampilleta, C. Bäuerle, and T. Meunier, "Coherent control of individual electron spins in a two-dimensional quantum dot array," Nature Nanotechnology **16**, 296 (2021).

[113] C. Volk, A. M. J. Zwerver, U. Mukhopadhyay, P. T. Eendebak, C. J. van Diepen, J. P. Dehollain, T. Hensgens, T. Fujita, C. Reichl, W. Wegscheider, and L. M. K. Vandersypen, "Loading a quantum-dot based "Qubyte" register," npj Quantum Information **5**, 29 (2019).

[114] C. J. van Diepen, P. T. Eendebak, B. T. Buijtendorp, U. Mukhopadhyay, T. Fujita, C. Reichl, W. Wegscheider, and L. M. K. Vandersypen, "Automated tuning of inter-dot tunnel coupling in double quantum dots," Applied Physics Letters **113**, 033101 (2018).

[115] A. R. Mills, M. M. Feldman, C. Monical, P. J. Lewis, K. W. Larson, A. M. Mounce, and J. R. Petta, "Computer-automated tuning procedures for semiconductor quantum dot arrays," Applied Physics Letters **115**, 113501 (2019).

[116] J. D. Teske, S. S. Humpohl, R. Otten, P. Bethke, P. Cerfontaine, J. Dedden, A. Ludwig, A. D. Wieck, and H. Bluhm, "A machine learning approach for automated fine-tuning of semiconductor spin qubits," Applied Physics Letters **114**, 133102 (2019).

[117] K. MacLean, S. Amasha, I. P. Radu, D. M. Zumbühl, M. A. Kastner, M. P. Hanson, and A. C. Gossard, "Energy-dependent tunneling in a quantum dot," Phys. Rev. Lett. **98**, 036802 (2007).

[118] T. Botzem, M. D. Shulman, S. Foletti, S. P. Harvey, O. E. Dial, P. Bethke, P. Cerfontaine, R. P. G. McNeil, D. Mahalu, V. Umansky, A. Ludwig, A. Wieck, D. Schuh, D. Bougeard, A. Yacoby, and H. Bluhm, "Tuning methods for semiconductor spin qubits," Phys. Rev. Applied **10**, 054026 (2018).

[119] M. J. Curry, T. D. England, N. C. Bishop, G. Ten-Eyck, J. R. Wendt, T. Pluym, M. P. Lilly, S. M. Carr, and M. S. Carroll, "Cryogenic preamplification of a single-electron-transistor using a silicon-germanium heterojunction-bipolar-transistor," Applied Physics Letters **106**, 203505 (2015).

[120] M. J. Curry, M. Rudolph, T. D. England, A. M. Mounce, R. M. Jock, C. Bureau-Oxton, P. Harvey-Collard, P. A. Sharma, J. M. Anderson, D. M. Campbell, J. R. Wendt, D. R. Ward, S. M. Carr, M. P. Lilly, and M. S. Carroll, "Single-shot readout performance of two heterojunction-bipolar-transistor amplification circuits at millikelvin temperatures," Scientific Reports **9**, 16976 (2019).

[121] C. H. Yang, A. Rossi, N. S. Lai, R. Leon, W. H. Lim, and A. S. Dzurak, "Charge state hysteresis in semiconductor quantum dots," Applied Physics Letters **105**, 183505 (2014).

[122] K. Eng, T. D. Ladd, A. Smith, M. G. Borselli, A. A. Kiselev, B. H. Fong, K. S. Holabird, T. M. Hazard, B. Huang, P. W. Deelman, I. Milosavljevic, A. E. Schmitz, R. S. Ross, M. F. Gyure, and A. T. Hunter, "Isotopically enhanced triple-quantum-dot qubit," Science Advances **1**, e1500214 (2015).

[123] B. D'Anjou and W. A. Coish, "Optimal post-processing for a generic single-shot qubit readout," Phys. Rev. A **89**, 012313 (2014).

[124] L. D. Landau, "A theory of energy transfer II," Physikalische Zeitschrift der Sowjetunion **2**, 46 (1932).

[125] C. Zener and R. H. Fowler, "Non-adiabatic crossing of energy levels," Proceedings of the Royal Society of London. Series A, Containing Papers of a Mathematical and Physical Character **137**, 696 (1932).

[126] J. M. Nichol, S. P. Harvey, M. D. Shulman, A. Pal, V. Umansky, E. I. Rashba, B. I. Halperin, and A. Yacoby, "Quenching of dynamic nuclear polarization by spin–orbit coupling in GaAs quantum dots," Nature Communications **6**, 7682 (2015).

[127] R. Hanson and G. Burkard, "Universal set of quantum gates for double-dot spin qubits with fixed interdot coupling," Phys. Rev. Lett. **98**, 050502 (2007).

[128] L. M. K. Vandersypen and I. L. Chuang, "NMR techniques for quantum control and computation," Rev. Mod. Phys. **76**, 1037 (2005).

[129] Y. Song, J. P. Kestner, X. Wang, and S. Das Sarma, "Fast control of semiconductor qubits beyond the rotating-wave approximation," Phys. Rev. A **94**, 012321 (2016).

[130] Y.-C. Yang, S. N. Coppersmith, and M. Friesen, "Achieving high-fidelity single-qubit gates in a strongly driven silicon-quantum-dot hybrid qubit," Phys. Rev. A **95**, 062321 (2017).

[131] M. Pioro-Ladriere, T. Obata, Y. Tokura, Y. S. Shin, T. Kubo, K. Yoshida, T. Taniyama, and S. Tarucha, "Electrically driven single-electron spin resonance in a slanting Zeeman field," Nat Phys **4**, 776 (2008).

[132] G. D. Fuchs, V. V. Dobrovitski, D. M. Toyli, F. J. Heremans, and D. D. Awschalom, "Gigahertz dynamics of a strongly driven single quantum spin," Science **326**, 1520 (2009).

[133] A. Laucht, S. Simmons, R. Kalra, G. Tosi, J. P. Dehollain, J. T. Muhonen, S. Freer, F. E. Hudson, K. M. Itoh, D. N. Jamieson, J. C. McCallum, A. S. Dzurak, and A. Morello, "Breaking the rotating wave approximation for a strongly driven dressed single-electron spin," Phys. Rev. B **94**, 161302 (2016).

[134] F. Bloch and A. Siegert, "Magnetic resonance for nonrotating fields," Phys. Rev. **57**, 522 (1940).

[135] Z. Lü and H. Zheng, "Effects of counter-rotating interaction on driven tunneling dynamics: Coherent destruction of tunneling and Bloch-Siegert shift," Phys. Rev. A **86**, 023831 (2012).

[136] Z. Lü, Y. Yan, H.-S. Goan, and H. Zheng, "Bias-modulated dynamics of a strongly driven two-level system," Phys. Rev. A **93**, 033803 (2016).

[137] Y.-C. Yang, S. N. Coppersmith, and M. Friesen, "Achieving high-fidelity single-qubit gates in a strongly driven charge qubit with 1/f charge noise," npj Quantum Information **5**, 12 (2019).

[138] E. Knill, "Quantum computing with realistically noisy devices," Nature **434**, 39 (2005).

[139] R. Raussendorf and J. Harrington, "Fault-tolerant quantum computation with high threshold in two dimensions," Phys. Rev. Lett. **98**, 190504 (2007).

[140] O. E. Dial, M. D. Shulman, S. P. Harvey, H. Bluhm, V. Umansky, and A. Yacoby, "Charge noise spectroscopy using coherent exchange oscillations in a singlet-triplet qubit," Phys. Rev. Lett. **110**, 146804 (2013).

[141] F. Martins, F. K. Malinowski, P. D. Nissen, E. Barnes, S. Fallahi, G. C. Gardner, M. J. Manfra, C. M. Marcus, and F. Kuemmeth, "Noise suppression using symmetric exchange gates in spin qubits," Phys. Rev. Lett. **116**, 116801 (2016).

[142] M. D. Reed, B. M. Maune, R. W. Andrews, M. G. Borselli, K. Eng, M. P. Jura, A. A. Kiselev, T. D. Ladd, S. T. Merkel, I. Milosavljevic, E. J. Pritchett, M. T. Rakher, R. S. Ross, A. E. Schmitz, A. Smith, J. A. Wright, M. F. Gyure, and A. T. Hunter, "Reduced sensitivity to charge noise in semiconductor spin qubits via symmetric operation," Phys. Rev. Lett. **116**, 110402 (2016).

[143] J. M. Nichol, L. A. Orona, S. P. Harvey, S. Fallahi, G. C. Gardner, M. J. Manfra, and A. Yacoby, "High-fidelity entangling gate for double-quantum-dot spin qubits," npj Quantum Information **3**, 3 (2017).

[144] K. Takeda, J. Kamioka, T. Otsuka, J. Yoneda, T. Nakajima, M. R. Delbecq, S. Amaha, G. Allison, T. Kodera, S. Oda, and S. Tarucha, "A fault-tolerant addressable spin qubit in a natural silicon quantum dot," Science Advances **2**, e1600694 (2016).

[145] X. Zhang, H.-O. Li, G. Cao, M. Xiao, G.-C. Guo, and G.-P. Guo, "Semiconductor quantum computation," National Science Review **6**, 32 (2018).

[146] A. P. Higginbotham, F. Kuemmeth, M. P. Hanson, A. C. Gossard, and C. M. Marcus, "Coherent operations and screening in multielectron spin qubits," Phys. Rev. Lett. **112**, 026801 (2014).

[147] I. L. Chuang and M. A. Nielsen, "Prescription for experimental determination of the dynamics of a quantum black box," Journal of Modern Optics **44**, 2455 (1997).

[148] J. F. Poyatos, J. I. Cirac, and P. Zoller, "Complete characterization of a quantum process: The two-bit quantum gate," Phys. Rev. Lett. **78**, 390 (1997).

[149] M. A. Nielsen, E. Knill, and R. Laflamme, "Complete quantum teleportation using nuclear magnetic resonance," Nature **396**, 52 (1998).

[150] A. M. Childs, I. L. Chuang, and D. W. Leung, "Realization of quantum process tomography in NMR," Phys. Rev. A **64**, 012314 (2001).

[151] M. Mohseni, A. T. Rezakhani, and D. A. Lidar, "Quantum-process tomography: Resource analysis of different strategies," Phys. Rev. A **77**, 032322 (2008).

[152] E. Knill, D. Leibfried, R. Reichle, J. Britton, R. B. Blakestad, J. D. Jost, C. Langer, R. Ozeri, S. Seidelin, and D. J. Wineland, "Randomized benchmarking of quantum gates," Phys. Rev. A **77**, 012307 (2008).

[153] J. Emerson, M. Silva, O. Moussa, C. Ryan, M. Laforest, J. Baugh, D. G. Cory, and R. Laflamme, "Symmetrized characterization of noisy quantum processes," Science **317**, 1893 (2007).

[154] E. Magesan, J. M. Gambetta, and J. Emerson, "Scalable and robust randomized benchmarking of quantum processes," Phys. Rev. Lett. **106**, 180504 (2011).

[155] E. Magesan, J. M. Gambetta, and J. Emerson, "Characterizing quantum gates via randomized benchmarking," Phys. Rev. A **85**, 042311 (2012).

[156] D. Gottesman, "The Heisenberg Representation of Quantum Computers," arXiv e-prints , quant-ph/9807006 (1998).

[157] J. M. Epstein, A. W. Cross, E. Magesan, and J. M. Gambetta, "Investigating the limits of randomized benchmarking protocols," Phys. Rev. A **89**, 062321 (2014).

[158] E. Magesan, J. M. Gambetta, B. R. Johnson, C. A. Ryan, J. M. Chow, S. T. Merkel, M. P. da Silva, G. A. Keefe, M. B. Rothwell, T. A. Ohki, M. B. Ketchen, and M. Steffen, "Efficient measurement of quantum gate error by interleaved randomized benchmarking," Phys. Rev. Lett. **109**, 080505 (2012).

[159] R. Harper and S. T. Flammia, "Estimating the fidelity of T gates using standard interleaved randomized benchmarking," Quantum Science and Technology **2**, 015008 (2017).

[160] Y. R. Sanders, J. J. Wallman, and B. C. Sanders, "Bounding quantum gate error rate based on reported average fidelity," New Journal of Physics **18**, 012002 (2015).

[161] F. Lowenthal, "Uniform finite generation of the rotation group," Rocky Mountain J. Math. **1**, 575 (1971).

[162] R. W. Andrews, C. Jones, M. D. Reed, A. M. Jones, S. D. Ha, M. P. Jura, J. Kerckhoff, M. Levendorf, S. Meenehan, S. T. Merkel, A. Smith, B. Sun, A. J. Weinstein, M. T. Rakher, T. D. Ladd, and M. G. Borselli, "Quantifying error and leakage in an encoded Si/SiGe triple-dot qubit," Nature Nanotechnology **14**, 747 (2019).

[163] S. T. Merkel, J. M. Gambetta, J. A. Smolin, S. Poletto, A. D. Córcoles, B. R. Johnson, C. A. Ryan, and M. Steffen, "Self-consistent quantum process tomography," Phys. Rev. A **87**, 062119 (2013).

[164] R. Blume-Kohout, J. King Gamble, E. Nielsen, J. Mizrahi, J. D. Sterk, and P. Maunz, "Robust, self-consistent, closed-form tomography of quantum logic gates on a trapped ion qubit," arXiv e-prints , arXiv:1310.4492 (2013).

[165] D. Greenbaum, "Introduction to Quantum Gate Set Tomography," arXiv e-prints , arXiv:1509.02921 (2015).

[166] W. van Dam, F. Magniez, M. Mosca, and M. Santha, "Self-testing of universal and fault-tolerant sets of quantum gates," in *Proceedings of the Thirty-Second Annual ACM Symposium on Theory of Computing*, STOC '00 (Association for Computing Machinery, New York, NY, USA, 2000) pp. 688–696.

[167] R. Blume-Kohout, J. K. Gamble, E. Nielsen, K. Rudinger, J. Mizrahi, K. Fortier, and P. Maunz, "Demonstration of qubit operations below a rigorous fault tolerance threshold with gate set tomography," Nature Communications **8**, 14485 (2017).

[168] D. Kim, D. R. Ward, C. B. Simmons, J. K. Gamble, R. Blume-Kohout, E. Nielsen, D. E. Savage, M. G. Lagally, M. Friesen, S. N. Coppersmith, and M. A. Eriksson, "Microwave-driven coherent operation of a semiconductor quantum dot charge qubit," Nature Nanotechnology **10**, 243 (2015).

[169] J. P. Dehollain, J. T. Muhonen, R. Blume-Kohout, K. M. Rudinger, J. K. Gamble, E. Nielsen, A. Laucht, S. Simmons, R. Kalra, A. S. Dzurak, and A. Morello, "Optimization of a solid-state electron spin qubit using gate set tomography," New Journal of Physics **18**, 103018 (2016).

[170] E. Nielsen, K. Rudinger, J. K. Gamble, and R. Blume-Kohout, "PyGSTi: A python implementation of gate set tomography," Available at http://github.com/pyGSTio (2020).

[171] K. Takeda, J. Yoneda, T. Otsuka, T. Nakajima, M. R. Delbecq, G. Allison, Y. Hoshi, N. Usami, K. M. Itoh, S. Oda, T. Kodera, and S. Tarucha, "Optimized electrical control of a Si/SiGe spin qubit in the presence of an induced frequency shift," npj Quantum Information **4**, 54 (2018).

[172] X. Xue, T. F. Watson, J. Helsen, D. R. Ward, D. E. Savage, M. G. Lagally, S. N. Coppersmith, M. A. Eriksson, S. Wehner, and L. M. K. Vandersypen, "Benchmarking gate fidelities in a Si/SiGe two-qubit device," Phys. Rev. X **9**, 021011 (2019).

[173] J. Johansson, P. Nation, and F. Nori, "Qutip: An open-source python framework for the dynamics of open quantum systems," Computer Physics Communications **183**, 1760 (2012).

[174] B. Hensen, W. Wei Huang, C.-H. Yang, K. Wai Chan, J. Yoneda, T. Tanttu, F. E. Hudson, A. Laucht, K. M. Itoh, T. D. Ladd, A. Morello, and A. S. Dzurak, "A silicon quantum-dot-coupled nuclear spin qubit," Nature Nanotechnology **15**, 13 (2020).